Title

Sintering Assisted Additive Manufacturing (SAAM) of Bioceramic Materials for the Production of Net-Shape Bone Scaffold Prototypes

Author

Carrillo, Maricruz Henkel

Publication Date

2023

UNIVERSITY OF CALIFORNIA SAN DIEGO
SAN DIEGO STATE UNIVERSITY

Sintering Assisted Additive Manufacturing (SAAM) of Bioceramic Materials for the Production of Net-Shape Bone Scaffold Prototypes

A Dissertation submitted in partial satisfaction of the requirements
for the degree Doctor of Philosophy

in

Engineering Sciences (Mechanical and Aerospace Engineering)

by

Maricruz Henkel Carrillo

Committee in charge:

University of California San Diego
    Professor Marc Meyers, Co-chair
    Professor Olivia Graeve
    Professor Jian Luo

San Diego State University
    Professor Eugene Olevsky, Co-chair
    Professor Elisa Torresani

2023

The Dissertation of Maricruz Henkel Carrillo is approved, and it is acceptable in quality and form for publication on microfilm and electronically.

Co-Chair

Co-Chair

University of California San Diego

San Diego State University

2023

DEDICATION

I would like to first and foremost dedicate this dissertation to the powerful women in my life, past, present and future. My grandma, Maria de la Cruz, was the matriarch of the family, raising 7 children as a single mom with a 3rd grade education. My mom, Elsa, the first of four women to graduate from her bachelor's program in Tijuana, Mexico. My older sisters, Patricia, Raquel, all thriving successful women in their respective fields and always searching for ways of helping other Latinas reach their goals. My sister Cristina who has been my best friend since birth, never ceases to amaze me and happened to also complete her doctorate degree at the same time, not sure I could have finished without you. And my chosen sisters, Ivette and Joana, for keeping me sane with you humor and love.

I also dedicate this achievement to my biggest inspiration, my nieces and nephew. Brianna, Karina, Sabrina, Alexa, Amaya, Alexa Sofia, Victoria and Leo, I hope I am able to show you that nothing is out of your reach. You can literally be anyone you want to be. I am excited to see what the future holds as we see the next generation grow.

Lastly, I want to thank the love of my life, Charles. There were times when I wasn't sure I was going to have the strength to finish this doctorate degree, but you were always there waiting with a warm plate of food, a power cuddle or a fresh perspective on a challenge I was facing. Thank you.

TABLE OF CONTENTS

LIST OF FIGURES

LIST OF TABLES

LIST OF ABBREVIATIONS

AM	Additive Manufacturing
I-AM	Indirect Additive Manufacturing
BJ	Binder Jetting
SJ	Solvent Jetting
SJD	Solvent Jetting on Dry
SJG	Solvent Jetting on Granulated
SJC	Solvent Jetting on Coated
SS	Subtractive Sintering
NG	Nano Granulated
MC	Micron Coated
ECM	Extracellular Matrix
HAP	Hydroxyapatite
B-TCP	Beta-Tricalcium Phosphate
IPA	Isoproprуl Alcohol
PEO	Polyethylene Oxide
FDM	Fused Deposition Modeling
DIW	Direct Ink Writing
P-3DP	Powder 3D Printing
EBM	Electron Beam Melting
SLS	Selective Laser Sintering
SLM	Selective Laser Melting
SLA	Stereolithography

CAD	Computer Aided Design
CT-Scan	Computer Tomography Scan
MRI	Magnetic Resonance Imaging
SPS	Spark Plasma Sintering
HP	Hot Pressing
CIP	Cold Isostatic Pressing
SEM	Scanning Electron Microscopy
TGA	Thermogravimetric Analysis
DSC	Differential Scanning Calorimetry
FEM	Finite Element Model
XRD	X-Ray Diffraction
CMM	Coordinate Measurement Machine
PSD	Pore Size Distribution
AM-SS	Additive Manufacturing via Subtractive Sintering
MEMS	Micro-Electrical Mechanical Systems
BMC	Business Model Canvas
NSF	National Science Foundation

ACKNOWLEDGEMENTS

I want to thank my professor and advisor Dr. Eugene Olevsky for believing in me and supporting me in the successful completion of this program. You have built an amazing legacy and I am honored to become part of it with this dissertation.

Chapter 5, in part, was published as it may appear in Additive manufacturing, 2020, Lee, Geuntak; Carrillo, Maricruz; Olevsky, Eugene., Elsevier, 2020. The dissertation author was the primary researcher and co-author of this paper.

Chapter 6, in part, was published as it may appear in Rapid Prototyping, 2021, Carrillo, Maricruz; Lee, Geuntak; Olevsky, Eugene., Emerald Publishing Limited, 2021. The dissertation author was the primary researcher and author of this paper.

Chapter 7, in part, was published as it may appear in Journal of European Ceramic Society, 2022, Torresani, Elisa; Carrillo, Maricruz; Haines, Chris; Martin, Darold; Olevsky, Eugene., Elsevier, 2022. The dissertation author was the primary researcher and co-author of this paper.

VITA

2015 Bachelor of Science in Mechanical Engineering, San Diego State University

2018 Master of Science in Bioengineering, San Diego State University

2022 Doctor of Philosophy in Engineering Sciences, Joint Degree with University of California San Diego and San Diego State University

PUBLICATIONS

Articles in Refereed Journals

Carrillo, M., Torresani, E., Olevsky, E. Modeling of Complex Shaped Components Fabricated Using Additive Manufacturing Via Subtractive Sintering Approach. International Journal of Ceramic Engineering and Science. In Review.

Torresani, E., Carrillo, M., Olevsky, E. Fabrication of Powder Components with Internal Channels By Spark Plasma Sintering And Additive Manufacturing. Journal of European Ceramic Society. 2023.

Carrillo, M., Lee, Geuntak., Manière, C., Olevsky, E. Additive manufacturing of powder components based on subtractive sintering approach. Rapid Prototyping Journal. 2021; Ahead-of-print.

Lee, Geuntak., Carrillo, M. Olevsky, E. Fabrication of ceramic bone scaffolds by solvent jetting 3D printing and sintering: towards load-bearing applications. Additive Manufacturing Journal. 2020; 33: 101-107.

United States Provisional Patent

63/389,892: Fabrication of powder components with internal channels by spark plasma sintering and additive manufacturing. Submitted on July 17th, 2022.

NSF Innovation Corps Grant

5A131A: Investigation of Commercialization Strategies for Load Bearing Ceramic Scaffolds Produced via Solvent Jetting. Completed August 31st, 2022.

ABSTRACT OF THE DISSERTATION

Sintering Assisted Additive Manufacturing (SAAM) of Bioceramic Materials for the Production of Complex-Shape Bone Scaffold Prototypes

by

Maricruz Henkel Carrillo

Doctor of Philosophy in Engineering Sciences (Mechanical and Aerospace Engineering)

University of California San Diego, 2023

San Diego State University, 2023

Professor Eugene Olevsky, Co-Chair
Professor Marc Meyers, Co-Chair

Ceramics are known for their wear resistance, hardness, strength, and biocompatibility yet the industrial application of these materials in the orthopedic industry is limited due to the difficulty and cost of manufacturing. Additive Manufacturing (AM) via ink-based powder bed

3D printing provides an exciting opportunity to address these issues in the production of implantable orthopedic components. However, the successful production of mechanically and geometrically compatible bioceramic parts has not been achieved using this coveted technology because the use of advanced sintering technologies together with AM has not been sufficiently investigated. In this work, a multi-faceted comprehensive study was performed which includes experimental testing, detailed characterization, analytical modeling, and finite element simulation of net shape bioceramic manufacturing using Sintering Assisted Additive Manufacturing (SAAM). By integrating the solvent jetting 3D printing method with advanced sintering technologies, high density bioceramic components with tailored geometrical, physical and mechanical properties were produced and provide a novel approach to current bone repair solutions.

1 INTRODUCTION

1.1 Background on bone repair grafts and scaffolds

Grafts used for the repair of bones can be subdivided into four categories: autografts, allografts, xenografts and synthetic grafts. Each type of bone graft has its own advantages and disadvantages, and the choice of graft depends on several factors, including the size and location of the bone defect, the patient's age and overall health, and the surgeon's preference and experience. It is important to understand each of these options for their advantages and disadvantages to better provide a solution that addresses the most important aspects of current bone repair approaches.

Autografts are bone grafts that are harvested from the patient's own body, usually from the iliac crest (the top of the hip bone) [1]. Autografts are considered the gold standard for bone grafting because they have the best chance of integrating well with the patient's existing bone tissue, and they also avoid the risk of disease transmission associated with allografts. However, harvesting an autograft can be painful and may lead to additional complications at the donor site. One of the earliest examples of using bone grafts to support tissue growth dates back to the 16th century, when Ambroise Paré, a French surgeon, used a piece of bone to repair a skull defect [2]. He implanted the bone fragment in the defect, where it acted as a scaffold for new bone tissue to grow around.

Allografts are harvested from a donor, typically a deceased person. Allografts are sterilized and stored in tissue banks before use. They are a good option for bone repair because they do not require a second surgical site for harvest, and they can provide a large amount of bone if needed. However, allografts may have a higher risk of infection or rejection, and they may not integrate with the patient's own bone tissue as well as autografts [3]. In the late 19th century, William Hunter, an English surgeon, developed a technique for repairing large bone defects using a bone graft. He would take a piece of bone from a donor site and transplant it to the site of the defect, where it would act as a scaffold for new bone tissue to grow [4].

Xenografts come from a different species, typically a cow or pig. Xenografts are processed to remove all cellular material before use, leaving only the mineralized bone tissue. They are a good option for bone repair because they are readily available and can be easily stored. However, they have a higher risk of rejection and may not integrate as well with the patient's own bone tissue as autografts or allografts [5]. As recent as June 2021, there was a Tuberculosis outbreak linked to a contaminated bone graft in spinal surgery [6]. The first record of a xenograft being used dates to the 1600s where Dr. Jacob van Meekeren performed surgery on a soldier wounded in battle. Resources and knowledge of grafting materials were very limited at the time, therefore, Meekeren decided to use a piece of dog bone as implant material to heal the soldier’s fractured cranium. This surgery gave big insight into how bone can heal itself and regenerate quickly.

Synthetic grafts, as the name suggests, are bone grafts made from synthetic materials, such as calcium phosphate ceramics, metals or polymers. Synthetic grafts can be manufactured to have specific properties, such as porosity or resorbability, and they do not carry the risk of disease transmission associated with allografts. However, they may not integrate as well with the patient's own bone tissue as autografts or allografts, and their long-term durability and biocompatibility are still being studied [7]. In the 20th century, advances in materials science and biotechnology led to the development of synthetic bone scaffolds [8]. Most common material systems used are either metallic or ceramic.

The history of metals being used for bone repair and replacement can be traced back to the early 19th century, when surgeons began using metal plates and screws to stabilize fractures and correct bone deformities [9]. Metallic implants have been used for over 80 years, first introduced for dental applications in the late 1940s [10]. Specifically, Titanium alloys have become the preferred metals for implantation in load bearing areas of the body such as hips, spine and large bones. This is due to a combination of outstanding mechanical properties, biocompatibility, and corrosion resistance. However, issues with these metallic implants are common [11], [12]. Retrieval studies have pointed out that these materials can be subjected to localized or general corrosion [13], [14]. Stress shielding due to a higher stiffness compared to bone compromises the native bone's integrity [15]–[17]. Ultimately, metallic materials were not designed to go in the body. Paraphrasing from the introduction section of J.J. Klawiter's paper on "Application of porous ceramics for the attachment of load bearing internal orthopedic applications", what are being called biomaterials are actually materials that were designed for other applications but are being applied to orthopedic purposes [18].

Calcium phosphate-based ceramics are of great interest to address the above issues based on similarities and ability to tune for structure and chemistry between these ceramics and bone apatite, the mineral of bone tissue [19]. In fact, more than 10,000 articles were found in the literature when the phrases "calcium," "phosphate," and "scaffolds" were combined. HA and calcium phosphate-based ceramics in general have long been the subject of in-depth research [20]–[23].When looking in literature, the main issue with synthetic ceramics is the difficulty in manufacturing complex porous parts with these materials while maintaining the biocompatibility and mechanical properties necessary for bone replacement [24].

Today, bone is the second most transplanted organ in the world [25]. In the United States, 50% of people over the age of 18 are affected by musculoskeletal diseases including accident-related trauma. According to the Center for Disease Control. in 2010 there were 5 million orthopedic surgical procedures performed in the US which included 2 million bone grafts. After the first synthetic ceramic scaffold was approved in 1991, there is now a plethora of materials available to be used as bone grafts and implants. However, despite the abundance of synthetic materials available, autografts (grafts from a different bone in the patient’s body) are still the golden standard for most bone repair procedures followed by allografts [26], [27].

Ideally, the synthetic scaffold will be used as a temporary structure to hold bone cells, growth factors and vascularization. But it all starts at the harvesting of the stem cells from the same patient. Figure 1.1.1 shows the complete process for bone repair. First, the cells should be cultivated in a petri dish, then they can be implanted onto the synthetic scaffold along with any growth factors or stimuli, then it is implanted in the injury site where the native bone can grow if the scaffold provides the perfect environment for bone healing. Synthetic scaffolds are designed to mimic the natural extracellular matrix (ECM) of bone tissue and provide a three-dimensional structure to support cell attachment, proliferation, and differentiation.

The purpose of the scaffold illustrated in Figure 1.1.1 is provide a platform for cell attachment, cell proliferation, growth factor delivery and mechanical support. Overall, synthetic scaffolds are a promising tool for bone tissue engineering, offering a versatile platform for the repair and regeneration of damaged or lost bone tissue [28], [29]. However, despite significant efforts to address the issues with current bone repair solutions, the arduous challenge to develop an effective way to produce an anatomically relevant, bioactive and mechanical appropriate scaffold required for load bearing large bone defects remains.

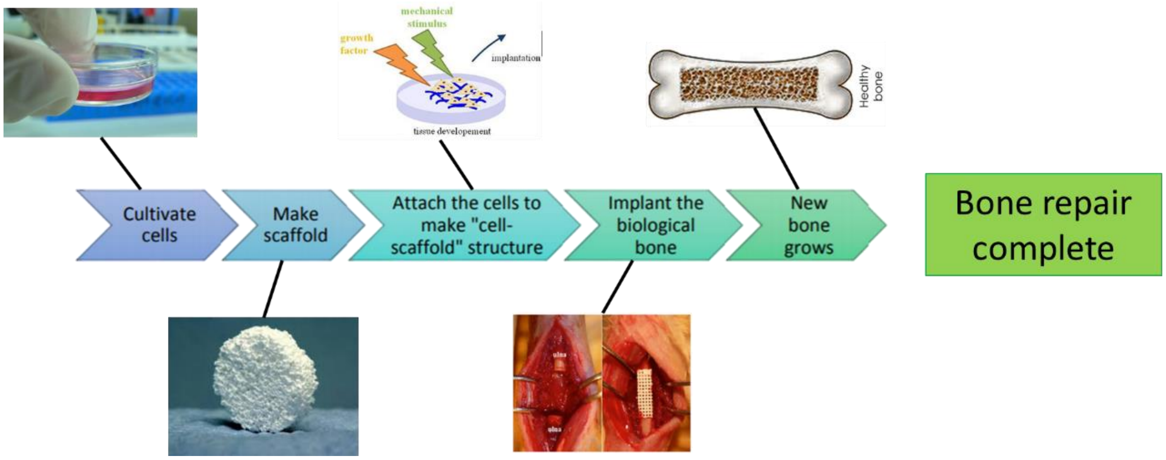

Figure 1.1.1: Overview of a bone repair process using a synthetic scaffold.

1.1.1 Bone graft and scaffold design requirements

The consensus is that replicating all of the native bone’s properties would help decrease host rejections and increase the success of bone repair surgeries [30]–[33]. There are mixed opinions in industry and research communities on what characteristic of bone is most important to mimic in synthetic scaffolds. There are three main properties of a scaffold that should be considered, illustrated in Figure 1.1.1.1: material, surface and architectural characteristics. Current solutions available for clinical use often have some of these characteristics but fail to perform in one or more. For example, metallic solutions perform well in their mechanical properties but do not perform well in tissue integration tests [34]. Contrary to metallic components, synthetic scaffolds made from calcium phosphates such as hydroxyapatite, provide great osseoinduction and integration but lack compressive strength [35], [36]. Since the goal is to replicate bone, it is important to understand how bone works and how it is structured. Bone tissue is made up of distinctive extracellular matrix (ECM), several cell types and water. The ECM is consists of inorganic minerals, mainly plate-like nano-crystalline hydroxyapatite

(HAP), and organic components, mainly triple helix collagen type I. Hydroxyapatite makes up 70 wt% of the inorganic constituents and the majority of the strength of bone originates from this inorganic component [37]. The composition is not the only factor that determines the characteristics of bone, the hierarchical structure with micro and macro porosity also plays an important role. Bone is a mechanosensory organ, it is believed that the cyclic loading of the bone and implant would decrease rejection and healing time. The compressive strength of cortical bone (load bearing component) ranges from 100 to 230 MPa and for trabecular bone (porous component) from 1 to 11MPa [38], [39]. Porous 3D scaffolds fabricated through a variety of methods and including a range of biomaterials have been explored.

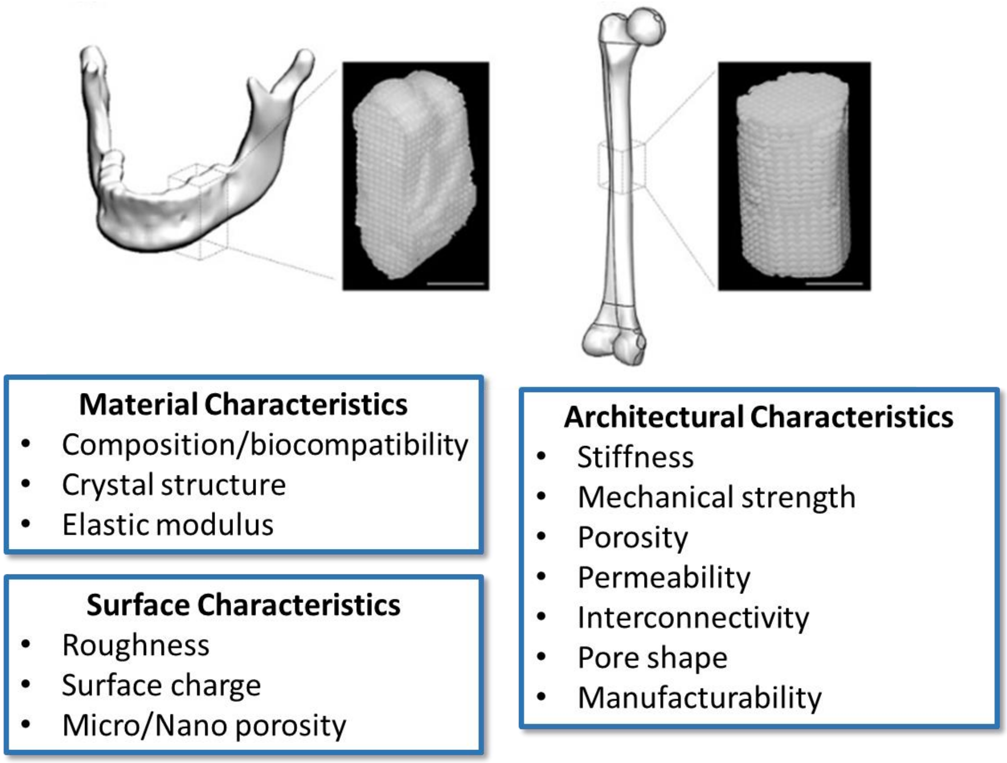

Figure 1.1.1.1: General scaffold requirements divided into 3 property types: material, surface and scaffold characteristics. Scale bar is 1 cm (top images adapted from [40])

Material characteristics such as elastic modulus, stoichiometric composition and crystal microstructure affect the bioactivity of a scaffold and should be considered. The elastic modulus, for example, was discovered to be crucial in fabricating a successful scaffold because it has been shown that mesenchymal stem cells (MSCs) can be directed to specific differentiation paths by changing the elastic modulus of the material [41], [42]. Ions released in trace amounts from various materials were shown to create fluctuations in the pH of the surrounding environment and cells. These fluctuations can deter or promote the activity of osteoprogenitor cells, leading to successful or unsuccessful apposition of new bone to the surface of the synthetic materials [43], [44].

The surface characteristics or roughness of synthetic bone scaffolds is also important. Research done by Deligianni et al. revealed that higher levels of cell adhesion are produced by rougher surfaces. Additionally, there is a strong correlation between surface roughness and osseointegration; roughness can influence protein adsorption, cell adhesion, and osteoblast activity [45]. In recently completed clinical trials, the benefits of implants having a rough surface were noted. Roughened titanium implants in humans were discovered to require a shorter healing time before loading, 6-8 weeks as opposed to 12 weeks [46]. As early as the 1990s, the importance of roughness in bone implants was being evaluated, all studies indicated a surface roughness was not only ideal but necessary [47]. In the medical world, the time in hospital care and reoperations is of upmost importance to reduce. In addition to the surface roughness, nano and micro porosity influences cell attachment and growth. For example, increasing the microporosity of scaffolds with the same surface roughness was shown to increase bioactivity [48], [49].

Architectural characteristics of synthetic scaffolds should be considered when designing a biomimetic scaffold. Pore connectivity and permeability influence nutrient flow and cell migration [50]. Pore shape and size determine bone cell growth and adhesion. Bulk porosity can affect the performance of scaffolds significantly, it is well understood that porosity in the scaffold plays an important role in the bone formation and graft healing process, including [51]–[53]:

- Helps bone cells grow and adhere by providing more surface area.
- Makes cellular migration to the scaffold possible.
- Supports cellular differentiation, proliferation and osseointegration inside scaffold.
- Provides a pathway for new vascularization.

As reference, osteoblasts (bone cells) are typically 10-20 micron in size. In bone grafts and scaffolds, if the pore size is either too small or too large, they restrict the above-mentioned activities. Based on literature, a minimum of 100 micron porosity is required but pore sizes larger than 300 micron is preferred[54]–[56]. Of course, there is an upper limit as well. Very early studies from 1971 indicate 500 micron being the threshold [18]. The architecture of the scaffold in a macro scale can affect the mechanical properties of the overall component. Stiffness, the resistance to macroscopic deformation, will positively or negatively affect the surrounding native bone tissue. If the scaffold is softer than the natural tissue, the scaffold might deform significantly and lead to a failure yet if the scaffold is stiffer than native bone, the skeletal tissue will experience stress shielding [57]. It is important to distinguish between the micro effect of a material’s modulus and a scaffold’s modulus; one affects the cells, and the other affects the overall deformation of the implant.

Lasty, the need for bone replacement for critical size bone defect scenarios is increasing and the clinical need remains unmet [58]–[60]. Currently the critical size that has been determined to need a bone scaffold with specific mechanical properties is 10mm [61]. Given that this is a small length, the demand for scaffolds is extensive. There have also been extensive studies on the preference of growth directions for bone cells in a synthetic scaffold. Where the direction of channels leads to different levels of bone growth making customization an important part of fabricating bone scaffolds [62]. The requirements are understood, ceramics have obvious advantages and now the appropriate manufacturing method needs to be chosen.

1.1.2 Bioceramics used for bone grafts and scaffolds

Ceramic materials have high strength, stiffness and bioactivity offering temporary framework by providing a suitable environment for cell adhesion, growth and overall bone tissue regeneration while being a good candidate for load-bearing applications [63]. There are three basic types of bioceramics: bioinert high-strength ceramics, bioactive ceramics that directly chemically bond with bone or even soft tissue of a living organism, and various bioresorbable ceramics that actively participate in an organism's metabolic process [64]. In recent years, bioceramics have been heavily researched for the area of skeletal repair and reconstruction.

Generally, under the umbrella of ceramics, bone substitutes are calcium based. It's interesting to note that the chemical elements utilized to create bioceramics only make up a small portion of the entire Periodic Table. In particular, alumina, zirconia, carbon, compounds containing silica and calcium phosphates may be used to create bioceramics [24]. These material systems are regarded as bioactive because they adhere to bone and promote the growth of bone tissue.

The resemblance between the surface structure and composition of bioactive materials and the mineral phase of bone has been used to explain the bioactive property.

Inert ceramics are a type of bioceramic that are commonly used in bone implants[65]. Inert means that these materials will not react with surrounding tissues and will therefore not reabsorb back into the body, they will be permanent implants.These ceramics have excellent biocompatibility and are highly resistant to corrosion and wear, making them an ideal material for use in the human body. The two most commonly used inert ceramics for bone implants are alumina (Al_2O_3) and zirconia (ZrO_2). Both of these materials have high strength and toughness, which make them suitable for use in load-bearing applications such as hip and knee replacements. Alumina has been used in orthopedic applications for over three decades and has a long track record of success. It has excellent biocompatibility, is highly resistant to wear, and has a low coefficient of friction, which makes it ideal for use in joint replacements. Alumina is also highly resistant to chemical attack, which ensures its long-term stability in the body. Zirconia is a newer material that has gained popularity in recent years. It has similar mechanical properties to alumina, but its high toughness and fracture resistance make it more suitable for use in dental implants and spinal fusion devices. Both alumina and zirconia can be used in 3D printing of bone implants, which allows for the production of highly customized implants with complex shapes and geometries. 3D printed ceramic bone implants made from these materials can be designed to mimic the mechanical properties of natural bone and can help improve patient outcomes.

Hydroxyapatite (HAP) and its amorphous phase Beta-Tricalcium Phosphate (β-TCP) are the most bioactive ceramics used. Due to its osteoconductivity and osteoinductivity characteristics as well as its superior in vivo degradation, beta-tricalcium phosphate (β-TCP) has emerged as a promising material for some bone regeneration applications [66]. However, hydroxyapatite is preferred due to its direct biocompatibility (does not cause an adverse reaction when implanted in the body) and slightly higher degradation resistance when compared to β-TCP [60]. Stoichiometric HAP ($Ca_{10}(PO_4)_6(OH)_2$) has a structure very similar to that of bone, for this reason, synthetic HAP is FDA-approved and is among the most investigated materials for scaffold composition for over three decades[38]. HAP is also osteoconductive, which means that it provides a surface that allows bone cells to attach and grow, an essential property for bone scaffolds and implants because it helps promote bone growth and integration with the surrounding tissue. Resorbability is a characteristic of implants that should be considered for the next generation of bone repair and replacement solutions. The ability to resorb is important for bone scaffolds, as it allows the scaffold to gradually degrade as new bone tissue is formed, reducing the risk of inflammation and other complications. HAP is slowly resorbable, which means that it can be gradually replaced by new bone tissue as it grows [67]. HAP has good mechanical properties at a micron level which is important for the cells. It can provide sufficient support to the surrounding tissue while also allowing for bone growth and remodeling. This property is essential for bone scaffolds and implants, as they need to be able to support the load of the surrounding tissue while also promoting bone growth. Overall, the combination of biocompatibility, osteoconductivity, resorbability, and mechanical properties make HA an ideal material for bone scaffolds and implants [68]. Its use in these applications has already helped improve patient outcomes and reduce the risk of complications associated with other implant materials.

Despite the successful integration of bioceramics in the orthopedic implant industry, the perfect scaffold material with desirable properties, primarily due to the geometrical limitations, has yet to be encountered and clinical translation of 3D scaffolds has been limited as a result [69]. Modifying or developing novel manufacturing processes offers the opportunity to produce scaffolds with superior biomimetic properties.

1.2 Background on additive manufacturing

Additive manufacturing (AM), also known as 3D printing, is a process of creating three-dimensional objects by building up layers of material [70], [71]. AM technologies can be categorized into types based on the processes and technologies involved, as in ASTM F2792 [72]. Figure 1.2.1 shows different variants of AM technologies [73]. This technique has revolutionized the manufacturing industry by allowing engineers to create complex designs with fewer constraints than traditional manufacturing processes.

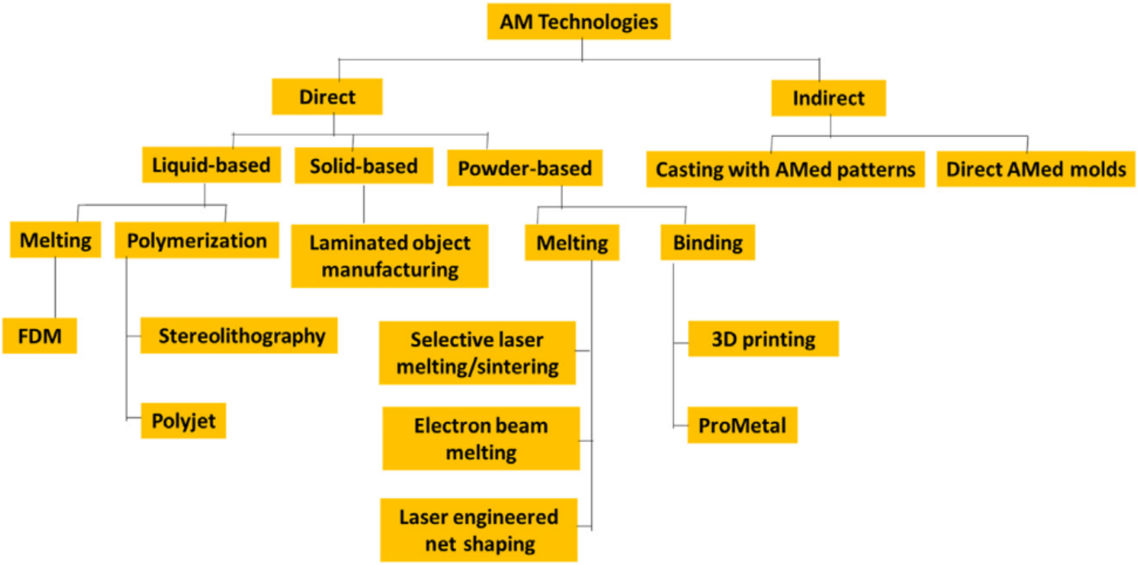

Figure 1.2.1: Categories of additive manufacturing techniques

The history of additive manufacturing dates back to the 1980s when the first process called stereolithography was invented by Charles W. Hull [74]. The process involved using a UV laser to solidify a photopolymer material layer by layer, creating a 3D object. This process was initially used to create prototypes for industrial design and engineering applications. In the following years, other additive manufacturing techniques were developed, including fused deposition modeling (FDM), powder 3D printing (P-3DP), electron beam melting (EBM) and selective laser sintering (SLS). As the technology improved, the applications of additive manufacturing expanded beyond prototyping to include production parts, medical implants, and even food. Today, additive manufacturing is an essential part of modern manufacturing, with a wide range of applications across many industries.

Over the years, additive manufacturing has evolved in several ways, including the range of materials that can be used, the speed of the process, and the size of the objects that can be produced [75]. Initially, additive manufacturing was limited to polymers and plastics. However, as the technology improved, it became possible to print with metals, ceramics, and even biological materials like living cells. Early 3D printers were slow and could only produce small objects. However, advances in technology have made it possible to print larger objects more quickly. Some printers can now produce objects at a rate of several meters per hour. While early 3D printers could only produce small objects, new techniques have made it possible to print larger objects. For example, binder jetting can create sand molds for metal casting, allowing for the creation of very large metal parts. There are several types of additive manufacturing techniques (, each with its own strengths and weaknesses. Here are some of the most common:

- Material Jetting: uses a printhead to deposit tiny droplets of material onto a build platform, creating a part layer by layer.
- VAT Polymerization or Stereolithography (SLA): involves using a UV laser or light to cure a liquid photopolymer resin, creating a solid part layer by layer.

- Binder or Solvent Jetting: involves depositing a liquid binding agent or solvent onto a powder bed to create a solid part.
- Fused Deposition Modeling (FDM) or Material Extrusion: one of the most popular 3D printing techniques, in which a thermoplastic material is melted and extruded through a nozzle to create layers that build up into a 3D object.
- Directed Energy Deposition or Electron Beam Melting (EBM): Powder Bed Fusion: Includes Selective Laser Sintering (SLS) and Selective Laser Melting (SLM)and involves using a laser to fuse powdered material into a solid part.
- Sheet Lamination: this technology stacks and laminates sheets of material to form three-dimensional objects. After the object is constructed, the parts' undesirable areas are gradually removed layer by layer.
- Powder Bed Fusion: Includes Selective Laser Sintering (SLS) and Selective Laser Melting (SLM)and involves using a laser to fuse powdered material into a solid part.

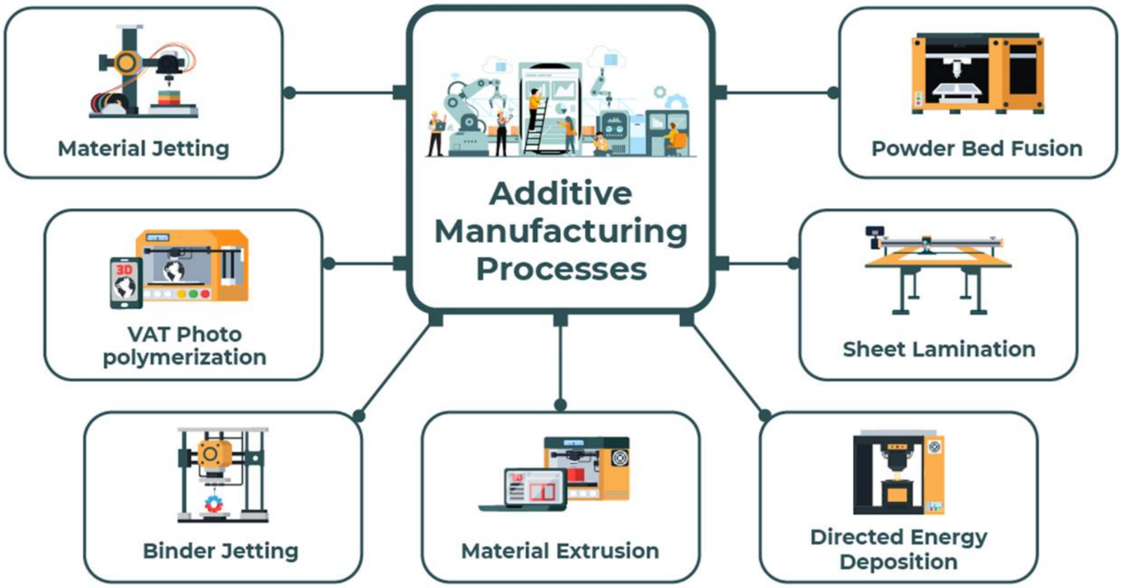

Figure 1.2.2: Common additive manufacturing techniques

It should be noted that Indirect additive manufacturing also exists and has been used to produce higher density components. Indirect additive manufacturing refers to a category of additive manufacturing techniques where a pattern or mold is produced using additive manufacturing, which is then used to create a final product using a traditional manufacturing process such as casting, molding, or forging. Indirect manufacturing techniques are often used for producing complex or intricate parts that are difficult or impossible to produce using traditional manufacturing techniques alone [76]. Investment Casting involves creating a wax pattern using an additive manufacturing technique such as stereolithography or binder jetting, which is then coated in a ceramic material and heated to create a mold. The wax is then melted and drained, and the resulting cavity is filled with molten metal to create the final product [77]. Sand Casting is a process where a pattern is created using an additive manufacturing technique, and then a mold is created using a mixture of sand and a binder material. The mold is then used to cast the final product using molten metal [78]. Powder Injection Molding involves creating a mold using an additive manufacturing technique, which is then filled with a metal or ceramic powder. The powder is then heated and pressurized to create the final product [79]. Recently, Lost Foam Casting has been of great interest. This process involves creating a foam pattern using an additive manufacturing technique, which is then coated in a ceramic material and heated to create a mold. The foam is then vaporized, and the resulting cavity is filled with molten metal to create the final product [80]. Finally, Investment Compression Molding. This process involves creating a pattern using an additive manufacturing technique, which is then used to create a mold using compression molding techniques. The mold is then used to produce the final product using a traditional manufacturing process such as injection molding [81]. These are just a few examples of the many different types of indirect additive manufacturing techniques available today, each with its own unique advantages and applications.

1.2.1 Additive manufacturing of ceramics for bone repair applications

There are many traditional methods of creating porous ceramic prototypes. For bone applications, not only is the level of porosity important but also the pore size and morphology. Manufacturing of simple porous samples were traditionally made either by partial sintering, impregnation of organic materials, foaming or etching [51], [82], [83]. These methods provide repeatable results of highly porous and interconnected channels which allow bone to regrow, rebuild and vascularization in the scaffold. However, given the inverse relationship between porosity and strength, these scaffolds have a low mechanical strength [84], [85]. The mechanical strength of the scaffold, although often not considered, is very important for the success of a bone scaffold. Considerable effort has been made to improve the strength of the porous materials to include novel methods such as freeze casting. Freeze casting provides the directionality of pores seen in real bone and achieved higher mechanical strength values than the traditional methods mentioned above [86], [87]. Despite the improvements, an adequate level of strength has not been achieved while maintaining a desirable level of interconnected porosity.

To address the geometric limitations of traditional manufacturing methods, additive manufacturing (AM) of ceramics is being widely explored for bone repair applications. Scaffold-based bone tissue engineering (BTE) has rapidly increased the amount of research dedicated to the printing of ceramic materials. In fact, the number of peer reviewed publication on 3D printing and its potential application in the biomedical field grew from 8 in 2002 to over 2900 in 2018, largely due to tissue engineering [55], [88], [89]. Bone tissue engineering focused on creating a reliable process to harness stem cells, place them on scaffolds with biological factors that encourage bone formation. For BTE, the scaffold needs to be the right environment to allow and direct the stem cells to form into osteoblasts and osteoclasts (bone cells). As Cameron R.M. Black describes:

> The scaffold provides the extracellular microenvironment for the support and stimulation of stem/cell-driven tissue regeneration serving as a supportive platform for transplanted cells or recruiting and retaining endogenous cells together with appropriate mechanical cues and biological triggers. [90]

Due to the need to understand how best to support the stimulation of this stem cells, many materials have been studied. One set of potential host materials are bioceramics such as hydroxyapatite or calcium phosphates due to their biocompatibility and high level of osseointegration. In addition to the biological properties of the material, the structural and mechanical properties are also important. It has become evident that the fabrication technique, the structure of the scaffolds are very important in dictating the final success of the tissue[91]. Many studies have been conducted on the 3D printing of of these scaffolds due to the ability to tailor the geometry of the scaffolds. Zadpoor et al reviewed how geometrical features such as surface curvature, pore shape and pore size affected the cellular response and tissue regeneration process [92]. From a medical perspective, patient-specific scaffolds are important in bone repair scaffolds and implants because they can be designed to fit the unique anatomical features of an individual's bone defect, which can improve the chances of successful bone regeneration and repair. Unlike traditional off-the-shelf implants, patient-specific scaffolds can be customized to match the size, shape, and contours of the defect, which can improve implant stability, minimize stress shielding, and enhance bone ingrowth [93]–[95]. Overall, patient-specific scaffolds offer a promising approach for personalized bone tissue engineering, which has the potential to improve the effectiveness and safety of bone repair scaffolds and implants.

AM can not only produce customized external geometries, but also internal architecture to obtain truly customizable porous components[96]. The transition to AM is obvious since it provides flexibility and customization is various ways. For example: geometry, internal architecture, porosity, pore morphology and mechanical properties. [97]. A major advantage of AM is the ability to utilize a patient’s anatomical information obtained from the patient through imaging techniques such as computed tomography scan (CT-Scan) or magnetic resonance imaging (MRI) in the design of the Computer Aided Design (CAD) model to be printed. This increases the accuracy in replicating the injury site and accelerates the healing process.

Various methods to 3D print ceramic bone scaffolds specifically were explored to include: selective laser sintering or melting (SLS/SLM), electron beam melting (EBM), fused deposition modeling (FDM), stereolithography (SLA), direct ink writing (DIW), and powder bed inkjet 3D printing (P-3DP) [63], [98]–[100]. These techniques can be divided in two categories: low energy and high energy AM. One advantage of SLS/SLM and EBM, considered high energy AM methods, is that sintering is not required after printing. However, one main risk is present when using high energy printing with bioceramics; the melting temperature of ceramics is relatively high which means the energy output of the laser or beam needs to be excessive, commonly leading to thermal shock [96], [101]. The low energy AM techniques are seen as desirable due to the inherent low cost and energy required for printing. FDM uses a polymer and ceramic composite filament as the feedstock, a heated nozzle to extrude the required shape followed by sintering to remove the polymeric component and for densification of the ceramic component. SLA uses a photo polymeric resin bath mixed with ceramic as the "feedstock", UV light to polymerize the resin followed by sintering for the same purpose as before. For these two techniques, the debinding process is very time consuming and sensitive. If debinded too quickly, the sample will experience cracking. The direct deposition of ceramic slurries using DIW, is one of the most used AM technologies for the fabrication of porous ceramic structures. In this method, viscous ceramic paste comprised of ceramic and a polymeric binder, is extruded through a nozzle. The filament can be composed of submicron ceramic powders and polymeric binder which, facilitates the generation of dense struts upon sintering. However, the shape and resolution of 3D printed parts are limited by the large nozzle size required (~ > 500 μm) and cylindrical filament shape[102], [103].

Conversely, powder-bed inkjet 3D printing (P-3DP) offers several advantages over DIW and other methods for making bone scaffolds to include low cost, high processing speed, smaller resolution (~100 μm), support free process, intrinsic porous structure and rough surface on printed samples [104]. P-3DP was chosen as the main method of printing for this work and will therefore be described in more detail. This technique forms a solid, generated from a computer model, by the deposition of layers of a flowable powder and spraying of ink (water-or polymer-based). A layer of powdered material is first spread and flattened followed by the corresponding layer of ink that is selectively placed; these steps are iteratively replicated until the part is completed. A main advantage of P-3DP for the fabrication of synthetic scaffolds is the intrinsic porosity that results through the control of printing parameters, particle size and particle size distribution. A surface roughness is also intrinsic to the process thus no surface treatment is necessary for bone grafting applications. These two factors can save in processing time and manufacturing cost making the fabrication of bone scaffolds with this cost and time effective P-3DP technology attractive to not only the scientific research community but also the industrial market.

There have been many advancements and research is rampant for 3D printing of ceramics for bone applications as seen in Figure 1.1. The images show three common printing systems: 3DP: a) TCP [105] Copyright2009, Wiley-VCH. b) α-TCP.[106] Copyright 2012, Elsevier. c) β-TCP. [107]Copyright 2008, Wiley-VCH. SLS: d) Ca-P)/poly(hydroxybutyrate-co-hydroxyvalerate) (PHBV). [108] Copyright 2010, The Royal Society. e) HA/PCL. [109] Copyright 2017, Elsevier. f) Carbonated hydroxyapatite (CHAp); [110] Copyright2010, Elsevier. EB: g) pasteβ-TCP. [111] Copyright 2015, The Royal Society of Chemistry. h) β-TCP/HA. [112] Copyright 2014, Wiley-VCH. i) CPC. [113] Copyright 2012, Wiley-VCH. However, there is a clear gap in the printing of load bearing bioceramics particularly due to the low densities of printed components [105]–[111]. The maximum compressive strength of a porous cylindrical scaffold produced via direct and indirect 3D printing in the cited literature is 3 MPa and 30 MPa, respectively, which are not sufficient to mimic the load bearing portion of bone. Furthermore, the maximum porosity of the samples cited are 70% and can be as low as

50 percent [62], [114]–[116]. The lowest compressive strengths belong to powder-based 3D printing.

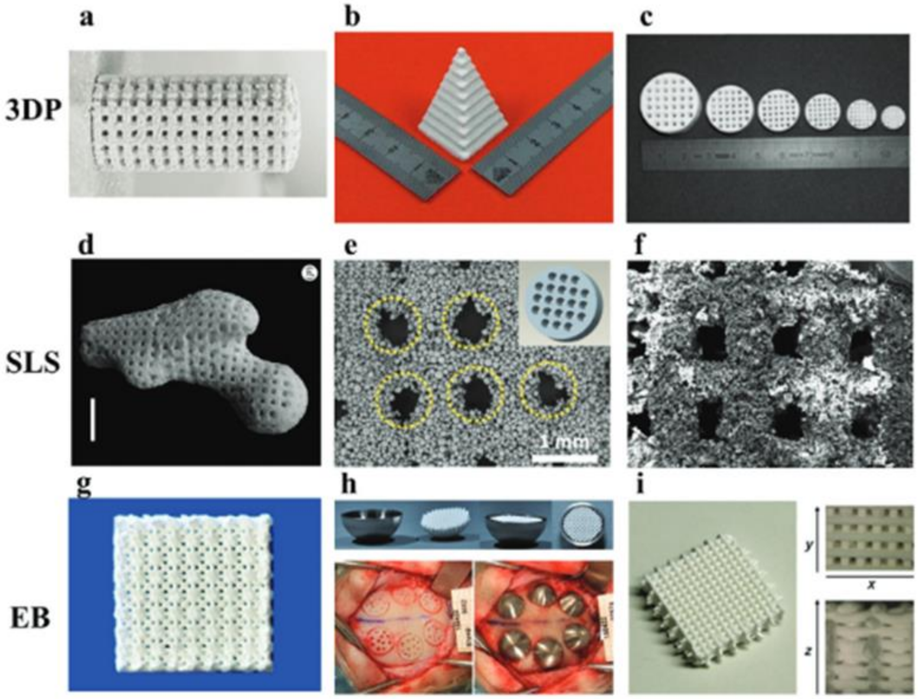

Figure 1.2.1.1: Porous Calcium Phosphate-based scaffolds fabricated by commonly used printing systems (full description in text)

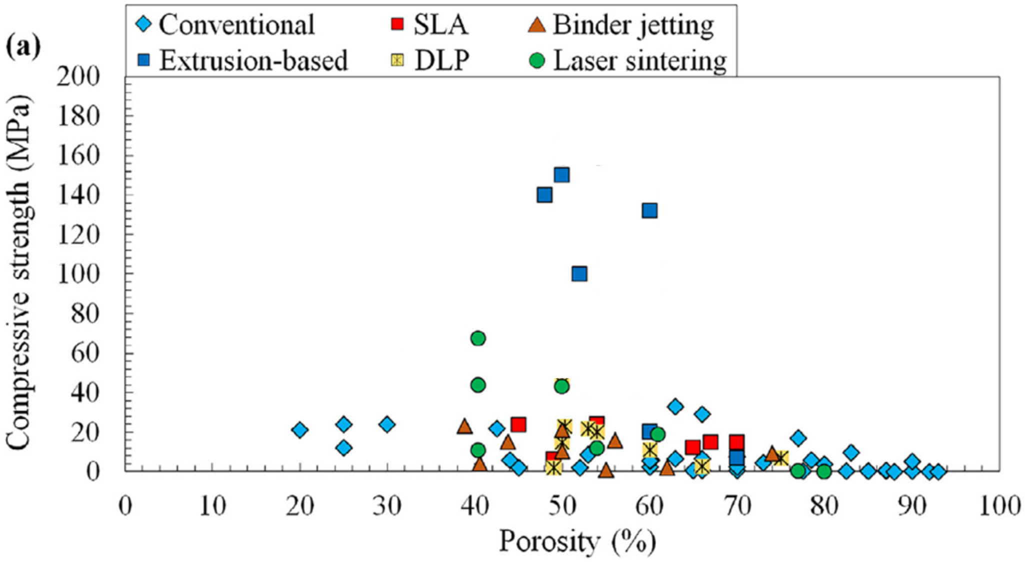

Figure 1.2.1.2: Compressive strength comparison for conventional and 3D printing manufacturing of bioceramics and bioactive glasses. Image was adapted from [117].

This porosity can be used for a wide range of bone replacement applications except for load bearing areas of the body such as the lower limbs or lower lumbar spine. It was observed that the sintering step is often an afterthought in AM studies or simply utilized as a debinding step. There is a gap in the understanding of the sintering behavior of printed samples, specially of bioceramics. Furthermore, the importance of sintering in the resulting physical and mechanical properties of the final scaffold is often ignored.

1.3 Background on sintering

Sintering is a process of compacting and forming a solid mass from a powdered material by heating it below its melting point. The sinterability of powders has been greatly studied in the past 80 years [118]. It has been a key technology in the manufacturing of materials for many centuries. The process involves the application of heat to a powdered material, causing the particles to bond together and form a solid mass. The history of sintering can be traced back to the ancient Egyptians, who used sintering to produce ceramic vessels. The process was also used in China during the Han Dynasty (202 BC - 220 AD) to produce iron tools and weapons. The process was further developed during the Industrial Revolution, when new technologies were developed to make it more efficient and cost-effective. Today, sintering is used in a wide range of applications, from the manufacturing of ceramics and metals to the production of advanced materials for use in electronics, aerospace, and biomedical industries.

Sintering technologies have evolved significantly over the years [119]. In the early days, sintering was carried out in simple furnaces using wood or charcoal as the heating source. As technology improved, new heating sources such as gas and electric were developed, allowing for more precise control of the sintering process. Common sintering techniques include [118], [120]–[122]:

- Conventional sintering: it involves heating a powder material in a furnace at a high temperature for an extended period of time. The process is carried out in air or a protective gas atmosphere, depending on the type of material being sintered. This technique is widely used in the production of ceramics, metals, and composite materials.
- Hot isostatic pressing: a high-pressure sintering technique that involves applying high pressure to a powdered material at high temperature. The pressure is applied using an inert gas such as argon or helium, which is used to compress the material uniformly in all directions. HIP is commonly used in the production of high-performance materials such as superalloys, titanium alloys, and ceramics.

- Microwave sintering: uses microwave heating to sinter the material. The microwave energy absorbed by the material is converted into the kinetic and potential energy that allows heating. Ceramics are most often sintering using microwaves.
- Spark plasma sintering: relatively new sintering technique that uses a combination of pressure and electrical current to sinter a powdered material. The process involves applying a pulsed electrical current to the material, which causes it to heat up rapidly due to the Joule heating effect. The high temperature and pressure generated by the electrical current promote rapid densification of the material, resulting in a highly compacted and uniform product. SPS is used in the production of advanced materials such as nanocrystalline metals, ceramics, and composites.

The discrete character of particulate media was the first foundation for theoretical concepts of sintering. However, in addition to the characteristics of the particles and the nature of their local interactions with one another, macroscopic factors also affect the actual sintering kinetics. One of the main factors impeding the application of sintering theory was the inadequate consideration of macroscopic effects. In 1998, Olevsky's continuum theory of sintering was published to unveil a model that describes the densification of a powder compact under high temperature and pressure [123]. This theory considers the powder compact as a continuum and assumes that the densification process is driven by diffusion and the reduction of surface area of the powder particles. According to the continuum theory, sintering occurs in three stages: particle rearrangement, viscous flow, and grain growth. In the first stage, particles rearrange themselves to achieve a denser packing configuration. In the second stage, particles begin to fuse together due to the formation of necks between adjacent particles. This process occurs by viscous flow of the material at the contact points and leads to a reduction in porosity. Finally, in the third stage, the grains grow by absorbing smaller grains, and the pores between grains disappear. The continuum theory also takes into account the effects of temperature and pressure on the sintering process. Higher temperatures and pressures accelerate the diffusion of atoms and the reduction of surface area, leading to faster densification. The theory also considers the effect of grain boundary diffusion, which can significantly influence the densification rate. This theory has been widely used to predict the densification behavior of various materials, including metals, ceramics, and composites and will be used in this work extensively.

1.3.1 Sintering of ceramics for bone grafting applications

Sintering of ceramics can be traced back 26,000 years. It is a critical process in the production of ceramics, as it involves heating the material to a high temperature to achieve the desired mechanical and physical properties. Improving the sintering process can help produce ceramics with better properties and reduce production costs. It is well understood that powder particle morphology and size can be used to promote densification. Surface and grain boundary diffusion are very sensitive to particle size. More specifically, smaller particle sizes promote sintering because of the larger area available to make contact with surrounding particles. Small particles also lead to smaller pores which result in higher energy per unit volume, more available surface area and higher curvature. All these factors contribute to faster sintering. This phenomena was first noticed by Herring in 1950 and although he only considered one transport mechanism during sintering at the time, the phenomena he termed as scaling law was repeatedly proven by other researchers for years to come [124]. Particle size has an effect not only on the sintering time but also the sintering temperature necessary to sinter.

In the book “Bioceramics and their clinical applications” by Tadashi Kokubo, various ways of producing green bodies for sintering are listed and shown here in Figure 1.3.1.1 [125].

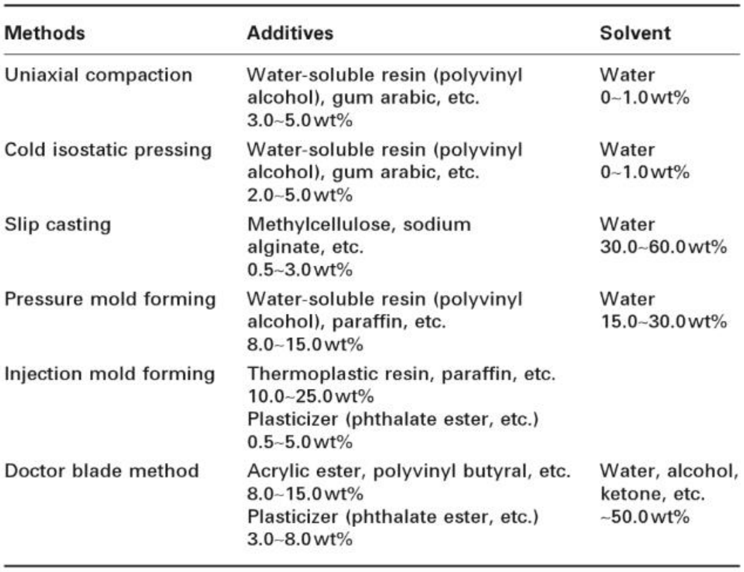

Methods	Additives	Solvent
Uniaxial compaction	Water-soluble resin (polyvinyl alcohol), gum arabic, etc. 3.0~5.0 wt%	Water 0~1.0 wt%
Cold isostatic pressing	Water-soluble resin (polyvinyl alcohol), gum arabic, etc. 2.0~5.0 wt%	Water 0~1.0 wt%
Slip casting	Methylcellulose, sodium alginate, etc. 0.5~3.0 wt%	Water 30.0~60.0 wt%
Pressure mold forming	Water-soluble resin (polyvinyl alcohol), paraffin, etc. 8.0~15.0 wt%	Water 15.0~30.0 wt%
Injection mold forming	Thermoplastic resin, paraffin, etc. 10.0~25.0 wt% Plasticizer (phthalate ester, etc.) 0.5~5.0 wt%	
Doctor blade method	Acrylic ester, polyvinyl butyral, etc. 8.0~15.0 wt% Plasticizer (phthalate ester, etc.) 3.0~8.0 wt%	Water, alcohol, ketone, etc. ~50.0 wt%

Figure 1.3.1.1: Table showing various ways of preparing bioceramic green bodies for sintering.

This book was written in 2008 when 3D printing was still not being heavily researched for biomedical applications. Regardless, green bodies were normally doped with additives in order to enhance sintering. In this way, the process of sintering traditionally made green bodies is similar to that of printed samples containing binder.

As mentioned above, partial sintering is one of the earliest traditional fabrication methods of porous scaffolds [126]. Partial sintering involves the sintering of initially porous powder compacts. Although the pore size and porosity can be controlled by the size of powder particles and degree of sintering, most resulting porosity is closed not interconnected as is desired in bone replacement prototypes. Interconnectivity can be maintained when using vapor transport sintering but requires special equipment, halide atmospheres and vapor[127]. From literature, it can be concluded that although partial sintering has been used to produce highly porous CaP prototypes with varying porosities, the mechanical properties achieved via this technique are not sufficient for load bearing applications[127]–[129].

Additive Manufacturing (AM) is being widely explored to produce custom bioceramic scaffolds and all AM techniques require sintering except for high energy printing such as selective laser melting and electron beam melting. Low energy printing methods require a polymeric binder and therefore, a subsequent debinding step followed by sintering for final consolidation. The sintering step is critical in achieving desirable physical and mechanical properties because during sintering, particle size and shape may change significantly[118]. Additionally, for bioceramics, reactions may also occur which can change the chemical and/or phase composition of the material leading to an alteration in biocompatibility[130], [131].

The sintering of bioceramics has been studied since the early 1970s and the ability to use sintering to produce high density prototypes has been confirmed using free sintering, hot pressing and spark plasma sintering (SPS)[132]–[134]. The behavior of common bioceramics is well understood and some benefits have been found to using one sintering technique over others. For hydroxyapatite $Ca_{10}(PO_4)_6(OH)_2$ for example, it was found that processing HAP via SPS showed an increase in large bone-like HAp crystals on the surface of the samples when compared to samples sintered using a conventional hot-pressing method at the same temperature while limiting the grain growth [135]. Further experimentation is needed to confirm this biocompatibility enhancement in other bioceramics.

Zirconia is an inert biomaterial commonly used for dental applications. The sintering of this material is also well understood. Zirconia has excellent properties such as high strength, high hardness, good wear resistance, acid and alkali resistance, and relatively low temperature required for sintering (~1300 °C) when compared to Alumina for example that has a sintering temperature of 1700 °C [136]. However, the application of pressure prior or during sintering is necessary to reach full densification as is the case with most bioceramics which often limits components to simple shapes.

The fact that pressure is required to fully densify a bioceramic has made the integration of sintering and AM to produce complex shapes difficult. This has resulted in bioceramic scaffolds only meeting the porosity and biocompatibility of a bone replacement but not the sufficient level of strength to be considered for all bone repair applications. More experimentation is necessary to achieve a net shape bioceramic part with complex architecture and tailored properties using powerful sintering techniques.

1.4 Chapter Summary

The benefits of 3D printing and the ability to sinter bioceramics to increase their strength has been proven in literature. However, there is a gap in the ability to produce complex shape, porous bioceramics using both 3D printing and sintering as the main tools to achieve the desired properties. As mentioned by Wang et al in his review on 3d printing of bone tissue scaffolds[89], the most common procedure to produce ceramic bone scaffolds is to “print the ‘green body’, followed by high temperature sintering, which burns out all organic phases, forming pure ceramic scaffold.” This is the extent to which sintering has been considered thus far, as a debinding step. There are several examples of low densities (and thus mechanical strength) of printed scaffolds making them not suitable for load bearing applications. For example, Seidenstuecker et al. printed bioglass and β-TCP samples via extrusion-based 3D printing followed by high temperature sintering and achieved a maximum mechanical strength of 0.64 MPa [137]. Song et al. focused on the pre-sintering portion of the process to increase the density and mechanical strength of the scaffolds. They combined extrusion-based printing and freeze casting followed by free sintering to produce scaffolds with a compressive strength of 24MPa, a superior value than others in literature[138]. In both cases above, sintering was not used as a tool to ameliorate the mechanical properties of the final scaffold. There is a need to better integrate known sintering techniques into the AM process.

The main gap in the additive manufacturing of bone scaffolds has been identified as developing components that encompass both the mechanical performance and multifunctional properties of bone [117]. Bone exhibits great resistance to crack propagation due to its internal design and mechanisms for toughening that operate at various length scales. In order to toughen bone scaffolds, engineers must mimmic the structure and deformation processes of bone. Bioinspired architectures that produce the appropriate toughening mechanisms can be made using advanced manufacturing techniques. Additive manufacturing can also be utilized to modify the composition and biophysical characteristics of the scaffolds, such as microporosity, surface roughness, and elastic modulus.

The successful completion of this work will provide an innovative solution to current issues with orthopedic implants with the potential of enhancing or replacing the current standard of care which relies on autologous bone. Bioceramics are the preferred material system to replace native bone in our bodies, therefore, having an affordable and customizable manufacturing technique to produce net shape bioceramic implants has the potential to revolutionize the current “gold standard”, reduce the costs and move the orthopedics industry closer to truly personalized care.

2 RESEARCH OBJECTIVES AND TASKS

There are many complications with the current synthetic bone implants due to stress shielding and implant debris [139]–[141] but additive manufacturing has the potential to completely revolutionize the orthopedic implant industry. From a scientific perspective, there is a big incentive to investigate AM and Sintering to produce bone scaffolds, simply for the advancement of science and engineering understanding of how various ceramic materials behave when being printed and sintered. However, for me, it is important to also mention the potential this research has as an application in the biomedical industry. The potential to change the current standard of practice that is still causing almost a million people just in the United States alone to have a lower quality of life post-surgery. The potential to make quality bone scaffolds available to more people around the world by making the manufacturing more accessible. The potential to return to utilizing what nature is showing us works already (ceramic materials in bone). The potential to reframe how the scientific community thinks about ceramics, their manufacturability, and their applicability.

2.1 Research Incentives

After an extensive literature review, it can be concluded that additive manufacturing is the future of manufacturing. Powder based printing is of utmost interest to industries due to the reduced waste, ease of use and precision. However, it can also be concluded that the sintering of printed prototypes has not been investigated sufficiently. A full investigation on the integration of sintering as a critical step in the printing of ceramic materials is necessary. The investigation can be simply separated into the two major aspects of additively manufacturing a component: the printing and the consolidation.

(i) The printing portion of the process has been studied in much greater detail than the sintering of bioceramic components. In part, this is due to the studies done on printing parameters for non-ceramic materials. Printing parameters such as layer height, cartridge temperature and roller speed can all be used to optimize the outcome of a print [63], [89], [99], [142], [143]. For example, a smaller layer height and higher cartridge temperature will result in a denser green body. However, sintering a denser green body, does not necessarily lead to a higher final density in printed ceramic samples. The reason behind these phenomena is unknown but can be investigated by analyzing the microstructure of printed samples and optimizing the printing powder for sintering.

(ii) Sintering is a well-established and highly studied discipline. However, sintering of *printed* samples seems to evolve in a different way when compared to traditional green bodies and therefore requires further investigation. The study of the sintering behavior of metallic parts printed via binder jetting is on the rise. Publications show there is anisotropy in sintering as was as in the microstructure of printed samples [144]–[146]. However, the same behavior cannot be assumed for ceramics given that initial tests show that ceramics printed via binder jetting cannot be fully sintered using pressure-less sintering techniques [104].

Overall, it can be observed that a gap in knowledge and understanding exists in the sintering behavior of ceramics and bioceramics which has limited the application of said materials. There is also a general impression within the manufacturing community that ceramics will never achieve the level of use and applicability as metals due to their current limitations. The successful integration of AM and advanced sintering techniques to produce highly technical ceramic parts can change the trajectory of ceramic manufacturing.

2.2 Research Objectives

Based on the literature review and incentives observed, a comprehensive research study was constructed to address current gaps in the production of complex shape. The main objectives directly relate to the two major incentives (i) and (ii) described in detail above. It was demonstrated that the printing and sintering behaviors of bioceramic materials need to be better understood to produce highly complex net shapes which will be addressed in this work. To achieve this, two major research objectives were formulated:

a) Optimization of the green bodies via experimentation. Paying special attention to printing parameters and powder morphology. This objective is aimed at understanding the green body microstructure and how that affects the sinterability of the printed prototype.

b) Optimization of sintering cycles and method. This objective is aimed at integrating advanced sintering techniques, to include field-assisted methods, with AM to achieve near full density complex shaped bioceramic prototypes.

Both objective a) and b) will include an experimental program and will be supported by the continuum theory of sintering-based finite element models to predict the evolution and/or distortions of components during the pressing (if applicable) and sintering processes. This modeling will be used to design initial geometries of printed parts that will result in the final desired geometry after all post-processing steps.

2.3 Research Tasks

Objectives a and b will be achieved by conducting the following five major tasks:

a. For objective a, the powder preparation method of the printing powder will be explored. Plenty of research has been done on the effect of printing parameters on the printed component, therefore, a series of experiments will be conducted to optimize the feed powder instead. For example, by varying the powder shape, size and binder application method.

b. A well-known approach to increasing sinterability is increasing the density of the green body prior to sintering. For this task, indirect additive manufacturing will be explored. The optimal powder for the printing of a sacrificial mold will be determined, following by Cold Isostatic Pressing of the sample to increase the density before free sintering. This task will also support Objective a.

c. Printed green bodies from tasks b and c will then be consolidated. The pressure-less sintering cycle will be optimized experimentally for various bioceramics. This will be the first task to address objective b and will be dedicated only to free sintering.

d. Pressure-assisted sintering will be used to develop a novel way to make complex shaped bioceramics while leveraging the strengths of AM found in tasks a-c. Specifically Spark Plasma Sintering (SPS) will be investigated and will support objective b.

e. Finally, microstructural characterization and mechanical testing of prototypes produced in tasks a-d will be conducted. This will support both objective a and b in evaluating the biomimetic properties of the produced scaffolds.

Research objectives and task conducted during my PhD research program can be seen graphically in the figure below:

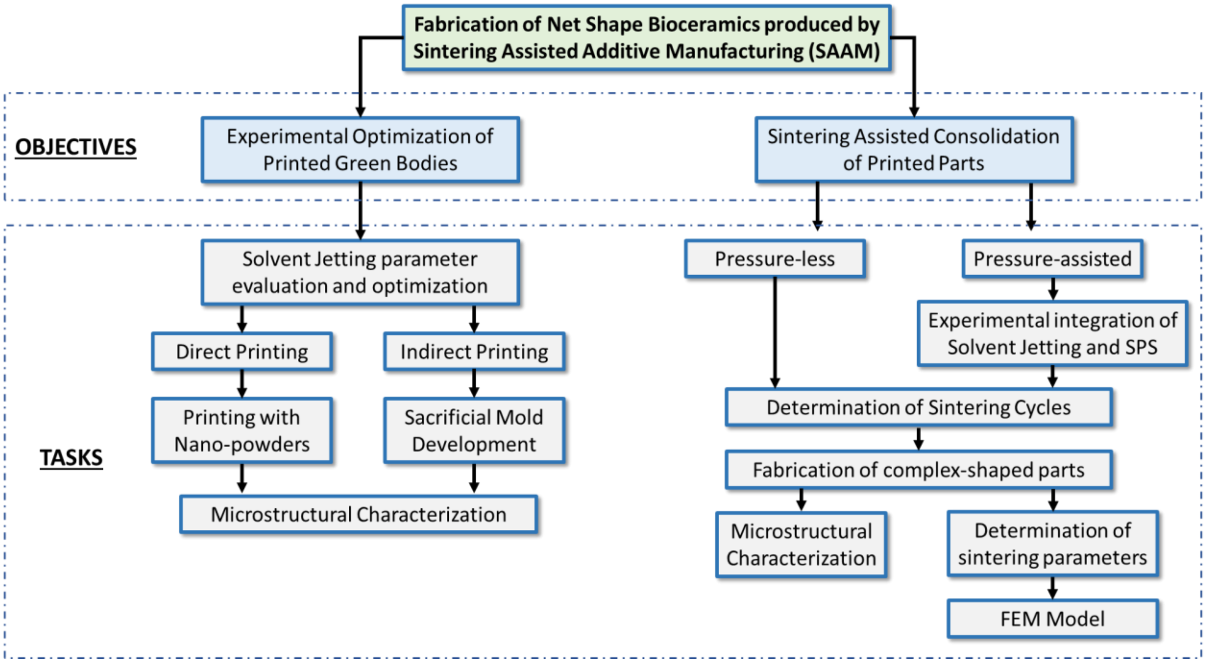

Figure 2.3.1: Flowchart illustrating the research objectives and tasks.

2.4 Selection of 3D Printing Method

There is an important distinction between Binder Jetting (BJ) and Solvent Jetting (SJ). The BJ technique was first invented by Sachs et al. at Massachusetts Institute of Technology (MIT) in 1990 and is described as “the deposition of powdered material in layers and the selective binding of the powder by “ink-jet” printing of a binder material.” [71] On the other hand, SJ is a technique where the binder is contained in the powder feedstock. A water-based solvent is dispensed as the “ink” which activates the binder in the powder bed selectively binding the geometry dictated by the Computer-Aided Design (CAD) file in a layer by layer basis. A diagram of how both powder-based inkjet printer works can be seen in Figure 2.4.1, in BJ the binder is in the ink cartridge, in SJ the binder is mixed in with the powder [147], [148].

In this work, SJ was chosen due to the ease of use, ability to change most parameters of interest and its economic advantage; an SJ printer was custom built in the laboratory from an affordable polymeric printer whereas a BJ printer would cost ten times as much to purchase.

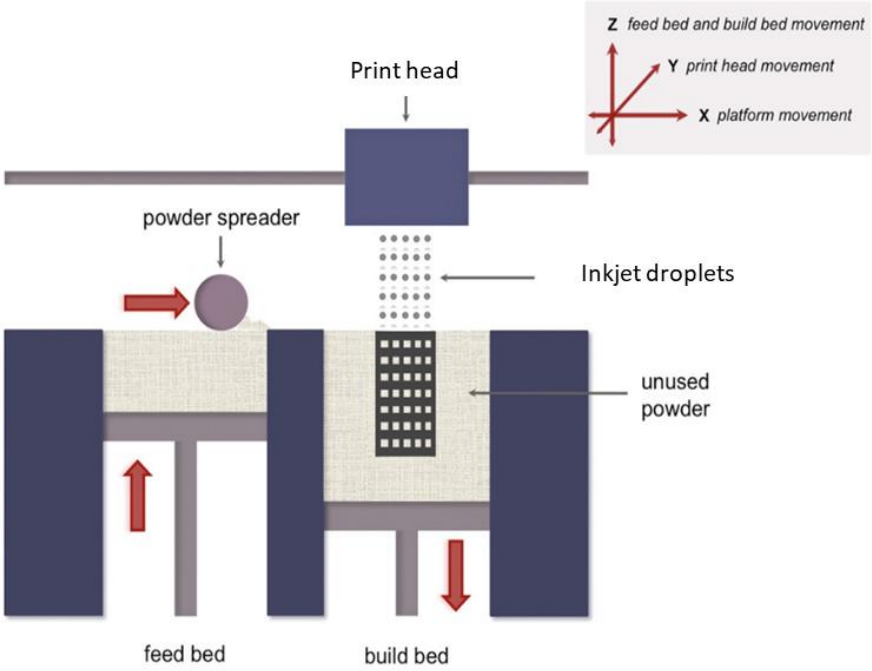

Figure 2.4.1: General powder-based inkjet printing method.

For the entirety of this research work, 3D printing was carried out in a custom-made solvent jetting printer. The water-based ink was composed of 8.3vol% of Isopropyl alcohol (IPA), 8.3 vol% of diethylene-glycol and 83.4 vol% of DI water. The 3D printer adjusted the amount of the printing ink by controlling the cartridge temperature through the use of a resistor in the nozzle of the HP 45 ink cartridge. The higher the nozzle temperature, the more ink was spread on to the powder bed during 3DP. The powders were deposited by the powder dispenser with a vibration motor, then spread and flattened by a roller as shown in Figure 3.1 above. Once the preparation layers were spread, the inkjet cartridge sprayed water-based ink in the designated areas as dictated by the CAD model. This process was repeated layer by layer until the printed object was completed.

2.5 Chapter Summary

Research objectives and background information was provided in this chapter. Possible venues to increasing the green density and sinterability of printed components have been proposed. It should be noted that although increasing the final sintered density of a printed sample would be one solution to improving the mechanical properties of the component, full density is not always a desired feature of most bone scaffolds. Porosity, at different levels, is a desired characteristic for every bone scaffold. To maintain a high level of porosity in the printed scaffold, the major critical factor that can improve the strength of a scaffold is the pore-grain structure. More specifically, the following factors can affect the final strength of the scaffold: pore size, neck size, strut density, grain size and component geometry.

3 PRINTING OPTIMIZATION OF GREEN BODIES FABRICATED VIA SOLVENT JETTING

The Solvent Jetting (SJ) method can be sub-divided into 3 approaches: (1) Solvent Jetting on Dry (SJD), (2) Solvent Jetting on Granulated (SJG), and (3) Solvent Jetting on Coated (SJC) feedstock powder. The SJD method simply mixes the polymeric binder and target powder in a dry condition and makes the freeform by spraying liquid solvent. For example, Shanjani et al. used this method to produce a 35 vol% porous calcium polyphosphate with a compressive strength of 33.86 MPa for tissue engineering purposes via Solid Freeform Fabrication (SFF) [149]. SJG makes the feedstock by drying a slurry which is composed of a polymeric binder and the target powder commonly by freeze drying or spray drying. Chumnanklang et al. demonstrated this technique by using a granulated feedstock consisting of nanosized Hydroxyapatite (HAP) and freeze drying it. Strength of the scaffold was shown to increase with increasing binder concentration [150]. In the SJC method the particle is coated by mixing the powder particles, water and polymeric binder followed by ball milling to remove the agglomerations. For example, Kakisawa et al. showed the fabrication of a porous nickel structure using SJC method. Non-uniformity was observed in the coated powder samples [151]. For this work, the SJG method was chosen. In addition to the binder integration method, the characteristics of the feedstock powder have an impact on the green density of the printed parts.

The most important characteristic for the feedstock during SJ and all powder-based printing is flowability. This traditionally means the powder particle size must be in the range of 25μm-150μm [152]. Larger particle sizes yield more flowable powders and smaller particles tend to agglomerate. Inversely larger particles are more difficult to sinter than smaller particles. Powder particle size will therefore influence the final density of the printed sample and sintered sample. The particle size of the feedstock powder will affect the pore size, pore shape and, therefore, the sinterability of the green body. Veljovic et al. also demonstrated that the sphericity and size of the pores found in Hydroxyapatite samples also impact the overall fracture toughness [153].

There are 4 main 3D printing parameters which can be changed during the printing process using this printer: roller speed, shaker speed, layer height, and nozzle temperature. Roller speed determines the smoothness of each layer and needs to change according to the amount of powder that is being deposited. Roller and shaker percentages, which indicate the percentage of total power affecting the speed, were increased and decreased until the setting which laid the smoothest powder bed was found. Shaker speed determines the amount of powder being deposited. Layer height determines the thickness of each layer. Nozzle temperature, as mentioned before, determines how much ink is sprayed on each layer. The proper shaker and roller settings were determined first, followed by the layer height and finally the adequate nozzle temperature was determined. These parameters, the approach taken for each and its effect on the final properties of the sample are described in more detail in each section. Finally, the printed samples were left in the powder bed at room temperature for a minimum of 4 hours or in a curing oven at 80 C for one hour to ensure samples were dry.

The intent of this research project was to vary and experiment with all aspects of the additive manufacturing and sintering processes. This led to the decision to use a custom-made printer for all experiments. By having a custom-made printer, we gained the ability to chance almost all parameters and analyze the effects of each in detail. Additionally, this printer allowed us to use a variety of powders without requiring a large amount of it for every print.

The main functions necessary for powder-based inkjet printing: on-demand ink jetting, powder spreading and movement in the x, y,z-axis. Interestingly, these three functions are already implemented in 2D paper ink-jet printing and Fused Deposition Modeling (FDM) plastic 3D printing. By retrofitting an FDM 3D printer with a 2D inkjet catridge and adding a powder spreading function, a powder-based printer can be made. With this concept, Van der Geest invented “Colorpod”, a powder spreading system that can be attached to a generic FDM 3D printer to have the ink jetting function with only a small modification of the electronics. With this Colorpod, complex shaped products made with sugar or polyvinyl alcohol (PVA) have been produced. However, this custom printer had not been used to build complex ceramic parts. The behavior of bioceramics during printing in this printer is not well understood.

From literature, it can be concluded that one of the most influential printing parameters on the final green density and shape of parts is layer height and therefore will be the focus of this chapter [154]–[159]. The layer height is the distance along the z-axis between each layer deposition and dictates how long the total print will take. In most powder-based inkjet printers it ranges from 15-300 μm and there are recommendations on how to choose a layer height based on your feedstock powder’s particle size. Some references suggest the optimal layer height is 3 times the average particle size [160]–[162], 2 times the particle size [163] or simply, some studies show the layer height should be larger than the largest particle size [164]–[166]. A smaller layer height generally results in a higher green density in the printed bodies. Yet once the reduction of particle size, and in turn layer height, is not limitless as the void fractions tend to increase as the size decreases[167]. Fine powders tend to agglomerate and reduce powder flowability to the extent that it is no longer printable.

Although the various phenomena detailed above are expected with our custom-made printer, the degree to which each can affect the printed part needed to be investigated. The full effect of layer height on the anisotropy of powder based printing is still not well understood although being heavily researched [144], [145], [168]–[172]. Most of these studies have been conducted on metallic materials, mostly stainless steel, with Hamano et al [171] being the exception in studying calcium sulfate moldings.

In this study, the physical properties of printed alumina with regards to layer height were optimized. The focus was on the printing parameters which traditionally has the most impact on the quality of printed components, layer height. The main desired outcomes for the green bodies were high geometrical accuracy and high relative densities. Overall condition of the samples was also considered.

3.1 Materials and Methods

3.1.1 Experimental approach

The initial step for this study was to build the 3D printer. The assembly of a jetting 3D printer required a regular polymer FDM printer and the Colorpod (Spitstec, Netherlands) system developed by Adrianus Franciscus Van Der Geest. First, the structural units of Colorpod were fabricated using the plastic FDM 3D printer (Ultimaker 2, USA). Second, the structural parts such as the powder feeder, shaker, roller and cartridge holder were assembled onto the Colorpod mother board provided by Spitstec (Figure 3.1.1.1). Third, the original plastic extruder was removed from the Ultimaker. Lastly, the Colorpod assembly was attached to the 3D Printer to replace the original extruder parts.

The equipment used for the general preparation of feedstock powder can be seen in Figure 3.1.1.2. The initial step is to weigh the different powders for their respective percentages using the scale (Ohaus, GA2000). Then, the powders can be mixed using either a magnetic hot plate (Scilogex, MS-H Pro) if coating with binder or with the tubular mixer (Turbula) if dry mixing with binder, both pictured in Figure 3.1.1.2. For coated powders, an additional step is necessary to re-pulverize the dried binder-powder combination using a ball milling machine (Pulverisette 6, Fritsch, Germany). Lastly, the powders are sieved using the 250 micron sieve prior to printing. After printing, the powder bed is cured in a vacuum oven (Across International, AccuTemp-09, USA) for a few hours or left to dry at room temperature over night depending on the material system used.

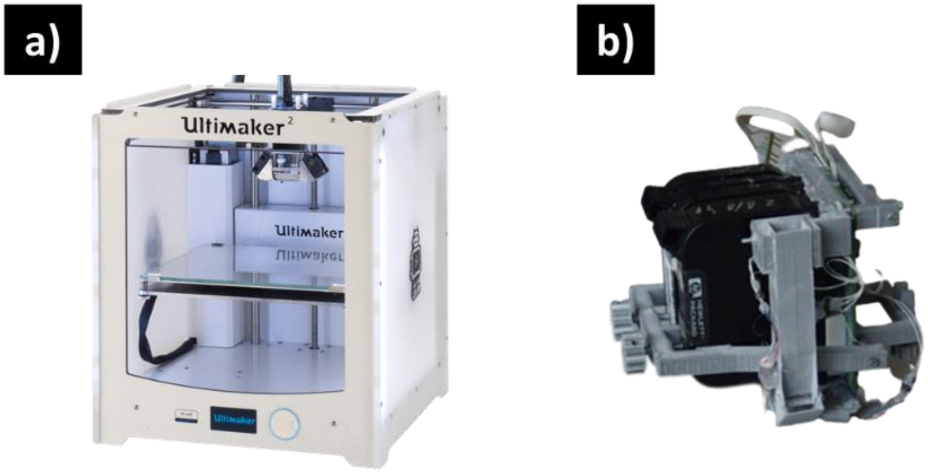

Figure 3.1.1.1: Components of custom-built printer a) Ultimaker 2 and b) Colorpod assembly.

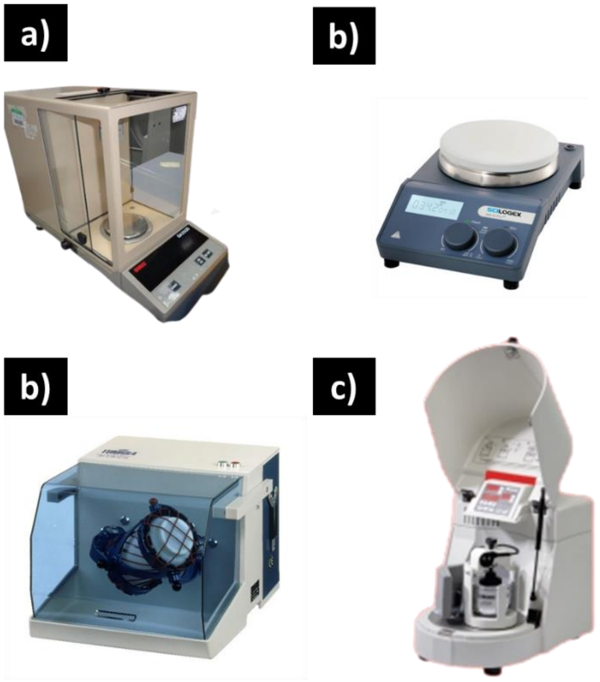

Figure 3.1.1.2: Equipment used for the fabrication of feedstock powder.

Figure 3.1.1.3: Vacuum oven used for curing.

3.1.2 Powder preparation

Calcined alumina powder with 99.2% purity (Materion, USA), maltodextrin (LD Carlson Co., USA) and powdered sugar (Wholesome Sweeteners, Inc, USA) were mixed in varying weight ratios. To find the best composition of the feedstock powder, a series of Spritz tests (Figure 3.1.2.1), were conducted. For these tests, different percentage combinations of sugar, maltodextrin and alumina powders were tested by changing the weight percent of each constituent. It was insured that alumina was always the highest weight percentage and the remaining percentage was split between the sugar and maltodextrin powders. Each combination sample was placed in a trabecular mixer for 10 minutes at 67 rpm, then, placed in small foil cups. Using a syringe, the water-based ink from the cartridge was deposited on top of the powder preparations creating a high concentration of ink in the middle while depositing small droplets around. Once the ink dried, each one was checked for hardness or a gelatin like consistency, the former being what was considered a positive result. If the consistency was gelatin like, the composition was deemed a failure. From these tests, it was concluded that the best composition was 74% alumina, 13% sugar and 13% maltodextrin, a mixture that showed to be sufficiently flowable for printing as well. This composition was used for the experiments. Four different layer heights were tested: 200, 225, 250 and 275 micron layer. At least 4 cubic samples were printed for each layer height. All other printing parameters were held constant.

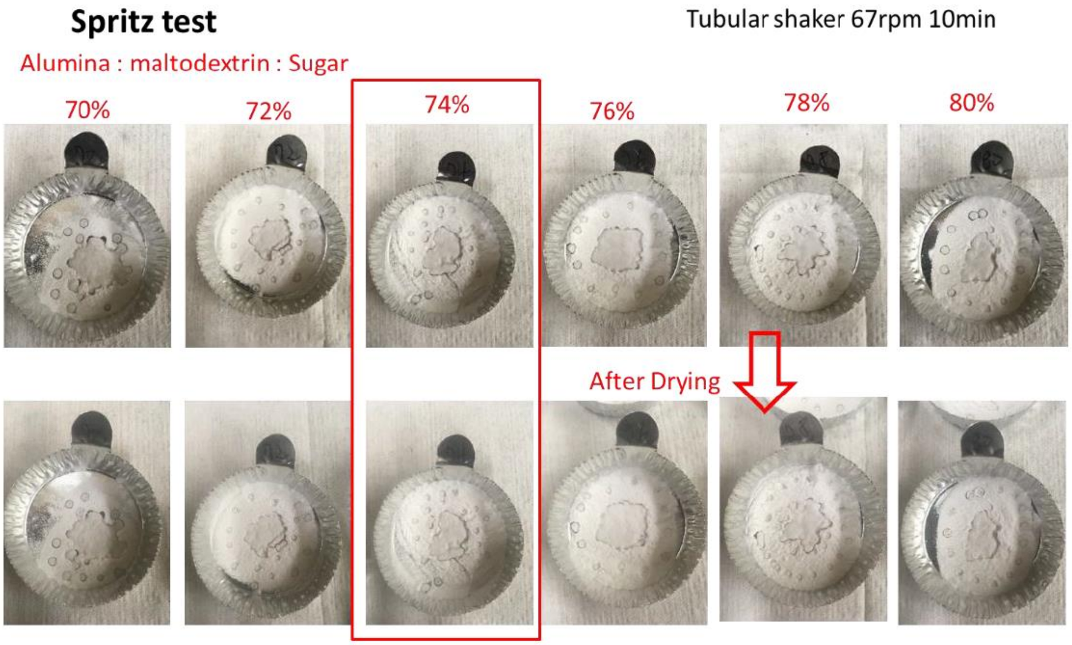

Figure 3.1.2.1: Spritz test results for alumina feedstock powder.

As-received powders were analyzed by the scanning electron microscopy (SEM), (FEI Quanta 450, USA). The particle size for alumina was analyzed using an Anton Paar, PSA 1090 particle size analyzer. The relative density of the printed specimens was evaluated either geometrically or by the Archimedes' immersion method, which required the samples to be coated with paraffin wax prior to the measurements to prevent the contact of water to the samples. Given that the feedstock powder is a combination of alumina, sugar and maltodextrin, the theoretical density of this mixture had to be calculated to be 3.23 g/cm^3 using the rule of mixtures approach:

$$(\rho_{alumina}\ x\ \%_{alumina}) + (\rho_{sugar}\ x\ \%_{sugar}) + (\rho_{maltodextrin}\ x\ \%_{maltodextrin}) = \rho_{feedstock} \quad (1)$$

When displaying data for relative density in terms of the sacrificial mold, it is being compared to this rule of mixtures calculated density not the density of alumina which is 3.95 g/cm^3. This was the approach taken in the case of all printed components containing a significant (greater than 5%) binder.

3.2 Results

The particle sizes and shapes of the as-received powders are seen below in 3.2.1. It is important to note the particle size for the alumina powder while viewing the results of the conducted experiments. The average particle size of the alumina powder is 110 microns. Two properties of the final printed parts were evaluated: green density and geometrical dimension. The Computer Aid Design (CAD) model was a 10mm cube, therefore, the length of each direction (x, y and z) in the printed green body should be 10mm (1cm). Figure 3.2.2 shows the x, y, z dimensions for each printed cube based on their respective layer height. Figure 3.2.3 shows the difference in green density values for each layer height group.

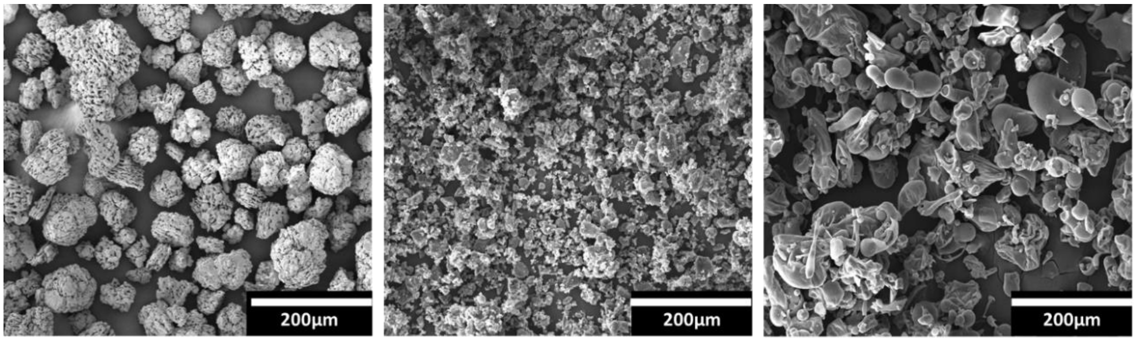

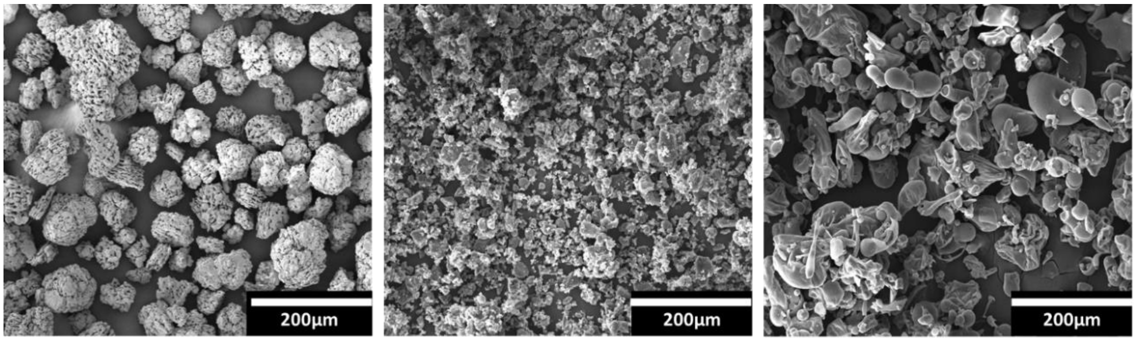

Figure 3.2.1: SEM Images of as-received powders from left to right: Alumina, sugar and maltodextrin.

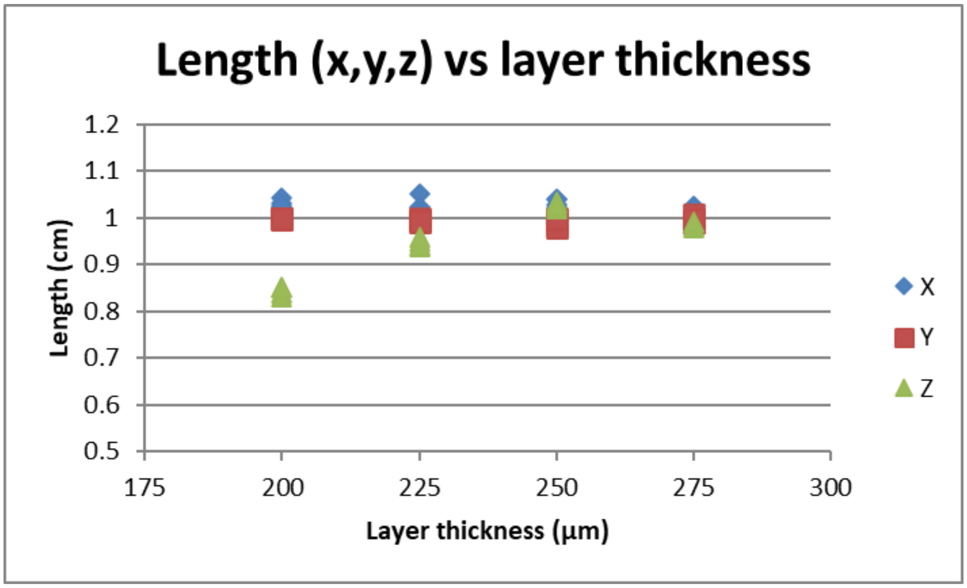

Figure 3.2.2: Dimensions for printed cubes grouped by layer height.

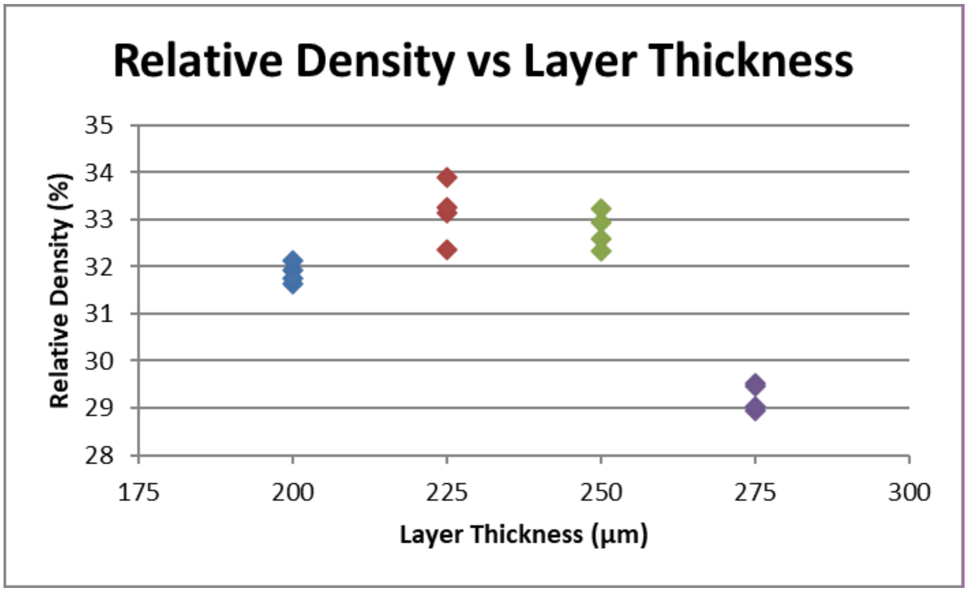

Figure 3.2.3: Green density of printed cubes based on layer height.

3.3 Discussion

In literature, it is understood that a smaller layer height leads to a higher green density. However, it can be seen in Figure 3.2.3 that the highest green density is experienced by the samples with a layer height of 225 micron. This can be attributed to the particle size of the alumina powder. To illustrate this concept, a simple diagram can be made to show how particle size and layer height can become an obstruction in the bonding of the layers. When the layer of powder is deposited, it can be assumed that the particles will fall on top of each other. If two particles with a size of 110 micron are stacked on top of each other, the total possible height is 220 microns, therefore, one layer is not thick enough to cover two powder particles. A layer height of 225 micron, on the other hand, can cover two particles and does not “cut” a particle in half. This is important because once the next layer is deposited, the roller can push the extra portion of the particles and when it is repeated along the whole surface of the powder bed, it can have some significant effects on the overall compaction of the particles.

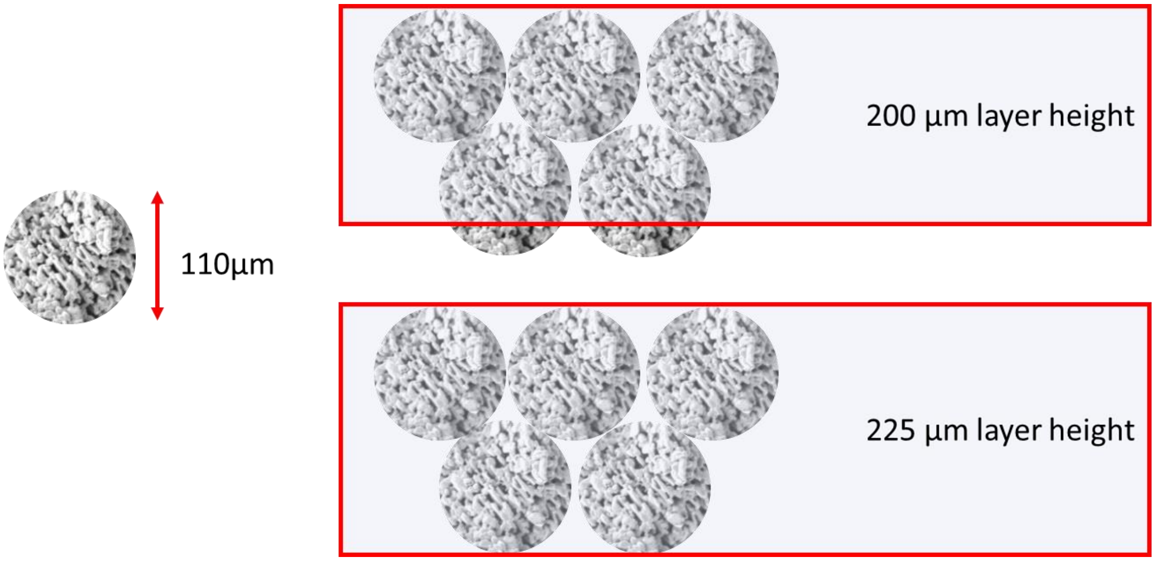

Figure 3.3.1: Particle stacking within layer for 200 and 225 microns.

Another effect that was observed is with the large layer height of 275 micron. In this case, there are too many particles stacked on top of each other making the layer too thick. When the “ink” in sprayed onto the powder bed, it cannot penetrate the whole layer effectively and results in some of the binder not being activated and, therefore, some of the particles not being bonded together. Therefore, there is a significant drop in density in the samples printed using a layer height of 275 micron.

The geometrical accuracy of printed samples using solvent jetting is often seen as an aspect of concern. Slight deviations from the CAD model dimensions were observed in the printed samples. In the table below, the average length of each layer height group is listed for each side of the cube:

Table 3.3.1: Average length for each side of printed cubes

Layer height	Avg length, x (cm)	Avg length, y (cm)	Avg length, z (cm)
200	1.03	1.00	0.85
225	1.02	0.99	0.95
250	1.03	0.99	1.03
275	1.02	1.00	0.99

Calipers when used to measure the cubes by hand, therefore the slight errors in the x and y directions can be attributed to a manual measurement error. There is a large difference in the length measured in the z direction for the layer height of 200 micron. The lengths for each sample in the group were measured as 0.841, 0.842, 0.852 and 0.850 which indicates that this was not a measurement error. The shortened height is due to the phenomenon illustrated in Figure 3.3.1. Because the layer height is smaller than two particle layers, there is more “ink” or solvent, deposited on the powder particles. The solvent is heavier and pushes the printed layers down along with gravity. The over saturation of the solvent in the printed section makes the overall cube shorter in the z direction.

3.4 Chapter Summary

The custom-made printer used in this study follows similar patterns as other solvent jetting machines. The effect of the layer height was investigated. It was discovered that the optimal setting is not only dependent on the height of the layer but also on the particle size of the feedstock powder. A smaller layer height does not necessarily result in a higher density. Additionally, the geometrical accuracy decreases once the lower threshold is passed.

For future experiments, a quick optimization of layer height will be conducted prior to investigating any other experimental parameters if a different feedstock is being used. When using this specific alumina powder, the layer height that will be used is 225 microns if the desired outcome is higher density.

4 SINTERING OPTIMIZATION OF SOLVENT JETTED SAMPLES

Increasing the sinterability will lead to higher green density in printed bodies and therefore, higher mechanical strength. It is important to understand the sintering mechanics of a powder compact as this can aid in printing an ideal component. An extensive investigation on how to the particle interactions in the powder bed and green body could affect the sintering process was conducted. Additionally, the continuum sintering model is described in regard to how it can be used to model the densification behavior printed samples.

The level of porosity in a green (prior to sintering) body can affect sinterability. When all other parameters are held constant, a higher green density results in a higher sintered density [173]. Higher densities mean higher amounts of interparticle contacts and less or smaller initial pores. In fact, it is common to apply pressure prior to sintering to leverage these benefits. It is also common to use loose powder sintering (no pressure) when a highly porous component is desired. At low initial packing densities, particles bond to form a long-chain open pore structures but usually fail to fully densify [174]. The influence of the green state on the spark plasma sintering of alumina was heavily studied by Aman et al [175]. It was concluded that narrowing pore size distribution and reducing pore size can significantly favor sintering. Green density gradients should also be considered as differences in green density along the component can leave to warpage during sintering [176], [177]. Additional attention needs to be given to the sintering behavior of printed ceramics given that it might differ than the sintering of traditionally manufactured ceramics.

Another parameter that can be controlled is the dwell time during sintering. This is typically the time that the sample is held at the highest temperature of the sintering cycle. As would be expected, the longer a sample is held at high temperature, the more it densifies.

However, with bioceramics, special attention needs to be given to phase transformations that result from long dwell times as these could have several negative effects on the final bulk density of the part.

4.1 Materials and Methods

4.1.1 Experimental approach

The effect of green density and sintering dwell time were studied in this work. Printing parameters were varied (based on results produced in Chapter 3) to produce different levels of green density for the same material system and understand how green density of printed bodies affect the final densities. The printing variables chosen were cartridge temperature and layer height. Then, these printed samples with varying green densities were held at the maximum temperature for 10 hours and 48 hours to understand the effect longer sintering times of these samples. The tube furnace used for this study can be seen in Figure 4.1.1.1. Since the printed samples are very fragile, the green densities were estimated using a geometrical approach. The bulk densities of the sintered samples were estimated using the Archimedes' immersion method following ASTM standard C373-18, which required the samples to be coated with paraffin wax prior to the measurements.

For the analytical model of sintering, it is necessary to conduct a dilatometry test on a printed specimen. The configuration with the highest final density was chosen for this study and subject to sintering in the dilatometer (Anther, Unitherm 1161, USA) pictured below (Figure 4.1.1.2). In future chapters, this equipment was utilized to find sintering parameters for the modeling of sintering as well.

Figure 4.1.1.1: Tube furnace used for free sintering.

Figure 4.1.1.2: Dilatometry System.

4.1.2 Powder preparation

Alumina (A16SG, α-Al2O3, 99.8% pure, Alcoa, Pittsburgh, PA) was used for this study. Alumina is a material that is generally well understood, and its powders are available in a variety of morphologies and sizes. The water-soluble polyethylene oxide (PEO) based binder used consists of >95wt% PEO, <3wt% fumed silica and <1wt% Calcium (PolyOx WSR N10, Dow Chemical Company, Midland, MI), and will be referred to as PEO.

First, solutions of various PEO concentrations were made with deionized (DI) water; a 5 wt% PEO solution refers to 5g of PEO to 100g of DI water. Second, the alumina powder was suspended in the PEO solutions. Third, the mixtures were homogenized by a stirrer and dried simultaneously at 35 ºC for 48hrs on a magnetic hot plate. Fourth, the dried alumina slurries were milled using Zirconia balls (diameter: 20mm) at 150rpm for 30min by high energy ball milling (Pulverisette 6, Fritsch, Germany). Lastly, the pulverized alumina powders were sieved using a 250μm sieve. After creating several powder mixtures of different concentrations (3wt%, 5wt%, 7wt%, and 8.5wt%) of PEO solutions with alumina powders; these were tested by spraying water-based ink on a simulated partial powder bed and visually inspected for the degree of consolidation (see Figure 3.1.2.1) . The 8.5wt% solution was found to hold alumina particles together better and was, therefore, used in the rest of this study. After printing, the samples were left to dry at room temperature for at least six hours.

4.1.3 Analytical modeling of sintering

The sintering behavior of the printed samples can be analytically modeled using the continuum theory of sintering. Given that the binder is expected to decompose in the early stages of sintering, there is only one material system than remains and that should be considered for the sintering model. This one material system allows for the conservation of mass law to be used in our free sintering condition.

The mechanics of sintering for powder components is described using the constitutive relationship of the continuum theory of sintering proposed by Olevsky [123]:

$$\sigma_{ij} = \frac{\sigma(W)}{W}\left[\varphi\dot{\varepsilon}_{ij} + \left(\psi - \frac{1}{3}\varphi\right)\dot{e}\delta_{ij}\right] + P_L\delta_{ij} \tag{2}$$

where σ_{ij} (Pa) are the stress tensor components, $\sigma(W)$ (Pa) is the effective equivalent stress that determines the constitutive behavior of a porous material. W (s^{-1}) is the equivalent strain rate, $\dot{\varepsilon}_{ij}$ (s^{-1}) represents the strain rate tensor components, φ and ψ are, respectively, the normalized shear and bulk viscosities, P_L (Pa) the sintering stress, and δ_{ij} the Kroenecker delta.

This framework can be used to predict the final porosity of the printed samples and shrinkage during sintering. In this study, it will be used to estimate the amount of dwell time that is required to achieve a specific level of porosity. For example, determine the amount of dwell time required to attain full density in the printed component.

4.2 Results

4.2.1 Effect of green density and dwell time on sintered density

A total of 5 cubes from each configuration were printed. After depowdering, the green density of each cube was measured, and all successful prints were taken into account. The relationship between the green density and sintered density for printed samples can be seen in Figure 4.2.1.1. As the green density increased, the sintered density also increased in a linear fashion. Although there are no data samples in between the densities of 1.2 g/cm^3 and 1.5

g/cm^3, it can be safely assumed that those data points would follow the same trend time as was established by previous data points.

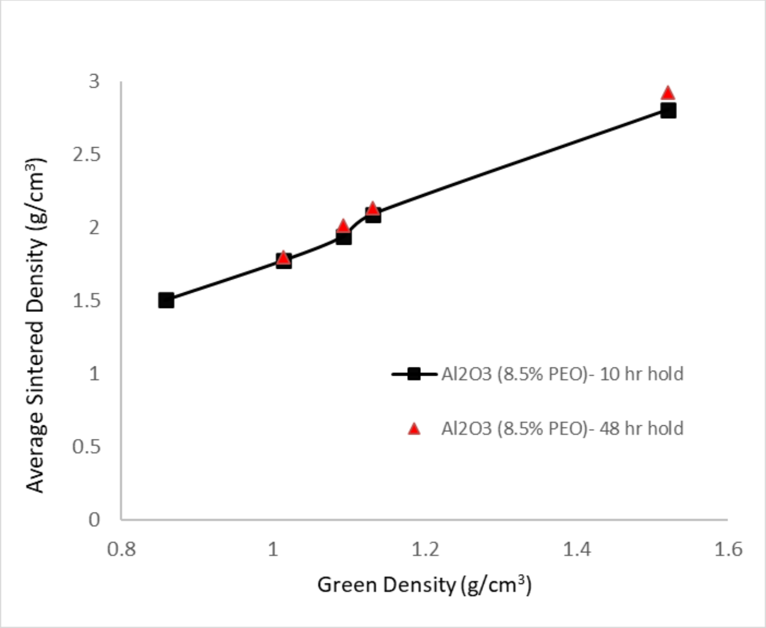

Figure 4.2.1.1: Green and sintered density relationship in printed samples at 10 hour and 48 hour holding times.

In the experimental results (Figure 4.2.1.1), it was observed that the longer holding times did not significantly improve the sintered density. For example, in the samples beginning with a relative green bulk density of 39% only say an increase of 2.5% in final sintered density when increasing the holding time from 10 hours to 48 hours. However, when analyzing the samples via Scanning Electron Microscopy (SEM), an important phenomenon was identified. The microstructural images (Figure 4.2.1.2) show the difference in microstructure between the 10 hour and 48 hour holding time (left and right, respectively). As can be seen, the average grain sizes are 10 μm for the shorter dwell time and 25 μm for the longer dwell time. A materials' grain size is inversely related to its mechanical properties; therefore, this is not a desired effect. A decrease in compressive strength is expected and will be discussed in the following chapter.

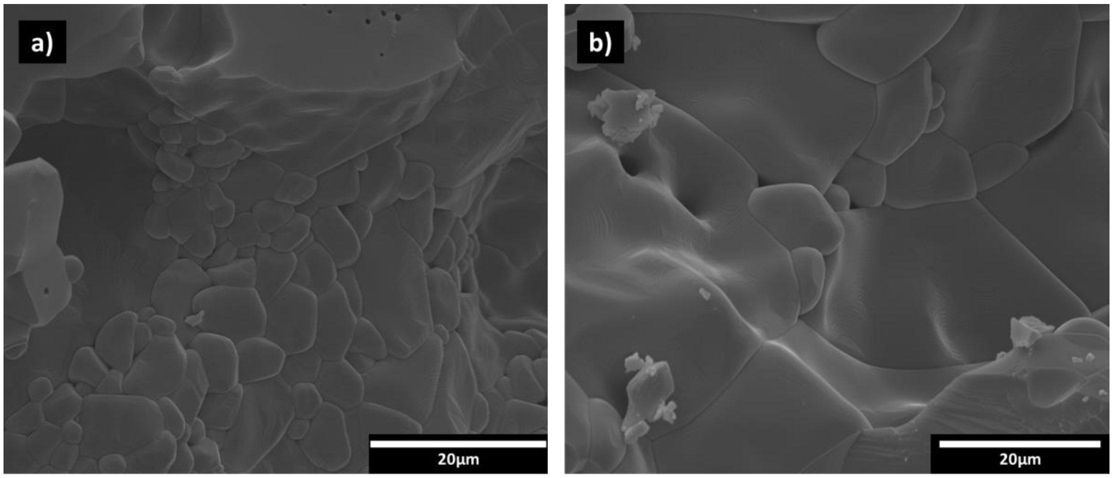

Figure 4.2.1.2: SEM Images of sintered samples showing the difference in grain sizes after increasing the holding time from 10 hours to 48 hours during sintering.

4.2.2 Analytical model for free sintering of printed samples

The printing configuration that yielded a final sintered density of 70.9% was used in the creation of this analytical sintering model. The effective stress- equivalent strain rate (W) relationship is dependent on the type of consolidation process you are using and, in turn, the type of deformation. Table 4.2.2.1 below shows the value of σ(w) for each type of consolidation. Free sintering was used in this research and, therefore, the linear viscous relationship is used in all calculations. Several methods of modeling the sintering of ceramics from literature were used as reference for this analysis as well [178]–[182].

Table 4.2.2.1: Definition of effective Stress by deformation type.

Deformation Type	**Sintering Process**	**$\sigma(w)$**
Linear viscous	Free sintering	$2\eta_0 w$
Plastic	Cold Pressing	σ_y
Power-law creep	Hot deformation of crystalline materials	Aw^m

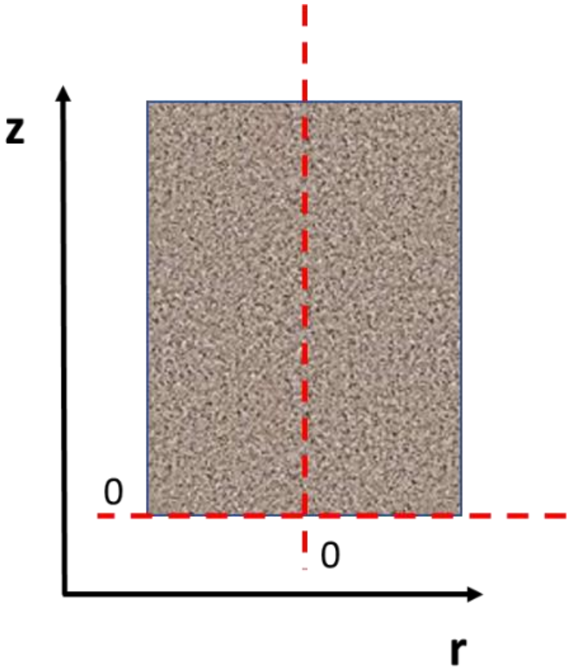

Figure 4.2.2.1: Axes and origin definition for analysis.

Substituting the value for σ(w) in the main equation for the free sintering case used in this study can be written as,

$$\sigma_{ij} = 2\eta_0 \left[\varphi \dot{\varepsilon}_{ij} + \left(\psi - \frac{1}{3}\varphi\right) \dot{e}\right] + P_L \tag{3}$$

Where, η_0 is the shear viscosity of the fully dense material. For this analysis, the axes and reference origins are defined as illustrated in Figure 4.2.2.1. By defining i,j as r,z, the external stresses applied in each direction can be written as,

$$\sigma_r = 2\eta_0 \left[\varphi\dot{\varepsilon}_r + \left(\psi - \frac{1}{3}\varphi\right)\dot{e}\right] + P_L$$

$$\sigma_z = 2\eta_0 \left[\varphi\dot{\varepsilon}_z + \left(\psi - \frac{1}{3}\varphi\right)\dot{e}\right] + P_L$$

Using the relationships for hydrostatic pressure (P) to external stresses (σ_r, σ_z), the latter equations can be re-written as,

$$P = \frac{\sigma_z + 2\sigma_r}{3}$$

$$P = \frac{1}{3}\left\{2\eta_0 \left[\varphi(\dot{\varepsilon}_z + 2\dot{\varepsilon}_r) + 3\left(\psi - \frac{1}{3}\varphi\right)\dot{e}\right]\right\} + P_L$$

Simplifying,

$$P = 2\eta_0\psi\dot{e} + P_L$$

Because there are no external stresses in free sintering, the hydrostatic pressure P is equal to 0, substituting this in and solving for P_L, we get an equation for sintering stress,

$$P_L = -2\eta_0\psi\dot{e} \qquad (4)$$

For this research the equation is most helpful in terms of porosity. To accomplish this, the following relationships are considered:

$$\dot{e} = -\frac{P_L}{2\eta_0\psi}$$

$$\dot{e} = \frac{\dot{\theta}}{1-\theta}$$

$$P_L = \frac{3\alpha}{2r_0}(1-\theta)^2$$

$$\psi = \frac{2}{3}\frac{(1-\theta)^3}{\theta}$$

where,

$\theta = Porosity$

$\dot{\theta} = Change\ in\ Porosity$

$\alpha = Surface\ tension$

$r_0 = Particle\ radius$

Using these relationships, we can write the main equation for this study in terms of porosity

$$\frac{\dot{\theta}}{1-\theta} = \frac{\frac{3\alpha}{2r_0}(1-\theta)^2}{2\eta_0 * \frac{2}{3}\frac{(1-\theta)^3}{\theta}}$$

$$\frac{\dot{\theta}}{\theta} = -\frac{9}{8}\frac{\alpha}{r_0\eta_0}$$

The solution of this differential equation can be written as,

$$\frac{\theta}{\theta_i} = \exp\left(-\int_0^t \frac{9}{8}\frac{\alpha}{r_0\eta_0}dt\right)$$

Solving for porosity,

$$\theta = \theta_i \exp\left(-\int_0^t \frac{9}{8}\frac{\alpha}{r_0\eta_0}dt\right) \tag{5}$$

where,

$\theta_i = Initial\ porosity$

$t = Time$

If shear viscosity η_0 can be expressed as

$$\eta_0 = A_0 \exp\left(\frac{Q}{RT}\right)$$

Then the following expression can be formulated for specific sintering time and porosity kinetics,

$$\theta = \theta_i \exp(-\tau_s);\ \tau_s = \int_0^t \frac{9}{8} \frac{\alpha}{r_0 A_0 \exp\left(\frac{Q}{RT}\right)} dt \tag{6}$$

To apply equation 6 to the current material system and sintering parameters, a dilatometry test is necessary [183]–[185]. The dilatometry was done on a printed ALCOA sample using optimized parameters. The cycle consisted of a ramp up to 1000°C at a rate of 10°C per minute followed by a 10-minute hold for stabilization, then of another ramp up to 1600°C at a rate of 5°C per minute followed by a four hour hold at that maximum temperature.

The specific time of sintering (equation 7) was considered for the section of sintering where temperature is held constant (1600°C for 4 hours). If temperature is constant, then particle radius (r_0) is constant and shear viscosity (η_0) is also constant. Applying these two assumptions, the equation simplifies to,

$$\tau_s = \frac{9}{8} \frac{\alpha}{r_0 \eta_0} t \tag{7}$$

Inserting this into equation 4,

$$\theta = \theta_i \exp\left(-\frac{9}{8} \frac{\alpha}{r_0 \eta_0} t\right) \tag{8}$$

Using the dilatometry results, porosity during the temperature hold is plotted over time to show a constant linear decay. The natural log of these points can then be plotted to form a linear relationship with the porosity values as seen when writing the equation as,

$$ln\theta = \ln\theta_i - \frac{9}{8}\frac{\alpha}{r_0\eta_0}t \qquad (9)$$

Because this is a linear equation, the terms preceding t are equal to the slope, therefore, the slope of the line created by the natural log of porosity values can be found. As seen in Figure 4.2.2.2, a trendline can be fitted to within a 2% accuracy to the natural log line and from this equation the slope is found to be 0.0003 and this value is taken as the value for $\frac{9}{8}\frac{\alpha}{r_0\eta_0}$.

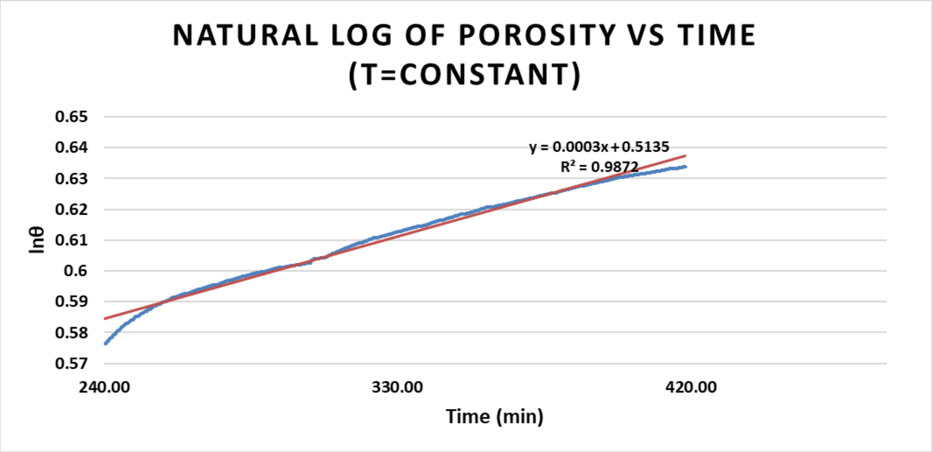

Figure 4.2.2.2: Natural log of porosity vs time of the dilatometry result

Substituting the new slope value back into equation 8,

$$\theta = \theta_i \exp(-0.0003t\ ) \qquad (10)$$

Initial porosity is known and, therefore, time is the only variable. Inputting the time starting from zero to 30,000 minutes and plotting these values gives a clear exponential decrease of porosity until reaching an asymptote close to zero. Using equation 10, one can determine the time required to reach a desired porosity. For example, to reach 1% porosity from our initial porosity of 56.2% the time necessary is 13429.64 minutes or about 9 days.

4.3 Discussion

From the experiments conducted on the effect of green density on the final sintered density of the printed samples, it can be concluded that a higher green density leads to a higher sintered density as is the case with samples produced via traditional methods. Although this was expected, it is important to emphasize that this relationship is linear and can does not seem to reach a limit. One interesting phenomenon identified in this study is the neutral effect holding time has on the final sintered density. Having a maximum of 3% increase in final density with a 38 hour increase in holding time shows that the printed samples reach a limit on the amount they can densify at the given temperature. Furthermore, the longer holding times lead to an increase in grain growth which is likely to severely impact the mechanical properties of printed parts.

As calculated in Section 5.2.7, to reach 1% porosity, the sample needed to be sintered for 9 days. Clearly, this time is excessively long for practical implementation and would lead to extreme grain growth. Thus, the modeling results indicate the limitation of the scaffold material’s sinterability. It is evident that the experimentally obtained results correspond to the practical maximum of the porous alumina scaffold’s densification. No further experimentation, targeting possibly higher post-sintering density levels, is therefore necessary. The theoretical modeling performed allowed us to predict the maximum densification achievable for printed samples using this powder 3D printing technique via free sintering. Furthermore, it allows for the prediction of sintering time based on a desired porosity value. In this study, the maximum holding time in the scaffold samples was 48 hours and full density was not achieved. This model predicted this as it indicates that in order to get a fully dense material, the holding time must be at least 15 days which is not a realistic time for production of these scaffolds. In the event that the goal is to mimic a 40% porous cancellous bone for example, then this model can indicate how long the temperature hold should be to achieve that porosity in the scaffold being produced. This is especially convenient for bone scaffolds given that the goal is to mimic the bone exactly and the ability to tailor porosity levels becomes crucial.

4.4 Chapter summary

In this chapter, a series of experiments were conducted to determine the effect of initial green density and sintering holding time on the final density of these printed parts. It was found that initial green density linearly relates to the sintered density leading to a higher final density whenever the sample had a higher initial density. When it comes to the holding time during the sintering cycle, a longer dwell does not lead to significantly higher densities. In fact, it results in a detrimental promotion of grain growth.

To predict the final porosity of a printed part is most useful when attempting to mimic native bone. Here, an analytical model of sintering was used to predict the amount of time necessary to achieve a porosity of 1 percent. The results indicate that using the current material system and sintering temperature, this desired outcome would require 9 days of holding time which is not only unrealistic but also extremely detrimental to the mechanical properties of the printed part.

5 DIRECT SOLVENT JETTING AND SINTERING OF LOAD BEARING SCAFFOLDS USING NANO-SIZED FEEDSTOCK POWDER

The feedstock powder used for printing has a significant effect on the characteristics of the printed part, particularly when using powder-based printing methods. Powder morphology, size and size distribution all play a role in the quality of the final part and need to be evaluated to ensure the highest density in the printed component. The shape, or morphology, of particles also affects sintering yet the correlation between sphericity and sinterability is not as clear as the size dependency[186]–[188]. Non spherical or elongated particles have a greater surface area available for sintering, yet they often result in lower green densities than spherical powders. The initial particle shape also governs the relationship between neck size, shrinkage and surface area.

Microporosity in scaffolds is beneficial for bone regrowth. Additionally, the highly porous ceramic parts made by SJ often have post-sintering problems consisting of low final densities (or even inability to sinter) and related low mechanical strength. The strength of porous parts is also dependent on the microscopic structure. As was mentioned in the introductory chapter, a smaller grain size results in higher compressive strength. However, feedstock powder for SJ and all powder-based methods is traditionally limited to micron sized powder and often times required long sintering times leading to a large grain growth. An approach looking at the intrinsic features of the printed components is proposed. When the macroscopic component geometry is kept constant by using the same computer-aided design (CAD) model, only 4 characteristics of the intrinsic porous structure will influence final sintered properties: pore size, neck size, strut density and grain size. A powder preparation method using nano-sized particles was developed to address these four factors and is discussed in this chapter.

In the initial trials of printing via SJ, it was observed that sintering was being inhibited. The cause of this inhibition was not clear, but it was hypothesized that the dynamics in the powder bed and after printing may be causing this phenomenon of “un-sinterable” components. Another hypothesis was that the green density of printed parts was below the threshold of 60% traditionally desired for sintering of slip casted samples or ceramic pore-forms for example. The goal of this study was to create a powder preparation method that allows for nano sized particles because nano sized particles promote sintering as was explained in section 5. To understand the effect of different preparation methods, the Solvent Jetting on Coated (SJC) and Solvent Jetting on Granulated (SJG) powder preparation methods were investigated.

Moreover, regardless of the method chosen, a modeling component is necessary. Sintering is required as a post-processing step in the printing of ceramics and some level of shrinkage is always present during sintering. This shrinkage might differ depending on the powder preparation method used. Therefore, the shrinkage that happens during the sintering process must be evaluated in order to reverse engineer the initial geometry required to achieve a desired final shape.

5.1 Materials and Methods

The porous ceramic scaffolds were fabricated using the following steps. To start, the effect of various printing parameters was investigated to understand the degree to which each of these impacted the final component using a custom-made 3D printer. As discussed in Chapter 3, optimization of printing parameters must be conducted whenever a different material is used and, in this study, the same alumina powder was used but also a different zirconia powder. Because it was a custom device, parameters from literature were not directly applicable to our work. Then, the intrinsic porosity was optimized along with the chemical and physical properties of the powder and binder. Standard alumina cubes without designed macro channels were fabricated with various 3D printing conditions and binder concentrations. After sintering, the alumina cubes were evaluated in terms of pore size, grain size, sintered density, and compressive strength. Lastly, a scaffold with designed pore channels was printed and sintered under the optimized conditions for the ideal intrinsic porous structure. In this way, a bone scaffold with hierarchical pore size can be easily fabricated via the simple solvent jetting method.

5.1.1 Powder Processing

Nano-alumina (A16SG, α-Al2O3, 99.8% pure, Alcoa, Pittsburgh, PA) and micron-alumina (AA-18, α-Al2O3 > 99.9%, Sumitomo Chemical, Japan) were used for this study. The granulation and coating processes are similar for nano and micron-sized powders. The starting powder particle size determines the final form of powders; nano particles result in granules, and micron size powders result in coated particles. The two types of resulting powder (granule versus coated) are confirmed by comparing the SEM images prior to and after the procedure described here. The water-soluble polyethylene oxide (PEO) based binder used consists of >95wt% PEO, <3wt% fumed silica and <1wt% Calcium (PolyOx WSR N10, Dow Chemical Company, Midland, MI), therefore it will be referred to as PEO.

First, solutions of various PEO concentrations were made with deionized (DI) water; a 5 wt% PEO solution refers to 5g of PEO to 100g of DI water. Second, nano and micron-sized alumina were suspended in the PEO solutions. Third, the mixtures were homogenized by a stirrer and dried simultaneously at 35 ºC for 48hrs on a hot plate. Fourth, the dried alumina slurries were milled using Zirconia balls (diameter: 20mm) at 150rpm for 30min by high energy ball milling (Pulverisette 6, Fritsch, Germany). Lastly, the resulting Nano-alumina Granules (NG) and Micron-alumina powders which were Coated (MC) were sieved using a 250μm sieve. After creating several powder mixtures of different concentrations (3wt%, 5wt%, 7wt%, and 8.5wt%) of PEO solutions with alumina powders; these were tested by spraying water-based ink on a simulated partial powder bed and visually checking the degree of consolidation. The 8.5wt% and 7wt% of PEO solutions were found to hold alumina particles together better in nano-alumina and micron-alumina powders, respectively, and were, therefore, used in the rest of this study. Under the same printing conditions, lower binder concentrations of PEO resulted in the printed part crumbling.

The theoretical density of the granule was estimated using the rule-of-mixtures. The theoretical densities of NG granules with 8.5wt% PEO and MC with 7 wt% PEO were 3.48g/cm3 and 3.55 g/cm3, respectively. The relative tap densities of NG granules with 8.5 wt% PEO and MC with 7 wt% PEO were 37.35 % and 58.40 %, respectively.

5.1.2 Printing- Solvent Jetting

Two types of alumina samples were fabricated. Cube-shaped samples were printed with nominal dimensions of 10mm x10mm x 10mm for the optimization of intrinsic porosity, densification, and mechanical strength, while cylindrical scaffolds with designed macro-channels (nominal dimensions of 12mm dia x 12mm) were fabricated to test the porosity, ability to print complex shapes and the compressive stress after sintering. During the research work for chapter 4, some of the necessary configurations for this study were produced, therefore, the same data will be reported here. However, different aspects of the samples will be analyzed. In chapter 4, the focus was on green and sintered density, whereas here we focus on particle interaction and mechanical strength.

The spreading of the water-based ink induces the PEO to dissolve resulting in adhesion bonding between adjacent particles in the NG and MC powders. The green parts, that had enough green strength to allow sample handing, were used for post-processing and analysis. In some cases, the green parts were not sufficiently strong to be depowdered and where discarded.

5.1.3 Debinding and Sintering

Thermogravimetric analysis (TGA) of the PEO was conducted by SDT Q600 (TA Instruments, USA), up to 1000 ºC with heating rate of 5 ºC/min, to determine the cycle of debinding explained below. The TGA of the solvent ink was also conducted to ensure the diethylene glycol in this ink is removed from printed samples during debinding. The debinding and sintering were achieved in one step using a conventional tube furnace in the air (GSL-1700X-KS-UL-60, MTI, Richmond, CA). The heating cycle used was: 20 ºC – 200 ºC with 5 ºC/min, holding at 200 ºC for 20 min, 200 ºC to 300 ºC with 10 ºC/min, holding at 300 ºC for 60 min, 300ºC – 600ºC with 5ºC/min, and holding at 600 ºC for 20 min, 600 ºC -1000 ºC with 5 ºC/min and 1000 ºC to desired sintering temperature with 5 ºC/min. The initial heating and holding times up to 600 ºC is the debinding cycle for the PEO. The specimens were held at the maximum sintering temperature for various holding times (10hrs, 24 hrs or 48 hrs) and the cooling rate down to room temperature was 5 ºC/min. The sintering temperature of the printed samples was set to 1700 ºC which is the maximum temperature for this furnace. The highest temperature was desirable because the most densification with the lowest grain growth was needed to achieve the highest strength. An overview of the powder preparation, printing and sintering process is illustrated here:

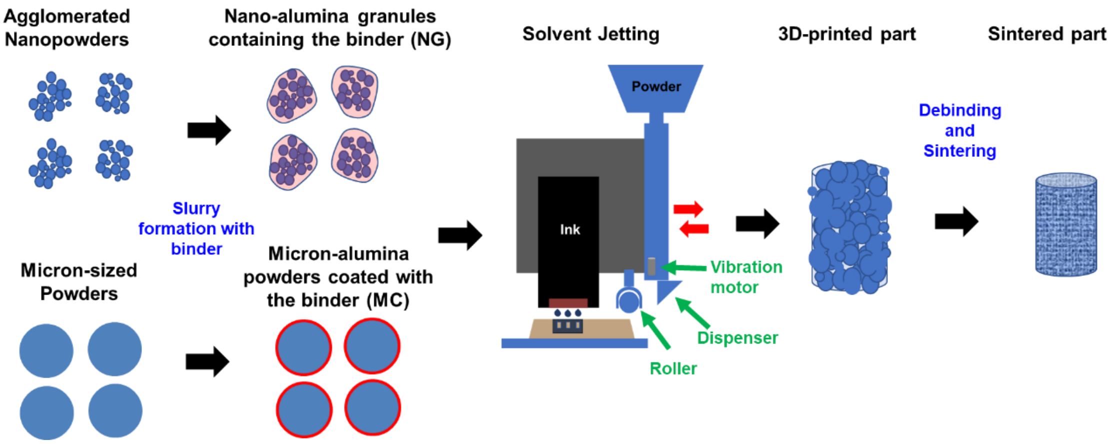

Figure 5.1.3.1: Schematics of processing of porous structure by solvent jetting (SJ). Upper path: solvent jetting on granulated feedstock containing binder (SJG). Lower path: solvent jetting on feedstock containing coated powder (SJC).

5.1.4 Characterization

The crystal structures of the powders and sintered parts were evaluated by X-ray diffraction (XRD) (Bruker D-8 diffractometer, MA, USA), utilizing CuKα radiation at room temperature. The green densities of the cylinder-shaped printed samples were determined via the geometrical measurement method. The bulk densities of the sintered samples were estimated using the Archimedes' immersion method following ASTM standard C373-18. The compression strengths of the cube-shaped (10mmx10mmx10mm) and scaffold-shaped (10mmx10mmdia) sintered samples were obtained using a universal testing machine (5900, Instron, USA), 1kN load cell. The compression testing was conducted at room temperature with a loading rate of 1 mm/sec. The size of the powder and of the fractured specimens' particles, grains and pores were analyzed using a scanning electron microscopy (SEM), (FEI Quanta 450, USA).

5.1.5 Sintering Model

The sintering behavior of the printed powder was simulated using the continuum theory of sintering which has been embedded in a FEM (finite element model) software. Given than the binder is expected to decompose in the early stages of sintering, there is only one material system than remains and that should be considered for the sintering model. This one material system allows for the conservation of mass law to be used.

The mechanics of sintering for powder components is described using the constitutive relationship of the continuum theory of sintering proposed by Olevsky [123]:

$$\sigma_{ij} = \frac{\sigma(W)}{W}\left[\varphi\dot{\varepsilon}_{ij} + \left(\psi - \frac{1}{3}\varphi\right)\dot{e}\delta_{ij}\right] + P_L\delta_{ij} \tag{2}$$

where σ_{ij} (Pa) are the stress tensor components, $\sigma(W)$ (Pa) is the effective equivalent stress that determines the constitutive behavior of a porous material. W (s^{-1}) is the equivalent strain rate, $\dot{\varepsilon}_{ij}$ (s^{-1}) represents the strain rate tensor components, φ and ψ are, respectively, the normalized shear and bulk viscosities, P_L (Pa) the sintering stress, and δ_{ij} the Kroenecker delta.

This framework was used in chapter 4 for the modeling of free sintering and the prediction of final porosity levels. In this chapter, it will be embedded in a finite element software (COMSOL Physics) to simulate the densification of these printed cubes and biomimetic scaffold.

5.2 Results

A new type of feedstock powder was created using the SJG method. The results section will outline the characterization of the as-received powders as well as the processed powders in at each step of the process. It is important to understand the microstructure prior to printing, after printing, after debinding and after sintering. Because the material used is a ceramic, it is also important to verify the phase of the ceramic has not been changed due to the ink or the sintering process. The analysis was done for both the micron coated (MC) and nano granulated (NG) powders. The final production of a biomimetic scaffold will also be detailed using SEM and mechanical testing but was only printed with the NG powder as it produced higher density samples. Results will also be reported for the theoretical analysis and finite element simulation created for the sintering of printed ceramic samples.

5.2.1 Powder Characterization

First, the as-received nano-alumina powders are agglomerated and have an average particle size of ~200 nm (Figure 5.2.1.1(a), (b)). Then, as can be seen in Figure 5.2.1.1(d), as-received micron-alumina powders are not agglomerated and have an average particle size of ~18 μm. After processing the powders (section 5.1.1), the average sizes and standard deviations (SD) of NG and MC were ~15.60 μm and 16.53 μm (Figure 5.2.1.1(c)) and 21.91 μm and 11.45 μm (Figure 5.2.1.1(e) and (f)), respectively, which were determined using statistical SEM image analysis (N = 350). The NG powders consisted of agglomerates (Figure 5.2.1.1(c)). Conversely, as shown in Figure 5.2.1.1 (e) and (f), the majority of the alumina MC powder consisted of discrete particles deagglomerated during milling with only a few agglomerates remaining.

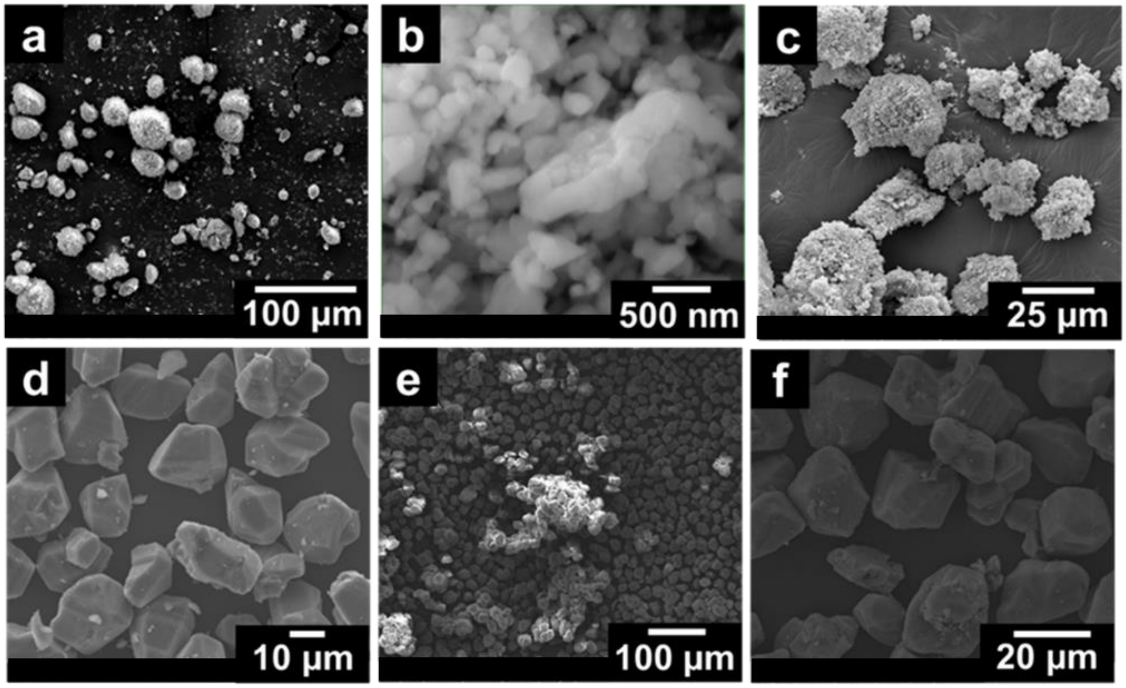

Figure 5.2.1.1: SEM images of (a) as-received nano-alumina powders, (b) zoomed image of (a), (c) nano-alumina granules containing binder (NG) with 8.5 wt% PEO, (d) as-received micron-alumina powders, (e) micron-alumina powders coated with the binder (MC) with 7 wt% PEO.

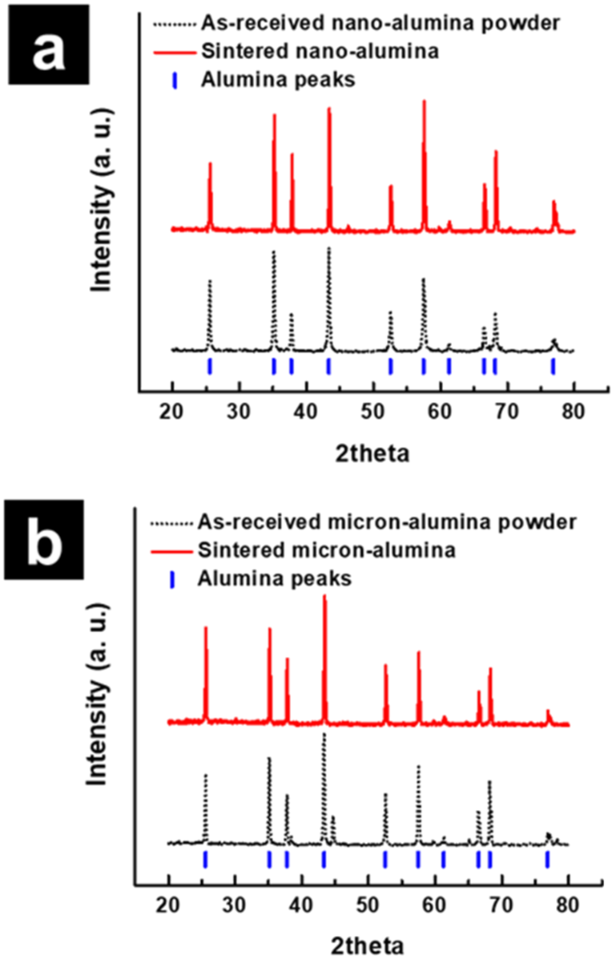

Figure 5.2.1.2: X-ray diffraction results of nano-alumina (a) and micron-alumina (b), before and after sintering. Alumina peak locations were shown at the bottom of each plot.

Figure 5.2.1.2 (a) and (b) show the XRD analysis results for both nano and micron-alumina before and after sintering at 1700 ºC for 10 hrs. This indicates that both remained as alpha-alumina powders, and the crystal structure was not changed during sintering except one impurity peak at 44.7 deg for the micron-alumina powder which was removed after sintering. Also, the XRD results (Figure 5.2.1.2 (a) and (b)) showed that there is no change of crystal structure in the alumina sample after debinding/sintering compared to the as-received alumina powder, which means that there is only alumina present (binder was completely removed) and that the sintering process did not affect the crystal structure of the final alumina part.

5.2.2 Debinding Analysis

One of the most critical procedures in using 3DP is the debinding step to remove the binder using heat. In the SJG and SJC methods, the following binders were used: 1. diethylene-glycol in solvent ink, 2. PEO used for granulation or coating. The amount of diethylene-glycol in solvent ink was very small (8.3vol%) and the jetted solvent from the ink cartridge consisted mostly of water (83.4vol%), therefore, TGA was only conducted on PEO to find the optimal debinding temperature. The TGA results of PEO are shown in Figure 5.2.2.1. The decomposition starts at ~ 300 ºC and continues until 410 ºC, with rapid decomposition occurring near 387 ºC. According to this analysis, the debinding conditions were set to be 300 ºC for 1hr to reduce the gas pressure during rapid decomposition at 387 ºC. After this stage, the heating rate from 300 ºC to 600 ºC was set at 5 ºC/min. If the binder used did not evaporate as easily, there were measures that could have been taken such as: slowing the heating rate down, increasing holding time at a critical temperature or adding an extra debinding step. However, for our geometry and printing method, the parts were sufficiently porous to let the binder decompose and release the gases through the porosity.

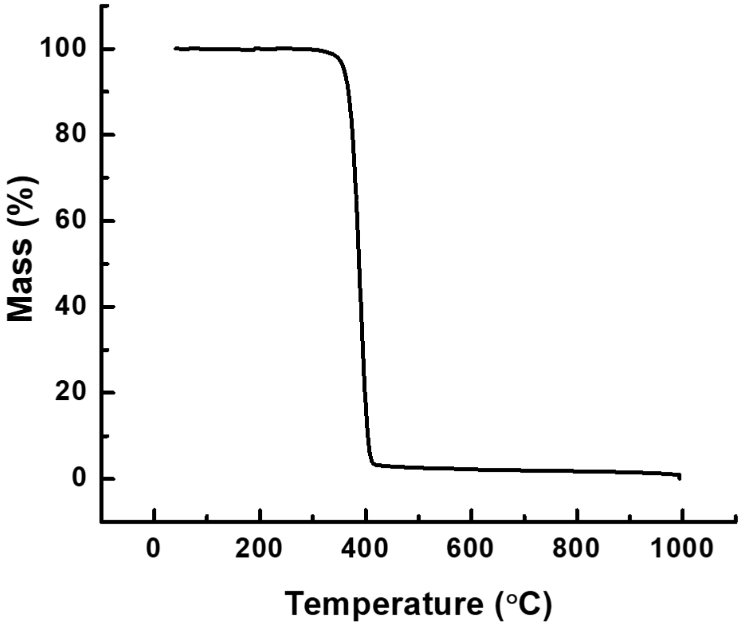

Figure 5.2.2.1: Mass loss profile of PEO binder

5.2.3 Relationship Between Printing Parameters and Density

The following parameters were determined: binder concentration, green density, sintered density, and compressive strength. The parameters were finalized as those which result in the highest sintered density of the sample. As mentioned before, there are 4 main parameters that were adjusted to control the lab-made inkjet 3D printer used in this study. After finding the best settings for the roller and shaker, the layer height and nozzle temperature (which relate to ink and powder bed interaction) were varied to find the highest green density. All parameters varied for each powder composition and preparation method as was expected. Optimized roller and shaker settings were 70% and 50% for NG powders and 70% and 35% for MC powders.

Figure 5.2.3.1(a) shows the effect of the layer height on the relative bulk density of the alumina cube before and after sintering at 1700 ºC for 10 hours and 48 hours. The nozzle temperature was set to 60 ºC. The decrease of layer height from 200 μm to 100 μm, increased the green density of the alumina cube which resulted in an increase of the relative sintered bulk density (Figure 5.2.3.1(a)). The increasing the holding time from 10hrs to 48hrs at the sintering temperature of 1700 ºC did not affect the final bulk density much, showing only ~ 0.6 % increase of the relative density, indicating that the pore structure was stable under these conditions. The average bulk density and compressive strength of the sintered cube, with a layer height of 100 µm (NG2) and 150 µm (NG3), were 52.9 % /78.3 MPa and 44.9% / 67.2 MPa, respectively, as shown in Table 5.2.3.1. The powder bed made with the smaller layer height could be saturated or oversaturated by the water-based ink, resulting in an increase of the green density by connecting the granules made up of nano powder to each other. Conversely, the granules made with the higher layer height were not well connected, resulting in a reduction of green strength and density which affect the final bulk density and strength.

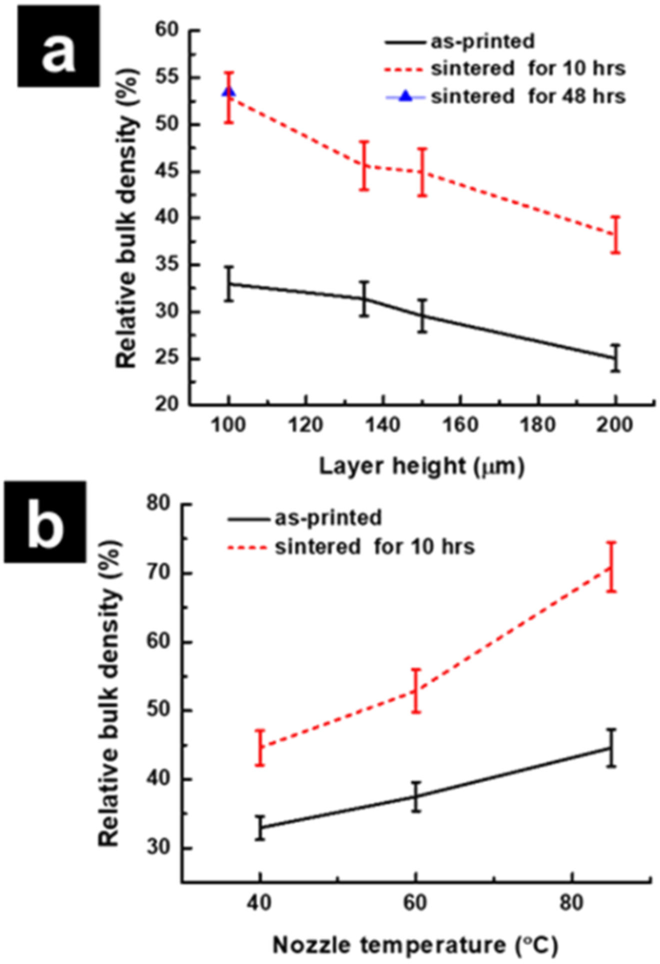

Figure 5.2.3.1: Optimization of 3D printing parameters for nano-alumina granules containing the binder (NG): (a) effect of layer height on relative bulk density of alumina cubes before and after sintering at 1700 ºC for 10 hrs and 48 hrs. (b) Effect of nozzle temperature.

Table 5.2.3.1: Effect of printing parameters on sintered bulk density and compressive strength.

Sample Name	Layer height	Nozzle temperature	Green bulk density	Holding time @1700°C	Sintered bulk density	Compressive strength
	μm	°C	%	hours	%	MPa
NG1	100	85 ± 2	44.6	10	70.9	113.1
NG2	100	60 ± 2	33.0	10	52.9	78.3
NG3	150	60 ± 2	29.6	10	44.9	67.2
MC1	250	60 ± 2	39.5	10	43.6	20.3
NG1Hold	100	85 ± 2	45.2	48	71.1	26.0
NG2Hold	100	60 ± 2	34.1	48	53.2	13.9
NG3Hold	150	60 ± 2	29.0	48	45.5	4.7
Scaffold	100	85 ± 2	-	10	50.8	30.2

Figure 5.2.3.1 (b) shows the effect of the nozzle temperature on the relative bulk density of alumina cubes before and after sintering at 1700 ºC for 10 hrs. With increased nozzle temperature, the green bulk density of the 3D printed parts increased, which made the final relative bulk density of the sintered parts increase. This phenomenon of high compaction in green state leading to high sintered density is well known in literature [118]. The average bulk density and compressive strength of the sintered cubes with nozzle temperatures of 60 ºC (NG2) and 85 ºC (NG1) were 52.9 % /78.3 MPa and 70.9 % / 113.1 MPa, respectively, as shown in Table 5.2.3.1. Since all other printing conditions were kept constant, the effect of the nozzle temperature is clear. With higher nozzle temperature, more "ink" was spread on the powder bed resulting in a decrease of porosity by removing intra agglomerate pores.

5.2.4 Relationship Between Sintering Holding Time and Compressive Strength

Regardless of the printing conditions, the matrix structures composed of NG powder resulted in higher densities than the MC powder under the same sintering conditions (1700 ºC for 10 hrs). Figure 5.2.4.1 shows the microstructure of the sintered alumina cubes made under NG1, NG2 and NG3 conditions. Since nano powders offer high sinterability, the intra-agglomerate pores between granules were mostly removed. This result indicates that inter-agglomerated pores or open porosity are the main part of the bulk porosity of the cube. The smaller pore size and nano-sized alumina particles inside of NG powder make the struts highly dense. Also, a small average grain size of <10µm was observed as shown in Figure 5.2.4.1.

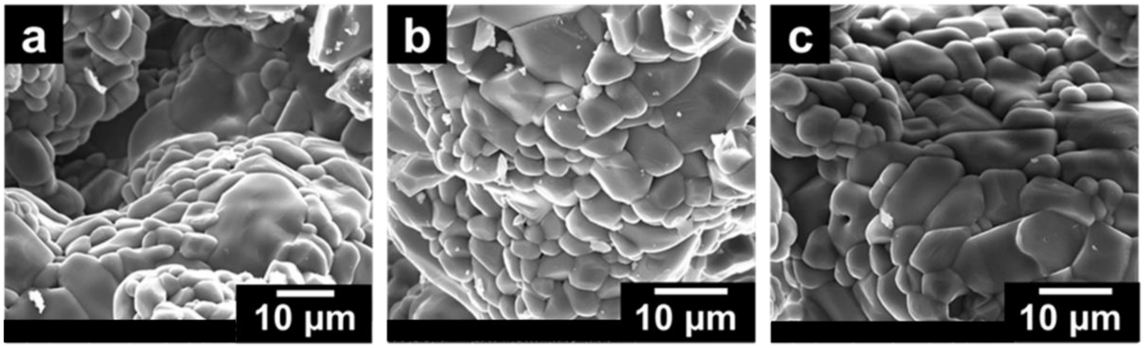

Figure 5.2.4.1: SEM images of sintered alumina cubes made of nano-alumina granules containing binder, from left to right: NG 1, NG2, and NG3 condition.

From Table 5.2.3.1, the effect of longer dwell (holding) time during sintering on the mechanical strength of the samples is clear. Longer holding time leads to a decrease in compressive strength. Prior to this observation, the holding time was increased in an effort to increase the final sintered density, however, the additional hours in the furnace did not affect the density significantly as seen in the results. The mechanical properties, however, were greatly affected. To study this further, two sets of samples were compared; NG1 was compared to NG1Hold, NG2 to NG2Hold and NG3 to NG3Hold. The “Hold” indicates that the sample was held at the maximum temperature (1700 ºC) for 48 hours rather than 10 hours. A dramatic drop in mechanical strength is observed between normal and long holding times. For example, the compressive strength of NG2 and NG2Hold were 78.3MPa and 13.9 MPa, respectively.

Finally, the NG1 condition was chosen for scaffold fabrication due to high strength and reasonable open porosity. The average apparent solid strut density of NG1 was ~96.9 % measured following the Archimedes method, indicating an average closed porosity of 3.1 %. Therefore, since the average bulk porosity is 29.1 %, the calculated open porosity is 26.1 % (= 29.1 % bulk porosity - 3.1 % closed porosity). Since a bone scaffold requires > 50 % open porosity, designed pore channels with > ~30 % porosity were incorporated in the scaffold design.

5.2.5 Microstructural Evolution from Printed to Sintered

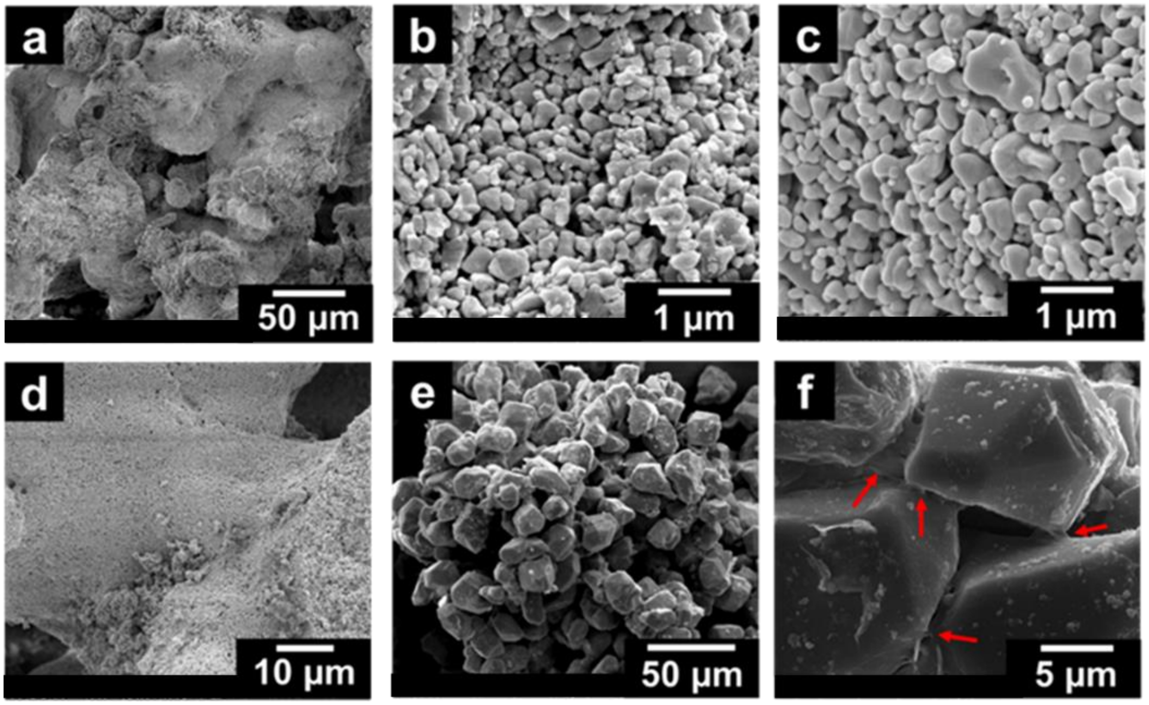

Figure 5.2.5.1: SEM images (a), (b) green parts using nano-alumina granules (c), (d) debinded parts using nano-alumina granules and €, (f) green parts using micron-alumina powders coated with the binder MC. All images are for the cube geometry. The red arrows indicate the slight bridges formed by the binder.

For the fabrication of load-bearing bone scaffold, the SJG method has many advantages related to microstructure over the SJC method. This is clear when analyzing each step of the process from printing to sintering and the evolution of the microstructure of the 3D printed parts. Sem was used to analyze components made from SJG and SJC. Particularly, the comparison between the parts made using the NG1 and MC1 conditions in Table 5.2.3.1 is described here.

The 3D printed parts produced by the SJG method show large macropores and well-connected granules with wide bridges (Figure 5.2.5.1(a)). The size of these bridges is important because they become the inter-particle necks which affect the strength of the final parts. The alumina particles and PEO binder inside of granules were well-packed with a small pore size less than that of the alumina particle size, as shown in Figure 5.2.5.1 (b). Figure 5.2.5.1(c) and (d) shows the alumina particles inside a granule and bridge after sintering at 1200ºC for 3hrs for the 3D printed parts by the SJG method. The alumina grain size inside the agglomerates (Figure 5.2.5.1 (c)) increased slightly compared to that of the green part (Figure 5.2.5.1 (b)).

The 3D printed parts made from SJC showed a weak connection by coated binder between the micron-sized alumina particles as indicated by Figure 5.2.5.1 (e) and (f). The red arrows in Figure 5.2.5.1(f) indicate the PEO binder between the alumina particles in the printed MC parts. The relative bulk green densities of the NG1 and MC1 samples were 44.6% and 39.53%, respectively. Since tapped density of the NG sample was 37.4 %, solvent jetting during 3D printing increased the green density even higher than the tap density of NG Powders. For the NG method, the water-based ink can be absorbed into the granules and reduce the size and numbers of mostly inter-agglomerate pores. For the MC, the ink activates the binder that is coating the particles and connects the micron-alumina particles to each other, however, given the size of the particles, the binder does not fill in as it does for the NG powders, limiting compaction density in the green printed state.

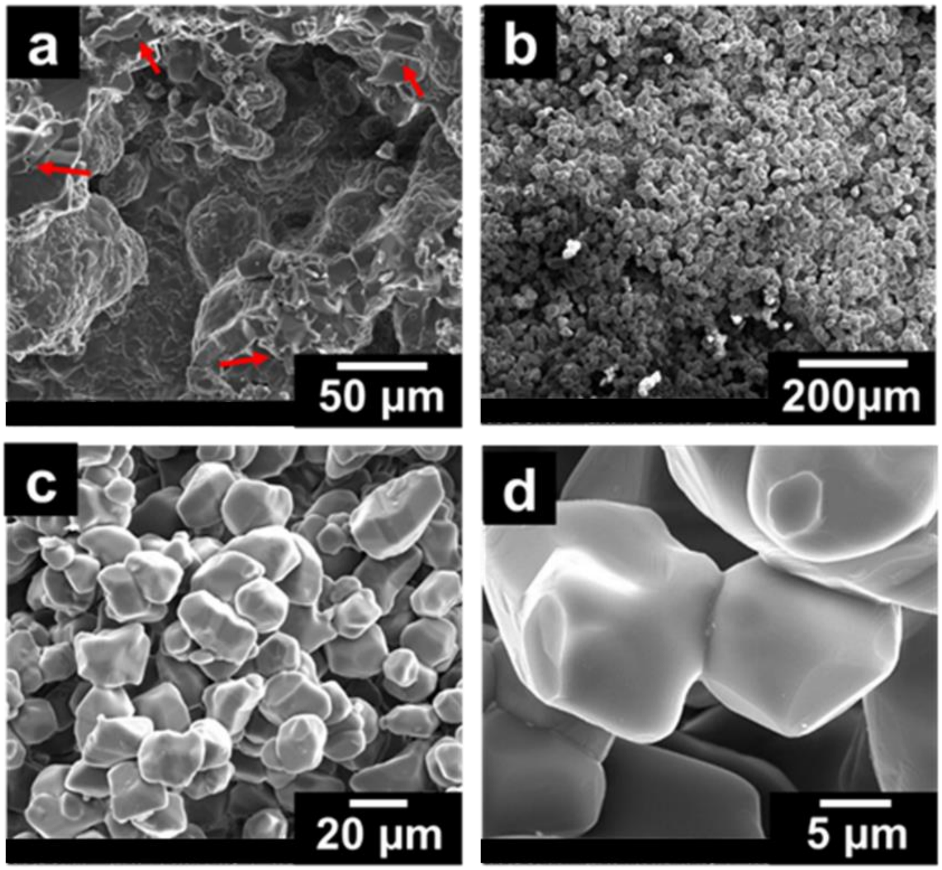

Figure 5.2.5.2: SEM images of sintered cube-shaped parts using (a) nano-alumina granules containing the binder NG1 and (b) – (d) micron-alumina powders coated with the binder MC. The red arrows indicate the micropores.

The microstructures of the sintered cube-shaped alumina parts produced under NG1 and MC1 conditions were measured using SEM after heating at 1700ºC for 10hrs and 24hrs respectively. During heating, the PEO was burned off and released to the air through the open porous structure. However, the porous structure maintained sufficient strength to maintain its structure. This could possibly be due to some mechanical interlocking of the irregular alumina particles and some neck formation during printing [149]. The average sintered bulk densities of alumina parts made from NG and MC were 70.9% and 43.6%, respectively. The average bulk shrinkages of the sintered alumina parts made from NG and MC were 26.3 % and 4.1 %, respectively. The alumina parts made from NG showed large size intrinsic macropores (~>100 µm) and large necks (~> 50 µm) (Figure 5.2.5.2(a)). The apparent strut density of sintered parts with NG was high (96.9 %), which indicates that the matrix was densified well even though macropores were still present. As shown in Figure 5.2.5.2 (a), only a small portion of micropores, which are indicated by the red arrows, were observed inside of the matrix. The alumina parts made from MC showed smaller sized macropores (~ < 30 µm) as shown in (Figure 5.2.5.2 (b) and (c)). Also, since sintered parts from micron-sized powder showed only small amounts of densification due to large particle size, the neck size was ~ < 20 µm (Figure Figure 5.2.5.2(d)), which is much smaller than that of the NG parts (Figure 5.2.5.2(a)). The average grain sizes of the parts made from NG and MC were 10.6µm (Figure 5.2.4.1(a)) and 23.5 µm (Figure 5.2.5.2(c) and (d)), respectively. The combination of higher sintered bulk density, wider neck, and smaller grain size causes the compressive strength (113.1 MPa) to be higher for the alumina parts made by NG compared to the compressive strength (20.3 MPa) of the ones made from MC.

5.2.6 Biomimetic Scaffold Characterization

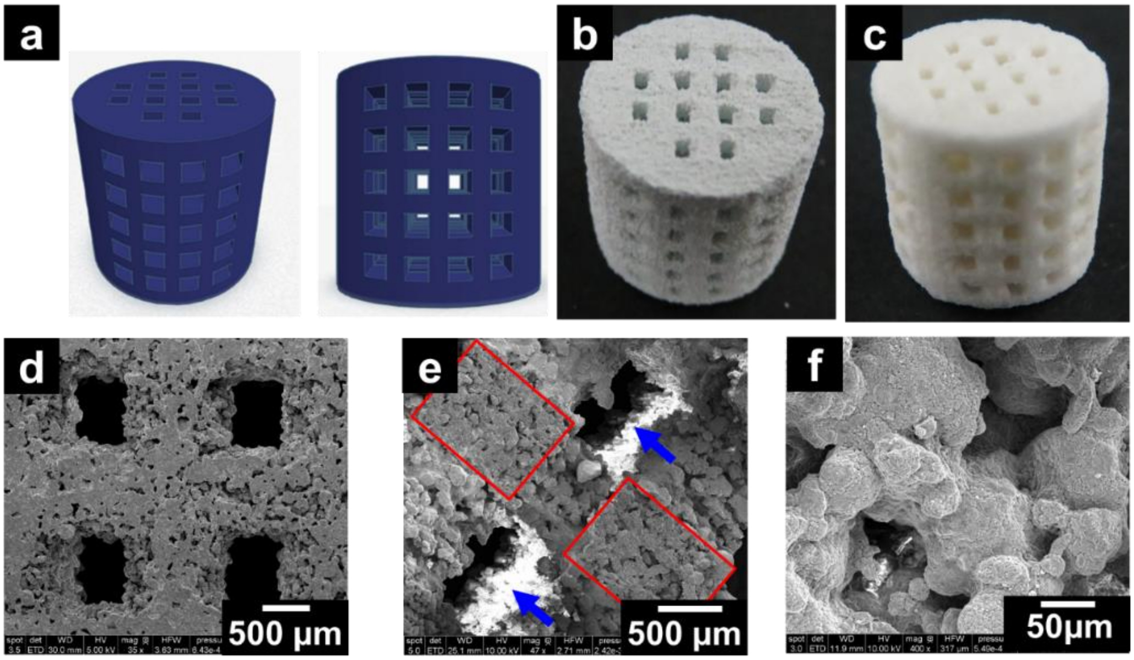

Figure 5.2.6.1: (a) CAD image of scaffold. 3D printed scaffold made by solvent jetting on granulated feedstock containing binder (SJG) method (b) before sintering, (c) after sintering. SEM image of sintered 3D printed scaffold made by the SJG method, (d) outer surface, (e) struts inside of scaffold structure and (f) interconnected porosity.

With the best intrinsic porosity condition (NG1 in Table 5.2.3.1), the bone scaffolds were fabricated with the designed channels using the SJG method. Figure 5.2.6.1(a) shows the CAD model of the cylindrical samples. The cylindrical CAD model has a diameter of 10 mm and a height of 10 mm with the designed channel size of 1 mm x 1 mm. The volume of the designed channel network in CAD is 38.6 % of the total cylinder volume. This CAD model was scaled up by 120 % to account for the shrinkage that occurs during the 3D printing and sintering. Figure 5.2.6.1(b) and (c) show the alumina scaffold green specimen after 3D printing and final specimen after sintering respectively. The sintered bulk density, apparent porosity, and apparent solid density of alumina scaffold were 50.7 %, 47.9 % and 97.3 % respectively.

As shown in Figure 5.2.6.1(d), the designed channel showed the shorter edge length in the x-direction (x: 550.4 µm, y: 828.1 µm and z: 891.5 µm) which will be discussed in the next section. More importantly, the designed channels have sufficient size for cell penetration into the scaffold. Figure 5.2.6.1(e) shows the inside microstructure of the broken scaffold after the compressive strength test. The red boxes and blue arrows indicate the fractured surface of the struts and the designed pore channel respectively. As shown in Figure 5.2.6.1(f), the size of the interconnected intrinsic pores is similar to the previous optimization study (NG1 condition, Figure 5.2.5.2(a)) and is large enough for cell migration and nutrient transfer (~> 100µm). The average neck and grain size is 63.5 µm and 11.3 µm which is similar to the NG1 condition. Due to the introduction of the designed channels, the average compressive strength of the alumina scaffold (30.2MPa) was reduced compared to that of the cube-shaped sintered alumina (113.1MPa).

In conclusion, bone scaffolds which contain macropores (>100 µm, formed by inter-agglomerate pores during 3D printing) and designed pores/macro-channels (>550 µm, created by CAD modeling) with sufficient mechanical strength and porosity were fabricated using a time and cost-efficient inkjet printer and printing methods.

5.2.7 Sintering Model and Finite Element Simulation

The developed powder preparation technique increased the density of the printed samples significantly. However, the lowest porosity achieved was 29% which is not near full density. Although full density is not a requirement for bone scaffold prototypes, it is beneficial to achieve higher densities to mimic compact bone. The powder preparation and printing parameters were optimized; therefore, the sintering cycle is the only variable available to change. Instead of doing hundreds of experiments, the continuum theory of sintering (equation 2) can be used to analytically determine whether achieving full density is realistic. As mentioned in section 4.2.2

It is beneficial to understand and predict the final density of the printed bone scaffolds when attempting to mimic the properties of bone. This is because the porosity of bone differs so greatly at different parts of the body and even within the same bone fragment. For example, the compact bone part of the femur can reach a porosity level of less than 5%, whereas the cancellous portion of the femur can reach a porosity level of 99% in the most porous areas.

As part of this work, a finite element model (FEM) simulation was developed to predict the evolution of porosity and final density of the components after sintering. The continuum theory of sintering was employed in the same way as in Chapter 3 and embedded in a FE code. Similar simplifications were made as in the previous section for the free sintering (pressure-less) conditions of the proposed method. Furthermore, the dilatometry data performed for the previous analysis was used in this model to determine the sintering parameters necessary for the properties of the material used. More importantly, this model can be used to predict a final density utilizing the printed density as the initial density parameter.

5.3 Discussion

5.3.1 Effect of Powder Preparation and Printing Parameters

When the nozzle temperature was increased in the SJG method, there was an abrupt increase of the sintered bulk density as shown in Figure 5.2.3.1(b) and Table 5.2.3.1. The increased amount of ink released by raising nozzle temperature, in turn, increased the green bulk density. When the NG1 and NG 2 results in Table 5.2.3.1were compared, raising the amount of ink increases the green density of alumina parts slightly (10 % shrinkage) but, the sintered density of NG1 more rapidly increased (31.7 % shrinkage) compared to NG2 (7.6 % shrinkage). This result was related to the geometrical arrangement of particles inside of the powder bed.

The geometric arrangement of the particles before sintering affects many crucial factors including: the green density, pore size distribution (PSD) and coordination number which control the final density and properties of the sintered part. When the pore size is too large (larger than half the particle size), they are not easy to remove though sintering. This means the green part with broad PSD, due to agglomerates or poor green part preparation, will have low sinterability since large pores tend to grow while small pores shrink, resulting in large unremovable pores in the final sintered structure.

However, for the fabrication of a porous structure with intended macropores (~ > 100 μm), the granules with wide size distribution were helpful in combination with the SJG method. In the current study, the granules with wide size distribution (<250 μm, limited by sieve) made of nano alumina particles (~ 200 nm) and PEO binder were used. Generally, wide particle size distribution generates wide PSD, which will have low sinterability [118]. In this study, this low sinterability problem was solved using the SJ method. The SJ method can control the macroporosity by controlling 3D printing parameters such as layer height and spread ink amount. During ink jetting in the SJ method, the size and amount of inter-agglomerate pores were reduced as shown in Figure 5.1.3.1. The larger macropores (~ >100μm) may see only limited reduction using ink-jetting since they are too large to be removed by the ink directly. On the contrary, the number of small micro and macropores (~ <100μm) were reduced or removed as the ink was applied. This could transform a wide PSD into more of a bimodal (macropore >100 μm and micropore ~ 100 nm inside of granule) PSD structure. During sintering, the inter-agglomerate pores produced by 3D printing grow while the intra-agglomerate pores inside of the agglomerates shrink. Therefore, the sinterability of the green part is increased compared to that with a wide PSD. Regarding the abrupt increase in sintered density by increasing nozzle temperature from 60 ºC to 85ºC situation shown above, the size and shape of some macropores were changed enough to become unstable which made them ready to shrink. As a result, a large macropore (>100μm) structure with high strut density was obtained after sintering when a high nozzle temperature was used.

Most P-3DP methods use micron-sized powder to achieve high flowability during the 3D printing process. The high flowability ensures a high powder packing density (or green density of printed sample), which usually generates high sintered bulk density parts. However, to make an intrinsic porous structure with large macro-porosity, the SJG method has clear advantages in terms of the controllability of macropores compared to other P-3DP methods. For example, our results showed that the cube-shaped part made by micron-sized alumina particles by the SJC method has low sintered bulk density (43.6 %), narrow neck size (~ < 20 μm), small macropore size (~ < 30 μm), and low strength (20.3 MPa). Whereas the SJG method yielded a cube-shaped part that has high sintered density (70.9 %), wide neck size (~ > 50 μm), big macropore size (~ > 100 μm) and high strength (113.1 MPa).

With micron-sized powders, the powder characteristics, such as, particle size and particle size distribution could be controlled to obtain a macroporous structure (> 100 μm) in SJ (this requires a lot of effort) but, achieving high strength is not easy with micron-sized particles due to their low sinterability. Conversely, the SJG method has more freedom to vary the macroporosity. After making a powder bed with wide PSD using granules, relatively simple control of the nozzle temperature and layer height can determine the pore structure as shown in Figure 5.2.5.2 (a) and Table 5.2.3.1. Also, large necks can be formed by the SJG method, which increases the compressive strength of a porous structure (Figure 5.2.5.1 (a) and Table 5.2.3.1). To the contrary, micron-sized powders, which have low sinterability compared to nanopowders, have a smaller neck size since the evolution of the neck area is only dependent on sintering conditions.

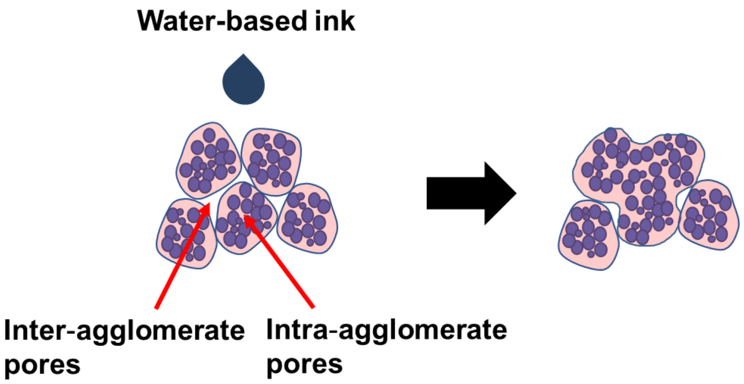

Figure 5.3.1.1: Schematic of the densification mechanism by solvent jetting on granulated feedstock containing binder (SJG).

There was densification (shrinkage) of 3D printed parts caused by water penetration during water-based ink jetting (see Figure 5.3.1.1). Therefore, the dimension of the printed part was smaller than that of the CAD model, which could be seen as a setback of this method. However, this shrinkage is very repeatable and can be accounted for by scaling the CAD file after a few trials of 3D printing. Contrary to other powder-based printing methods, the SJG method can change the powder packing density since the feedstock adsorbs the water-based ink and gains plasticity during the 3D printing stage as shown in Figure 5.3.1.1. The deformation of the feedstock decreases the amount and size of macro and micropores between and within the agglomerates, resulting in an increase of the green density of the printed parts. Also, the water-based ink absorbed by granules creates a bridge between the granules; the width of the bridge depends on the amount of ink. On the other hand, general binder jetting via powder bed method spreads polymer-based ink between micron-sized particles, and the binder penetrates the gaps between the particles, bonding only itself, not reacting or affecting the powder bed particle interaction.

The lab-made inkjet 3D printer spreads the ink moving in the X direction (fast printing axis). The acceleration effect in the X direction seems to make the ink spread out in that direction more than expected. The x and y dimensions of the printed green scaffold were 1.53 % and 3.64 % smaller than the corresponding dimensions of the CAD model, which indicates that the cartridge spread the ink more in the x-direction than in the y-direction. The faster printing in one of the directions also affected the channel size of the green sample of the alumina scaffold. The original square shape of the designed channel in CAD was changed to the rectangular shape with shrinkage of x: 30.52 % and y: 8.87 % after printing. Since the nozzle spread the ink more than expected, it resulted in a shorter edge of the channel in the x-direction.

The sintered bulk density of the optimized cube-shaped part was 70.9 %. When including the designed pore channels which occupied 30.8 % of the component volume in the CAD model, the sintered bulk density of the scaffold was expected to be 40.1 % (=70.9 % - 30.8 %). However, it was 50.8 %. This was mostly attributed to the anisotropic structure build-up during the 3D printing stage explained above.

5.3.2 Effect of sintering dwell time

It was observed that the mechanical properties of the sintered samples drastically deteriorated with longer sintering holding times. After analyzing the microstructure in the SEM, it can be seen that the grain size more than doubled for the samples held for 48 hours compared to the samples held for 10 hours. An increase in grain size leads to a decrease in mechanical properties. This is a well-known effect known as the Hall Petch effect [189]. The Hall–Petch relation predicts that as the grain size decreases the yield strength increases. The Hall–Petch relation was experimentally found to be an effective model for materials with grain sizes ranging from 1 millimeter to 1 micrometer and therefore, is appropriate to conclude that this difference in grain growth is responsible for the difference in compressive strength.

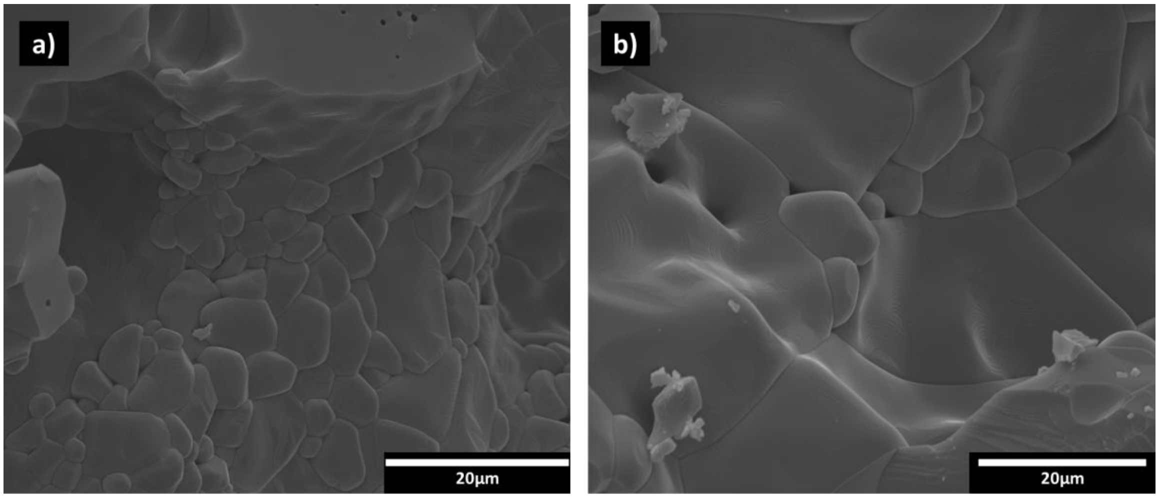

Figure 5.3.2.1: SEM images showing grain size differences between samples held for (a)10 hours and (b)48 hours during sintering.

When considering the real-life application of this manufacturing method for bone scaffolds, it is important to consider the overall time required to fabricate a sample. Shorter time frames are preferred and therefore the shorter lengths of holding times are also beneficial from an implementation perspective not just from a strengthening perspective. Additionally, as was discussed in section 4.2 and also shown in Figure 4.2.1.1, adding more dwell time does not significantly increase the final density, therefore, this should not be considered as a technique for increasing the sintered density.

5.3.3 Sintering Simulation

Using the continuum theory of sintering model described above was successfully embedded into COMSOL finite element modelling software. A combination of dilatometry and experimental results were used to calibrate the existing free sintering model to the materials used in this study. This model was evaluated by confirming the final density of all samples were accurately predicted. Table 5.3.3.1 lists the comparison between experimental and model results for each cubic sample.

Table 5.3.3.1. Comparison between experimental data and FE sintering model

Sample	Sintered Relative Density	
	Experimental	Model
NG1	70.9	71.0
NG2	52.9	54.0
NG3	44.9	46.0

This predictive tool allows us to plan the sintering cycle, to include the hold (dwell time), via the simulation rather than the highly time intensive physical experiments. As discussed, the slight difference in the scaffold actual density and what was expected is due to the anisotropy of printing which is not considered in this model. This anisotropy can be taken into account in the initial CAD model before printing since the distortion of the channels does not happen during sintering.

5.4 Chapter Summary

The cost and time-efficient fabrication of hierarchical porous structures for load-bearing applications was investigated. The powder processing methods of the nano and micron-sized alumina powders were described for the solvent jetting powder bed 3D printing method (P-3DP). The higher nozzle temperature (more ink spread) and lower layer height in this 3D printing process increased the green density, sintered density and compressive strength under the considered experimental conditions. Also, the advantages of using nanopowder granules over micron-sized particles for solvent jetting were thoroughly described and discussed. Optimizing intrinsic porosity by controlling the 3D printing parameters, allowed the hierarchical pore structure in a ceramic scaffold with cell path/interconnected macro channels with an overall high compressive strength, can be fabricated easily by solvent jetting on granulated feedstock containing binder (SJG) method.

The solvent jetting on granulated feedstock containing binder (SJG) method can control the porosity via control of 3D printing parameters by deforming and connecting the granules, which is quite unique compared to other 3D printing methods. The working principle studied here can be applied to the fabrication of hierarchical porous structures using various materials including hydroxyapatite, tricalcium phosphate and composites.

In addition, a theoretical model of sintering was developed for the printed material. This tool gives model-based predictions on the sintering time needed to achieve a certain porosity. The ability to choose the final porosity of a scaffold is an important advantage that could make this method of producing scaffolds much more useful and superior to other scaffold making techniques. The model was verified by comparing the predicted porosity based on the sintering holding time with experimental achieved porosity. Furthermore, the model was embedded into a finite element software and used to predict the final density which is important for the practical application of this technology.

The powder preparation technique developed here allowed for the printing of nano-powders which aided in increasing the sinterability and compressive strength of printed components, however, a high density was not attained. Only free sintering was used in this chapter, the next chapter will be dedicated to the addition of pressure prior to sintering as a way to increase the final sintered density.

Chapter Acknowledgements

Chapter 5, in part, was published as it may appear in Rapid Prototyping Journal, 2021, Lee, Geuntak; Carrillo, Maricruz., Elsevier. The dissertation author was the primary researcher and co-author of this paper.

6 INDIRECT ADDITIVE MANUFACTURING OF BIOCERAMIC PROTOTYPES VIA SUBTRACTIVE SINTERING

The previous chapter described our attempt to create a predictably porous scaffold that could mimic the properties of a real bone. Although we achieved this to a certain extent, there is still a gap for the production of near-full density components. The theoretical analysis conducted predicted that free sintering was not sufficient for the consolidation of the printed samples in a realistic amount of time. One way to increase density is by the application of pressure. However, the application of pressure is traditionally limited to simple shapes. The main benefit of additive manufacturing (AM) is the ability to produce complex geometries, therefore, this advantage should not be compromised.

One technique that leverages AM’s ability to print complex geometries while still using pressure is Indirect Additive Manufacturing (I-AM). This technique entails 3D printing a mold and using that mold in conjunction with other (more traditional) manufacturing techniques to create a final component that resembles the geometry of the mold. For example, Manière et al. successfully fabricated net shape parts with high density using this approach via spark plasma sintering (SPS) and polymer printing [190]. Although the results were impressive, the ability to use pressure in conjunction with free sintering needed to be investigated due to the low energy required in free sintering when compared to SPS. Indirect Additive Manufacturing Casting is a lengthy process that works in a similar way to traditional Investment Casting [191] where a polymer scaffold, produced via FDM, is casted with a high temperature material (usually a high temperature ceramic), the polymer is then burned out leaving only the ceramic cast. This cast is then used as a sacrificial mold to obtain a sample composed of a second material, usually molten metal [192], [193]. This approach has some defect formation issues but in general is successful producing metal parts. However, it cannot be used to make ceramic parts.

When 3D printing ceramics and metals, sintering is usually necessary after printing to achieve higher densities in the printed part. Naturally, the possibility of using this post-processing step to fabricate complex shapes has been explored. Selective Inhibition Sintering (SIS), as the name suggests, is usually described as using sintering inhibitors to sinter only certain parts of the sample. This concept has been used along with powder-based printing of metals by depositing sintering inhibitors from the “ink” cartridge [194]. For ceramics, liquid inhibitors delivered by inkjet printing are not effective due to the high sintering temperature of ceramics [195]. This method can produce complex shaped parts but with low final sintered density.

In this work, a novel Indirect AM process called Additive Manufactured Subtractive Sintering (AM-SS) is created. This method uses Subtractive Sintering (SS) in conjunction with the powder-based 3D printing technique Solvent Jetting (SJ) to print the sacrificial mold and later destroy it during sintering. AM-SS alleviates the limitations faced by the additive manufacturing techniques described above and issues faced when traditional methods are used for producing high density, complex shaped parts from ceramics.

6.1 Materials and Methods

Solvent jetting was used to print the sacrificial mold, followed by Cold Isostatic Pressing (CIP) and subtractive sintering to produce high density ceramic or metal complex parts needing only free sintering. In AM-SS, instead of printing inhibitors, polymers or expensive molds, a sacrificial mold is printed using a unique material combination that swells and breaks during sintering.

First, the sacrificial mold is printed using the custom printer (Ultimaker 2+ with ColorPod modification [104]) described in Chapter 3 from a powder mixture comprised of maltodextrin (MD) (Pure Organic brand), sugar (Wholesome brand, powdered) and alumina powder (-100, +325 mesh, 99.2% pure, Materion, USA). This mixture was found to swell and crack after reaching a specific temperature. Second, the inner face of the mold base is sprayed with graphite spray (Blaster) to help with removal and then filled with the article powder (in our case, Zirconia Z-pex Smile powder from Tosoh, Inc., Japan or Hydroxyapatite from PlasmaBiotal). The mold cover is carefully placed as the mold base is slightly tapped to ensure the powder is surrounding any features present in the mold cover. Third, using the standard sample preparation for Cold Isostatic Pressing (CIP) (CP360, American Isostatic Press), the full assembly is subject to 300-400 MPa pressure to increase the density of both the mold and the article particle before sintering. Fourth, the CIPed sample is placed in a tube furnace (GSL 1700X, MTI) for sintering. As the sample sinters, the sacrificial mold swells and cracks while the article powders sinter and shrink. Finally, the debris from the mold is removed with a brush and the final sintered sample is attained. The overall process is illustrated in Figure 6.1.1 below.

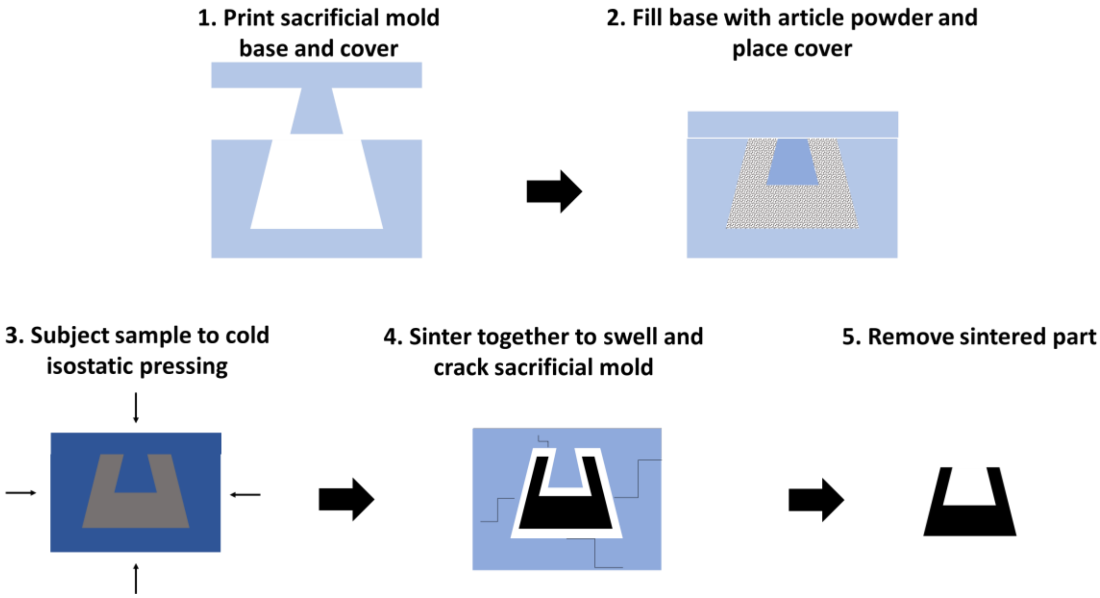

Figure 6.1.1: Schematic of the process of fabricating fully sintered 3D printed parts via AMSS.

6.1.1 Powder Processing

The powder used for printing the sacrificial mold to be subtracted during sintering was prepared by mixing alumina (-100, +325 mesh, Materion, USA) or zirconia (TZ-PX-392, Tosoh, Inc., Japan), maltodextrin (Pure Organic brand) and sugar (Wholesome brand, powdered) powders in a conventional dry mixer (Turbula, GreenMills) for 60 minutes. Alumina and zirconia powders were chosen based on their high sintering temperatures and the availability of the powder in large particle size. In the previous study of the printing parameters, an interesting phenomenon was observed. All printed cubes were subject to sintering yet, did not densify at all. In an effort to increase the density of the green specimens, the green bodies were subject to CIP and then sintered. The cubic samples swelled up and broke during the sintering. This “negative” effect was used in this process to our advantage. The chosen mixture included 74 wt% alumina or zirconia, 13 wt% maltodextrin and 13 wt% sugar. Example: in 100 g of powder mixture, 74 g were alumina or zirconia, 13 g were sugar and 13 g were maltodextrin. In this mixture, the sugar and maltodextrin serve as the binders for printing. In the present work, 3 mol% yttria-stabilized nano-zirconia powder (Z-pex Smile, Tosoh, Inc., Japan) and Hydroxyapatite (Captal R, Plasma Biotal, United Kingdom) were used as the article powders, no further processing was necessary. In fact, this is one of the advantages of this method, the ability to use the article powder in its pure form.

6.1.2 Experimental Procedure

The same custom-made printer described in chapter 3 was used for the printing of sacrificial molds. For this investigation, the following three geometries were printed: cylinder, dental crown, and simple gear. The cylinder was printed multiple times to understand the deformation that happens during the isostatic pressing. The dental crown demonstrated the ability to produce complex shapes and the gear showed that internal channels were possible to some extent. Figure 6.1.2.1 shows the desired design and the sacrificial mold design for each geometry.

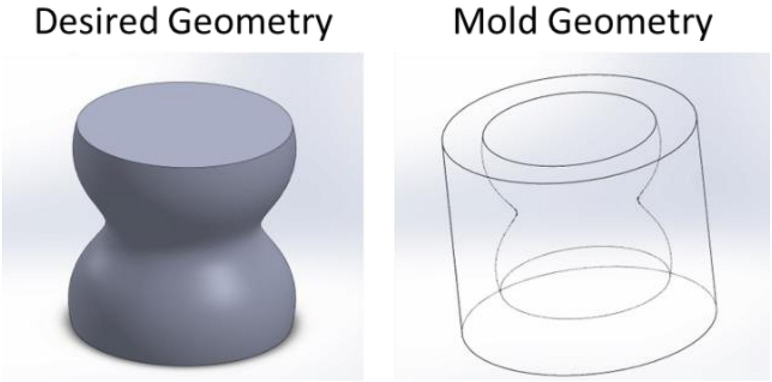

Figure 6.1.2.1: Mold geometry based on the final desired component.

After pressing, the sacrificial mold filled with compressed powder was subjected to sintering. Sintering was conducted using a conventional tube furnace in the air (GSL-1700X-KS-UL-60, MTI, Richmond, CA). The heating cycle used for Zpex smile was: 20 ºC – 200 ºC with 5 ºC/min, holding at 200 ºC for 20 min, 200 ºC to 300 ºC with 10 ºC/min, holding at 300 ºC for 60 min, 300ºC – 600ºC with 5ºC/min, and holding at 600 ºC for 20 min, 600 ºC -1400 ºC with 5 ºC/min, 1400 ºC to 1300 ºC at a rate of 5 ºC, holding for 10 hours and cooled down at a rate of 5 ºC/min. The sintering cycle described above was taken from the work of Manière et al. conducted on the Zpex Smile material system [190]. The heating cycle used for Hydroxyapatite (HAP) was: 20 ºC – 200 ºC with 5 ºC/min, holding at 200 ºC for 20 min, 200 ºC to 300 ºC with 10 ºC/min, holding at 300 ºC for 60 min, 300ºC – 600ºC with 5ºC/min, and holding at 600 ºC for 20 min, 600 ºC -1200 ºC with 5 ºC/min, holding for 4 hours and cooled down to room temperature at a rate of 5 ºC/min.

6.1.3 Characterization

The bulk relative densities of the sintered samples were estimated using the Archimedes' immersion method following ASTM standard C373-18. The size of the powder and of the sintered specimen's grains were analyzed using a scanning electron microscopy (SEM), (FEI Quanta 450, USA). Additionally, the printed parts were analyzed using SEM to observe the particle interaction after printing, eventually leading to understanding the sintering inhibition and swelling process.

To understand the deformation that happens during the developed AMSS process, the dimensions and distortion of the final geometry were measured using a caliber and a Coordinate Measurement Machine (CMM, Crysta-Plus M443, Mitutoyo Co.) when necessary.

The general height and diameter of the cylindrical samples were measured with a caliber but when there was more complex deformation, the CMM was used. Specifically, on the cylindrical samples, the top and bottom was measured using a single point and the side walls were measured using a circular pattern with fixed z coordinates.

6.2 Experimental Results

6.2.1 Powder characterization

SEM images of all powders are seen in Figure 6.2.1.1. The average particle size for the alumina and zirconia sacrificial mold powders chosen is 110 µm and 45 µm, respectively. Micron sized powder was chosen for the sacrificial mixture because a larger particle size makes sintering more difficult, especially in ceramics, which is desirable for the sacrificial mold. Maltodextrin and sugar powders are also micron size with an average particle size of 40 and 90 µm, respectively.

The ZPex smile and Hydroxyapatite (HAP) SEM images are seen in Figure 6.2.1.1. Zirconia powder has a particle size range from 10-100 µm, rounded and is specially made for dental applications. This powder was chosen to demonstrate the versatility of the developed method given that ceramics, in general, are difficult to fully sinter using powder-based printing. The HAP powder chosen has a smaller particle size (average of 3 µm) which means it is more sinterable than the mold. It is not very uniform or spherical in shape but was chosen because of its sinterability. HAP is also the mineral that makes up bones, therefore, of great interest for bone repair.

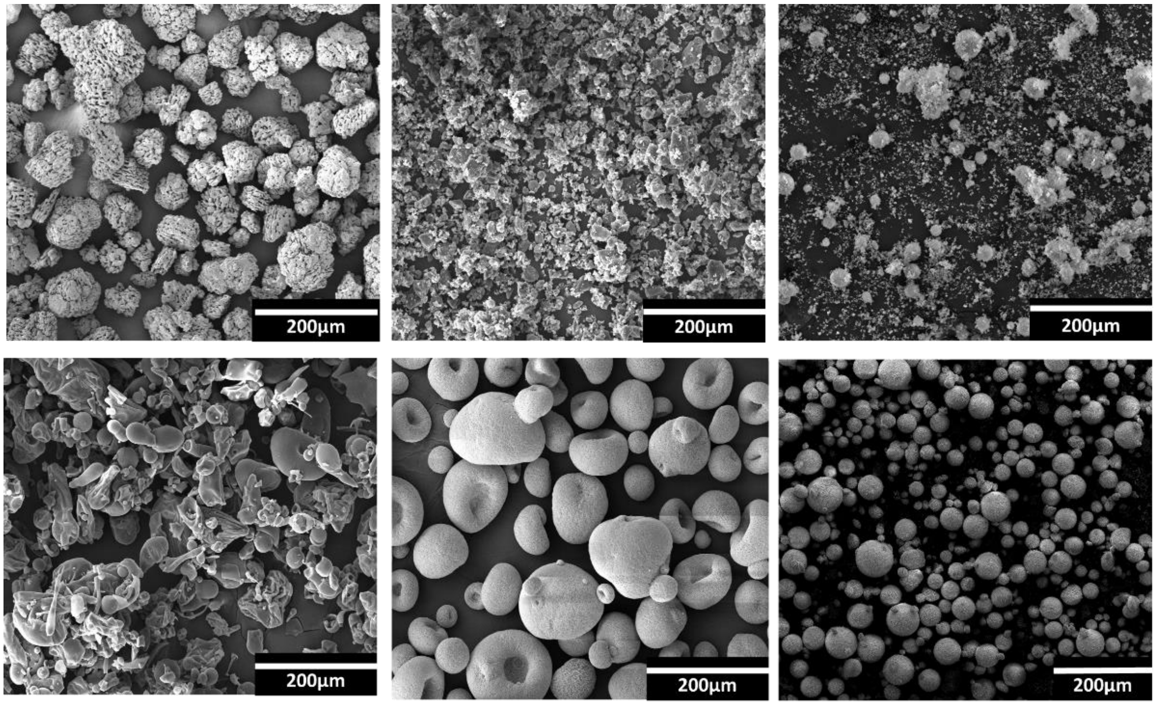

Figure 6.2.1.1: Scanning electron microscopy images of initial raw powders (Top left: alumina, Clockwise: sugar, hydroxyapatite, spherical zirconia, maltodextrin and irregular zirconia).

6.2.2 Sacrificial Molds

The sacrificial mold was solvent jetted using the sacrificial powder mixture made from maltodextrin, sugar and alumina or zirconia. Using traditional methods, such as SIS, the size of the part is limited because the whole powder bed is placed in the oven for sintering, thus, the size of the powder bed is limited by the size of the furnace. This is particularly an issue with high temperature materials given that most high temperature furnaces are smaller in size.

There are three aspects of the sacrificial mold that contribute to easy part removal: sintering inhibition, swelling and densification behaviors of the mold and article powders. As seen in Figure 6.2.2.1, the water-based ink that activates the binder creates a large neck (indicated by the arrows) between the alumina particles. These necks push the alumina particles far away from each other, sometimes by a relatively large distance. The coalescence of particles during sintering becomes difficult as the distance between particles increases and, in this way, sintering is inhibited in the sacrificial mold.

The swelling phenomenon can be explained by analyzing the SEM images of the CIPed green sample and taking normal outgassing of binders into account. Because both sugar and maltodextrin are carbon-based polymers and the sintering conditions are in air, the binders will react with oxygen to create carbon dioxide, a gas, that needs to be released After pressing, the open space available for the binder to escape is reduced significantly, therefore, when the binder is decomposing, it releases a significant amount of gas very quickly, pushes against the sample itself and makes it swell. From the DSC (SDT Q600, TA Instruments) conducted for both binders (Figure 6.2.2.2), it can be observed that both sugar and maltodextrin begin to decompose at around 200 ºC as shown by the %weight loss curve. Sugar and maltodextrin produce the explosive swelling at around 480 ºC and 580 ºC, respectively, as shown by the arrows. By 600 ºC in the cycle, both binders reach 0% weight, and it can therefore be assumed both binders are removed by the end of the cycle.

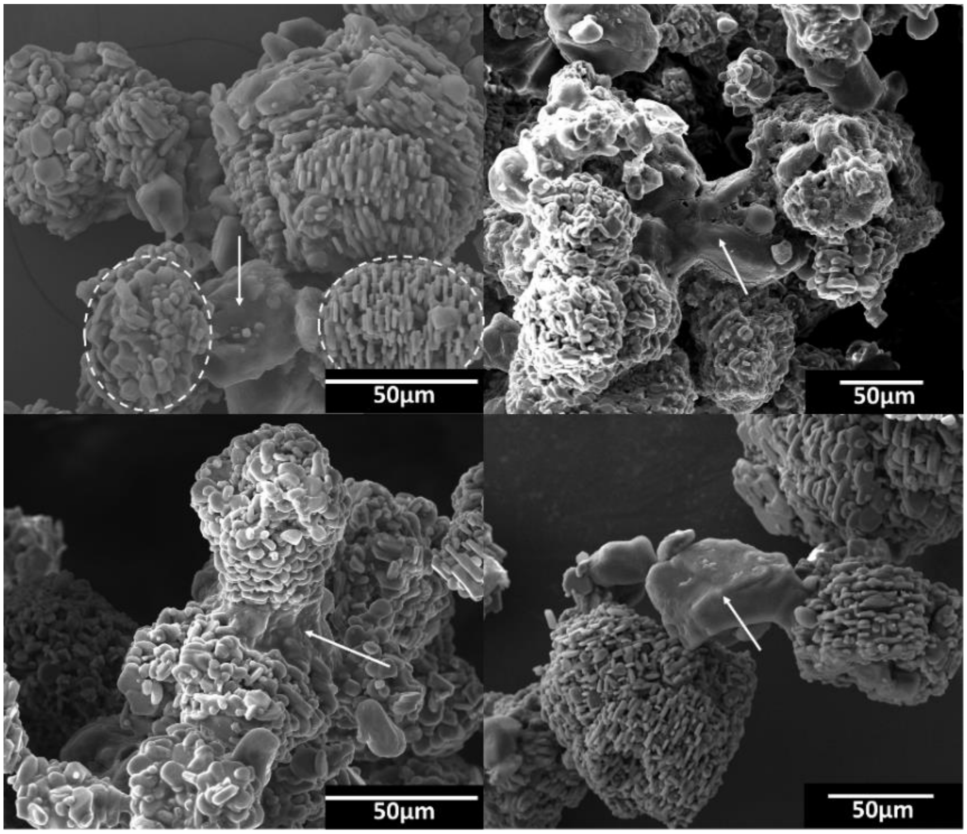

Figure 6.2.2.1: Binder neck formation between alumina powder particles formed during solvent jetting. Dashed lines encircle the alumina particles and the arrows point out the binder neck.

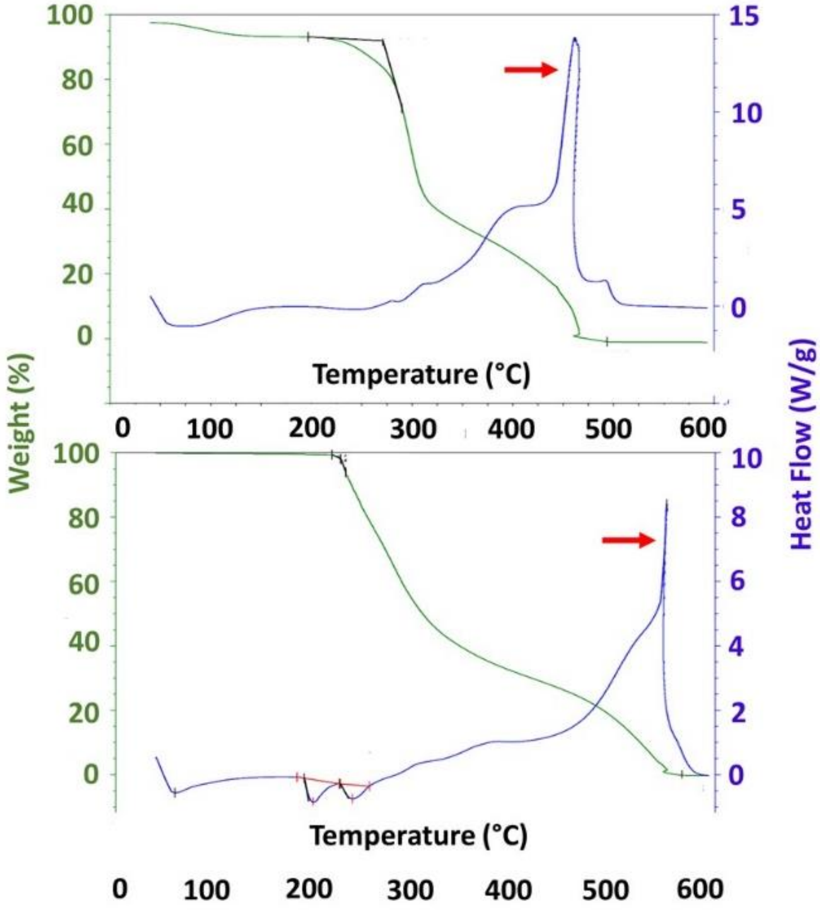

Figure 6.2.2.2: DSC plots of binders; Maltodextrin (top) and Sugar (bottom) showing the additional thermal expansion of each binder component with the arrow once decomposition is completed.

To confirm the above assumption, dilatometry was performed on the pressed sacrificial mold material. The dilatometry plot shown in Figure 6.2.2.3 shows an expansion at 100 degrees Celsius. This is at a lower temperature than was identified in the DSC for sugar and maltodextrin. This is attributed to the fact that the mold was pressed with 400 MPa pressure with the moisture from the print still in the sacrificial material.

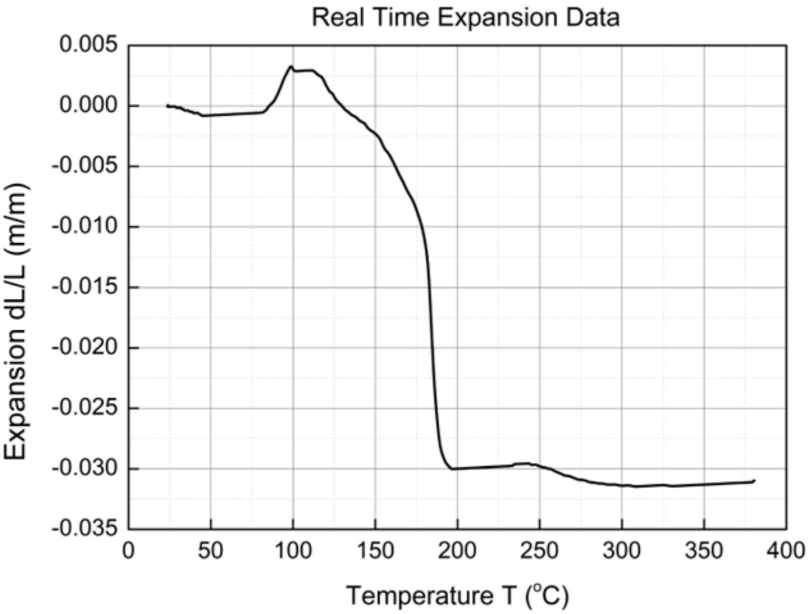

Figure 6.2.2.3: Dilatometry for the sacrificial mold material after cold pressing.

Lastly, the general densification behavior during sintering of the article powders and the sacrificial mold explains how their behavior aids in the removal of the target part. As the sintering cycle progresses, the article powder density increases exponentially while the sacrificial mold density decreases. Additionally, alumina has a higher sintering temperature than zirconia giving the sacrificial mold no opportunity to densify even at the highest temperature of the sintering cycle.

Attention must also be given to the fact that using the present method, the final part will be made up of only the article powder without the need for a long debinding process. Debinding is complex and time-consuming; sometimes taking a few days and multiple sintering cycles. Also, after debinding, some binder elements may remain in the specimen's volume and generate gas pressure during sintering, which impedes the sintering process resulting in low relative density and an adverse effect on the mechanical properties of the final products. This is avoided because the article powder is binder-free from the start.

6.2.3 Microstructural Analysis of Final Parts

To illustrate the ability to produce complex shaped components, a dental crown, hourglass shape and gears were fabricated by AM-SS. The dental crown was studied in detail given that it was a complex shape and made from the Zpex smile, a material used in industry. The relative density of the manufactured dental crown is ~97% which cannot be obtained by traditional solvent jetting approach. In powder metallurgy, a density in this range may not be considered high density but for ceramicists using free sintering, this result is among the highest reported.

The final density of ~97% was obtained using the Archimedes method and confirmed with SEM imaging. Grain size was found to be small (< 40nm) as in Figure 6.2.3.1. Small grain sizes are desired for improving mechanical and optical properties. The level of translucency was tested by using a laser as demonstrated in Figure 6.2.3.2. This material is highly translucent indicating the fabricated crown has a high density and a small average grain size [196].

Using this approach, other geometries were produced to experiment with the geometry. A pair of alumina gears with an internal channel were successfully fabricated. This demonstrated the ability to have internal channels despite needing a swelling action to take place. The gear has an internal diameter of 3mm and outside diameter of 15mm from one end of the tooth to another. The hourglass also seen in Figure 6.2.3.3. demonstrated the ability to design intentional curvature on the outer vertical walls of components.

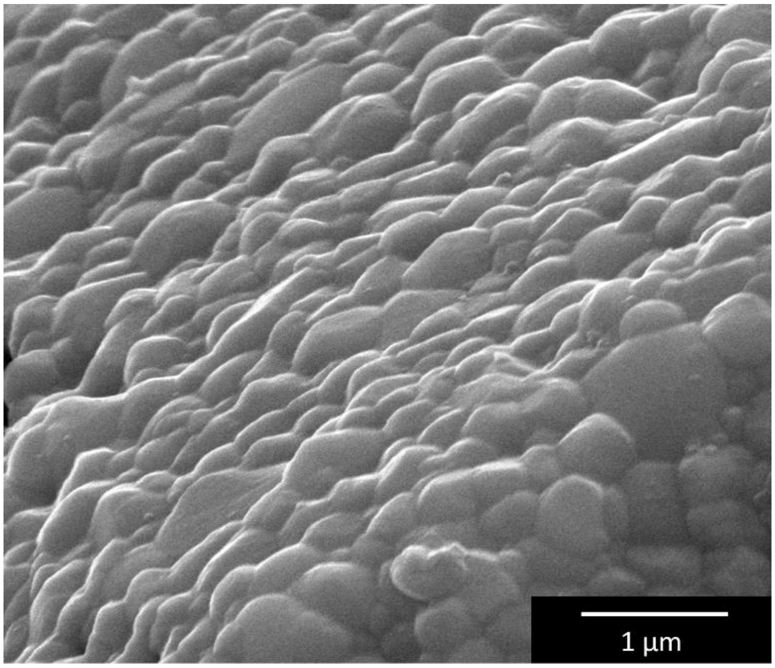

Figure 6.2.3.1: Microstructure of zirconia dental crown.

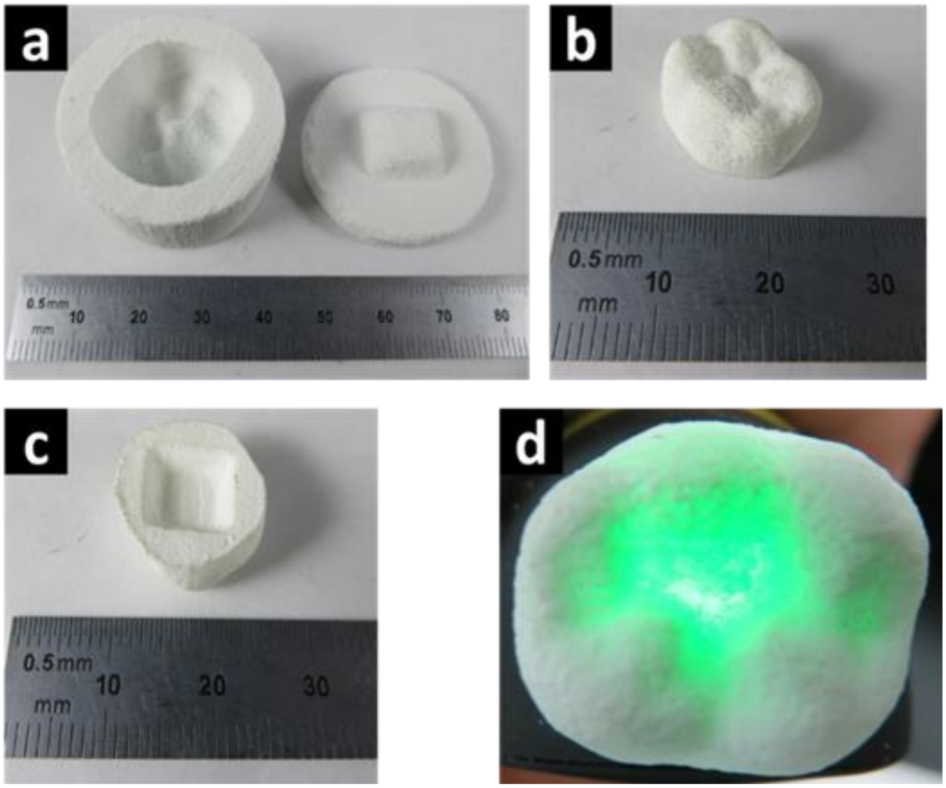

Figure 6.2.3.2: Final dental crown a) sacrificial mold b) top of sintered dental crown c) bottom of sintered dental crown d) translucency test demonstrating small grain size.

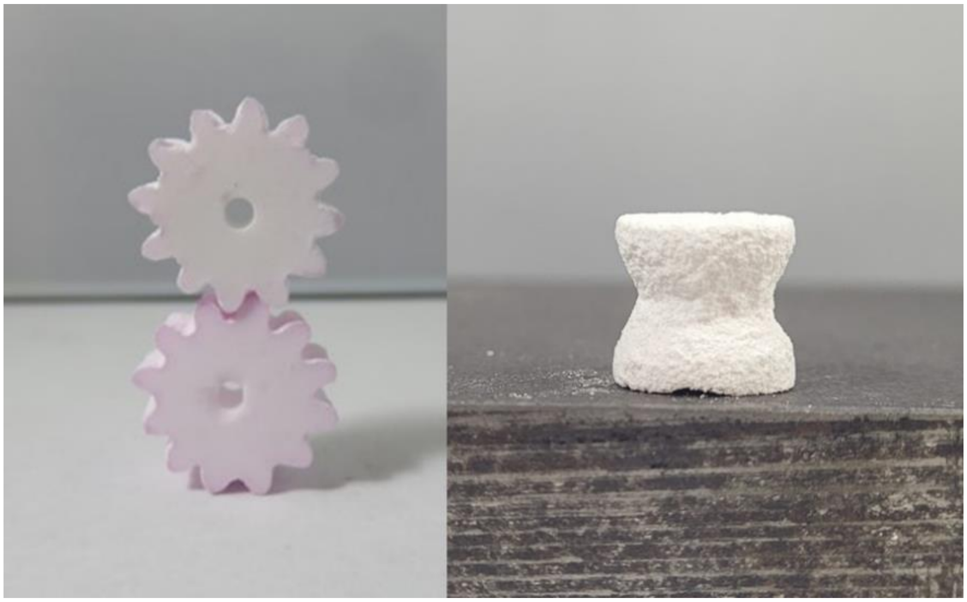

Figure 6.2.3.3: Alumina gears and zirconia hourglass.

6.2.4 Deformation and Shrinkage During Isostatic Pressing

Although there was no clear deformation when pressing complex geometries detailed above, the cylindrical geometry experienced severe deformation. A simple 10mm by 10mm diameter cylinder was used to analyze the deformation and shrinkage experienced by the mold and powder during Cold Isostatic Pressing (CIP). A straight walled cylinder mold was printed and seen in Figure 6.2.4.1(a) along with a same diameter lid (not pictured). There was an expected deformation during the pressing of straight cylinders that can be seen in Figure 6.2.4.1(b). Because the component is not sintered after CIP, it is difficult to directly measure the curve on the green pressed sample, however, the deformation on the final sintered sample (Figure 6.2.4.1(c)) can be measured using the CMM. Deformation happens on the top of the cylinder as well as the side of the walls.

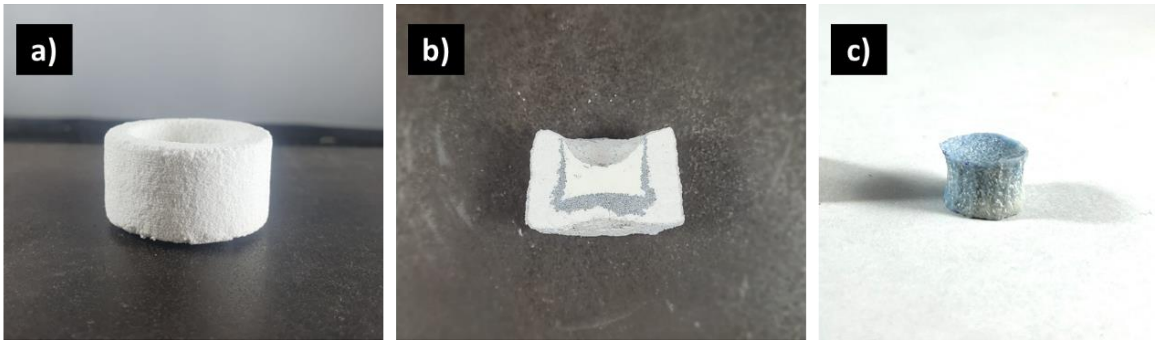

Figure 6.2.4.1: Cylindrical sample a) alumina sacrificial mold after printing, b) mold and article powder after CIP and c) HAP part after sintering.

6.2.5 Cold Pressing and Sintering Model

The continuum theory of sintering can also be utilized to model the pressing process of the AMSS technique. To use equation 2 for CIP, the effective stress σ(W) is replaced by the yield stress σ(y) of the porous material:

$$\sigma_{ij} = \frac{\sigma(y)}{W}\left[\varphi\dot{\varepsilon}_{ij} + \left(\psi - \frac{1}{3}\varphi\right)\dot{e}\delta_{ij}\right] + P_L\delta_{ij}$$

Additionally, there is no sintering stress, therefore, the equation above can be simplified to:

$$\sigma_{ij} = \frac{\sigma(y)}{W}\left[\varphi\dot{\varepsilon}_{ij} + \left(\psi - \frac{1}{3}\varphi\right)\dot{e}\delta_{ij}\right] \quad (11)$$

This code was embedded into COMSOL Physics. The yield stress for the sacrificial mold material and the article material was found either in literature or in SPS data from other research studies in this work. Figure 6.2.5.1 shows the deformation of the cylindrical sample. The concavity of the top and bottom can be seen as well as the waist forming along the side wall of the cylinder.

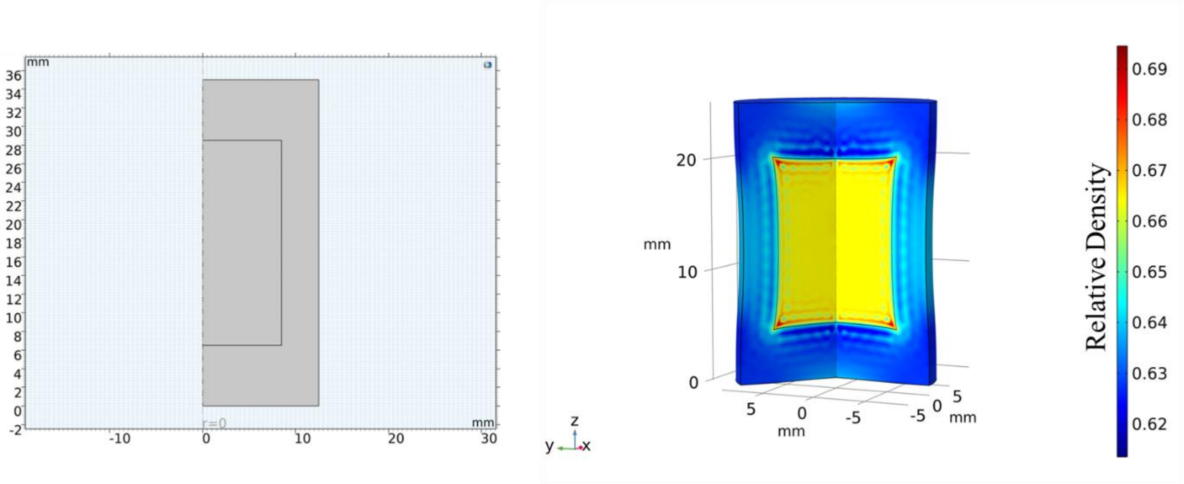

Figure 6.2.5.1: Initial geometry in 2D (left) and final waisted deformation (right) of the alumina sacrificial mold and hydroxyapatite after cold isostatic pressing.

Four cylindrical scaffolds were made using the AMSS approach with an alumina sacrificial mold and hydroxyapatite powder. Unfortunately, an exact measurement of the concavity of the top and bottom was not possible as the sample would break apart when attempting to remove the sacrificial mold after pressing.

Once the density and deformation from pressing were determined by the model above, the final configuration of the article powder was taken as the input for the free sintering model. The same free sintering model used in chapter 5 was used for the final step of this AMSS process. As can be seen in Figure 6.2.5.2, the deformation seem in the simulation was very close to the experimental result seen in Figure 6.2.4.1(c). In addition to predicting the final deformation of AMSS samples, there is also the possibility to use this model to determine the initial geometry for the printed mold. For example, Figure 6.2.5.3 demonstrates how by designing the initial geometry of the sacrificial mold, one can arrive at the desired straight walled cylinder after pressing and sintering.

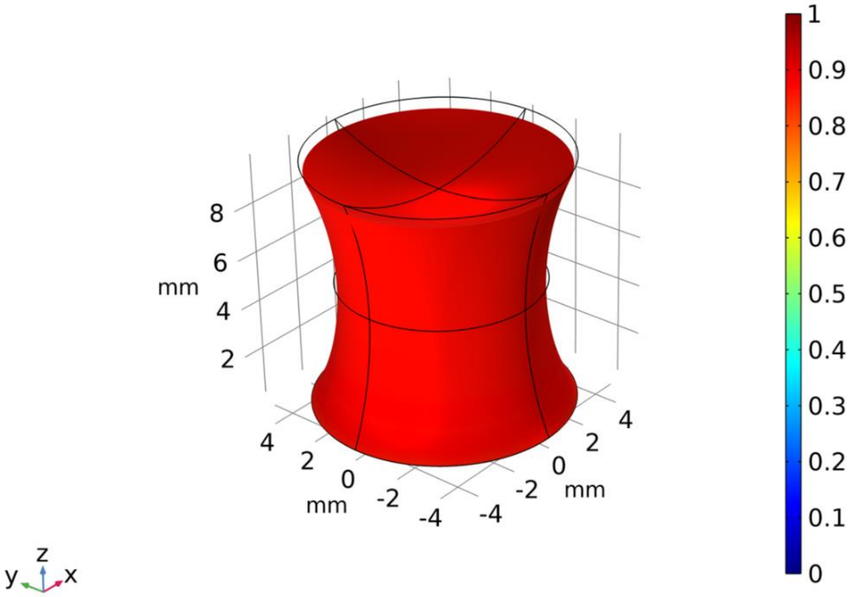

Figure 6.2.5.2: Sintered AMSS cylindrical sample demonstrating deformation that occurs after cold isostatic pressing and sintering.

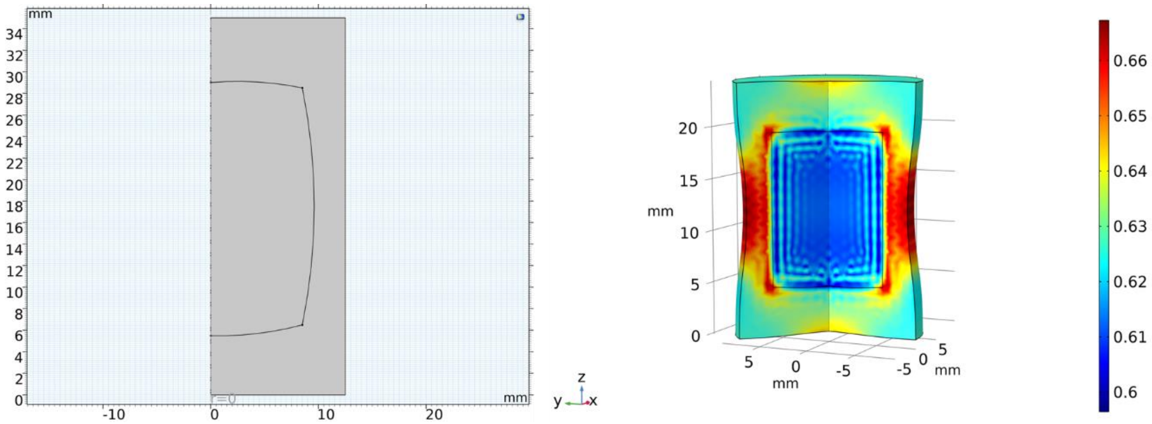

Figure 6.2.5.3: Sintered AMSS Cylindrical sample demonstrating the ability to design initial shape for a desired final geometry.

The coordinates of the top surface in the scaffold simulation seen in Figure 6.2.5.2 were extracted using point probes in COMSOL. The point probes follow a point on the sample during the sintering simulation and are given in an exportable table format. The coordinates for the top surface of the experimental scaffold seen in Figure 6.2.4.1(c) were attained using the CMM. Both sets of data were exported to excel and plotted on the same graph to compare the two results. In the vertical axis, the displacement on the Z direction is shown and the x-axis correlates to the distance along the diameter of the sample. The plot seen in Figure 6.2.5.4 shows that the model and the experiments have a good agreement. There is a slight deviation in the experimental data due to the surface roughness on the scaffold. Again, in the case of bone scaffolds, a random surface roughness is desirable for bone cell adhesion.

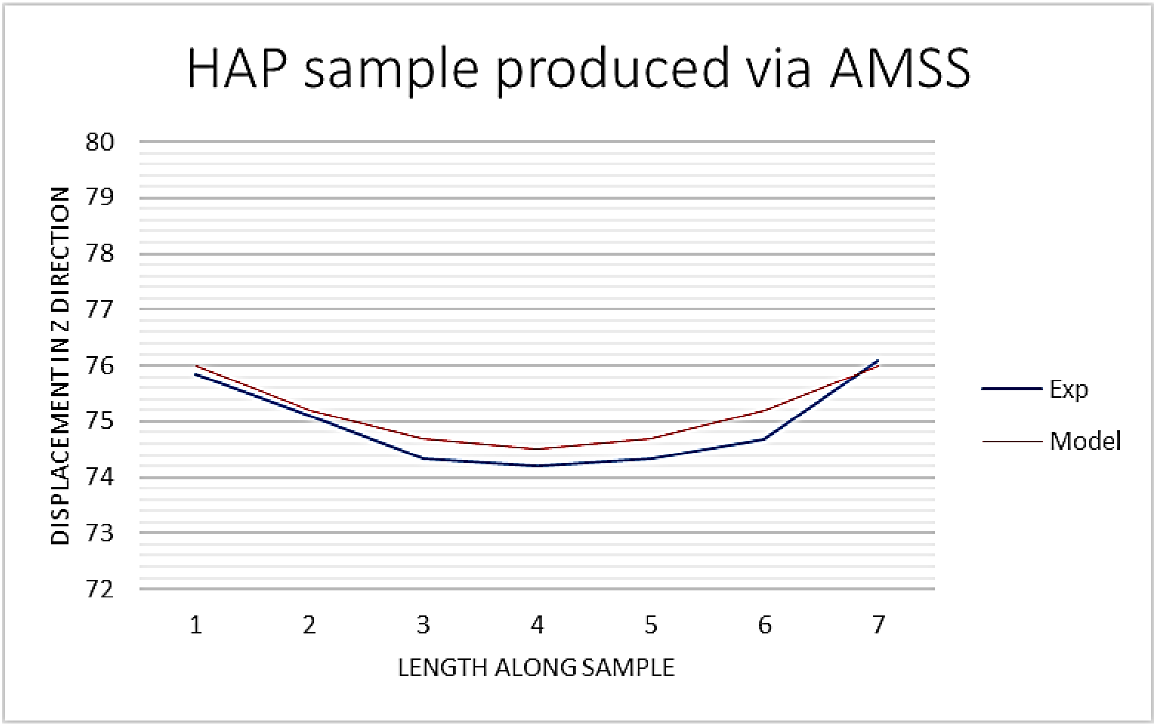

Figure 6.2.5.4: Comparison of distortion at the top of cylindrical sintered samples, experimental versus model results.

6.3 Discussion

A traditional powder-based printing process produces 3D shape components with low green density, which prevents the densification during the follow-up sintering. Furthermore, the article powders used in printing usually have binders inside their volume, therefore pressure-assisted consolidation technologies like the cold isostatic pressing applied in this work cannot be applied because the binder inside would generate shape distortion or cracks during the sintering process. In the present work, the article material (Zirconia or HAP) are pure raw powders without binders; hence the pressure can be applied without shape distortion or crack generation. By pressing the sacrificial mold and the article powder at the same time, the green density of the green part can be increased to a level higher than 50%, so that it is ready to be fully consolidated during sintering and can achieve full density under the optimum temperature settings.

In addition, the AM-SS approach enables the usage of nano-sized powders, which are typically not utilized in powder-based printing due to their limited flowability. The use of nano-sized powders is desired due to its initial small grain size and enhanced sinterability. Small grain sizes are desirable because they are known to provide higher mechanical strengths and some translucent optical properties. Furthermore, small particle sizes are more sinterable than micron sized powders. Using nano-sized powders renders a lower sintering temperature and small average grain sizes in the final complex parts, which is not traditionally achievable by powder-based 3D printing.

There is one more advantage to AM-SS regarding the productivity. This method enables the avoidance of the use of pressure-assisted sintering, which otherwise generally becomes a roadblock to mass production. Using the 5 step AM-SS process described in the present work, many parts with different or same complex shapes can be obtained in a straight-forward manner with no need for curing, debinding or infiltration which are techniques generally used to increase density of final parts produced via powder-based printing.

Finally, there is the question of shape deformation. Although there is some deformation during the CIP process, it can be remediated by taking the deformation into account in the sacrificial mold. The predictive tool can ensure that the final geometry is the desired density and shape which is important since the most valuable aspect of additive manufacturing is the ability to create complex geometry.

6.4 Chapter Summary

High-density ceramic parts were fabricated using the novel technique of Additive Manufacturing combined with Subtractive Sintering (AM-SS). Main advantage of this process is that, unlike traditional methods such as investment casting or slip casting, the mold does not require a difficult removal process. In AM-SS, the mold essentially removes itself during sintering which reduces the processing steps from 10-12 (investment casting) to 5. Furthermore, given that the article powder is placed in the mold in its raw form, the possibilities of materials that can be fabricated using this method is more diverse than with any other technique in literature.

A potential limitation exists with geometry due to the nature of the process. Because the process depends on the swelling, internal channels and structures become difficult to produce, yet not impossible. Initial experiments show that internal structures with a small diameter relative to the size of the overall shape can be successfully produced as was proven by the alumina gear fabricated in this work.

Overall, the present work demonstrated the potential of AM-SS in producing high density complex shaped parts from any material with free sintering and without the need of a long debinding process. Additionally, a predictive model developed in this work was able to accurately predict the shape deformation and shrinkage of the components. This tool can be used prior to printing to design the initial size and shape of the sacrificial mold making this AM-SS method applicable in most industries.

Chapter Acknowledgements

Chapter 6, in part, was published as it may appear in Additive manufacturing, 2020, Lee, Geuntak; Carrillo, Maricruz., Elsevier. The dissertation author was the primary researcher and co-author of this paper.

7 FABRICATION OF POWDER COMPONENTS WITH INTERNAL CHANNELS PRODUCED BY SOLVENT JETTING AND SPARK PLASMA SINTERING

In the previous chapter, it was demonstrated that applying pressure to printed samples was an effective way to increase the green density and sinterability of the components. By applying pressure, ceramic parts with a density as high as 99% were produced. However, using the AM-SS, the geometry is limited to one internal cavity that is smaller than the overall component. In the case of producing an internal cooling channel for a heat exchanger or osseointegrating channels for a bone scaffold for example, more complexity is necessary.

Spark Plasma Sintering (SPS) is a materials processing technology which involves the simultaneous application of pressure and electrical field to consolidate powder materials [197]–[199]. It is well known for its capability to rapidly densify even those materials (such as carbides and other high temperature systems) which cannot be consolidated up to high density by traditional sintering technologies. Due to the fast-heating rates that can be reached, it is able to retain the grain size even in nanosized grain materials [200]–[203]. Despite the SPS technology’s potential to produce components with high mechanical properties and tailored microstructures, it is limited to the production of simple shape components, such as cylinders. This limitation derives from the inhomogeneity that is usually introduced by the application of pressure to components with complex shapes that have different thickness in the direction of pressing [204]–[206]. In the uniaxial compaction the thinner areas densify earlier and prevent the punches to completely densify the entire component [207]. Different approaches to overcome this limitation have been utilized [204], [205], [208], [209]. These methods, including the more recent ones proposed by Manière et al. [210] have been focused on the netshaping of the external geometry of the components. But in many applications the fabricated components need to have internal features such as channels or holes.

In the biomedical industry, ceramics requiring internal cavities are being used mostly for orthopedic applications such as bone tissue engineering, bone implants and scaffolds. Methods for producing internal structures synthetic implants include salt leaching [31], freeze drying [87], gel or chemical forming [211]. Current techniques have limitations in the ability to include or tailor external and internal geometries. Internal architecture is important in mimicking bone because these channels allow nutrient absorption and cell adhesion [104]. AM becomes particularly attractive for orthopedics due to the ability to tailor the geometry of scaffolds and implants to the patient specific injury; however, internal structures and channels are difficult to produce with AM [212]. High density ceramic components with complex external geometry can be designed and produced using printed molds and applying pressure before free sintering as done in previous work (Chapter 4) [213]. Producing a high-density bio-ceramic however adds a level of difficulty due to their high melting temperature yet low phase transition temperature. To retain the biocompatibility of Hydroxyapatite (HAP) for example, one must sinter at temperatures below 1300 °C [214].

Internal channels are also important for ceramic components involved in various energy applications such as solar cells, wind rotors and heat transfer devices [215]. When considering manufacturing of channels, the main concern is removing material from inside the designed openings. Traditionally in energy applications, ceramic components with channels are made by slip casting or injection molding in two pieces and then joined leading to potential early failures, or through-hole channels can be machined out adding to the cost. Self-supported 3D printing techniques such as binder jetting and stereolithography (SLA), are being considered for parts that require internal channels. Singh et al., chose binder jetting to successfully produce a prototype of a one-piece ceramic heat exchanger [216], highlighting the advantage of AM by producing a complex internal structure in one print. However, a high density was not achieved despite the long debinding and sintering cycles used.

Microsystems, to include micro-electrical mechanical systems (MEMS) and micro-fluidic devices have been investigated widely in recent years with the demand for smaller components for electronics and testing [217]. Current silicone-based manufacturing methods limit the 3D geometry of the microsystems and have become difficult to source [218]. To address the manufacturing of ceramic microsystems with small internal channels, Do et al., propose using a 0.9 mm thick machined graphite shape, inserting it into alumina powder, pressing them together and then removing the graphite by annealing in air. A micro burner was successfully produced using this approach; however, the geometry of the internal structure is limited to the cutting machine and by the thickness of the graphite sheet. In another study, Nawrot et al., assessed the applicability of Stereolithography to microfluidic devices [219]. Although they were able to successfully create channels with an optimized sintering cycle that limited deformation, using SLA required a long debinding time and not all channels were able to fully penetrate the whole structure making this technique non-transferable into high output production situations.

Overall, in traditional ceramic manufacturing, conventional (free) sintering is the most common method for consolidating ceramics. In additive manufacturing, SLA has been the most common 3D printing method being explored for ceramic components with internal channels and cavities [33]. However, there are issues with both traditional and additive manufacturing methods. The removal of the polymer, the inability to completely remove this polymer and long debinding times limit the applicability of advanced ceramics in industry. There is opportunity to use advanced sintering methods as a tool to address the shortcomings mentioned above.

In this study, a novel method of producing complex ceramic and metallic parts with designed internal channels is proposed. Using solvent jetting, a graphite structure can be printed to serve as a mold or shaper for the article (target) powder that is to be sintered. The article powder is then placed inside the mold in the raw form with no binder or preparation necessary before placing in the Spark Plasma Sintering (SPS) machine. This method brings many benefits in producing complex shape with internal channels. Along with geometric customization of the 3D printed mold, a major advantage of this method particularly for ceramics is the removal of the need for a long debinding process, usually necessary with other 3D printing methods, by using the SPS. Furthermore, because the graphite does not sinter, it is very easily removed from the internal channels and cavities via sand blasting and any remaining graphite can be decomposed in air via annealing. Additionally, sintering time is drastically reduced using the SPS which leads to high density and small grain growth. High density ceramic and metallic complex parts with internal channels were successfully produced with close to theoretical densities.

7.1 Materials and Method

7.1.1 Powder Preparation

The printing powder for the graphite sacrificial mold was prepared in advance by mixing graphite powder (Atlantic Equipment Engineers, 325 mesh) with sugar and maltodextrin in a conventional dry mixer (Turbula®, WAB-Group, Switzerland) for 60 minutes. The main component of the powder is graphite and makes up 75 wt% of the mixture;

powdered sugar (Wholesome) and maltodextrin (Pure Organic) were used as binders and equally make up 25 wt% of the mixture (12.5% sugar and 12.5% maltodextrin). Alumina powder (Materion, Al2O3 99.2% pure, 325 mesh, Phoenix, AZ, USA) was used as an electrical insulator to protect the ceramic article powder. Hydroxyapatite (HAP, CAPTAL 30, Plasma Biotal Limited, United Kingdom) and Stainless Steel (SS316L, OzoMetal, USA) were chosen as article powders for the study. Although stainless steel is not a bioceramic, it is often used for bio implants. The ability to use this method to produce metallic components was to be addressed, therefore, stainless steel was chosen as the experimental metallic powder. The particle morphology and particle size of each powder are shown in Figure 7.1.1.1.

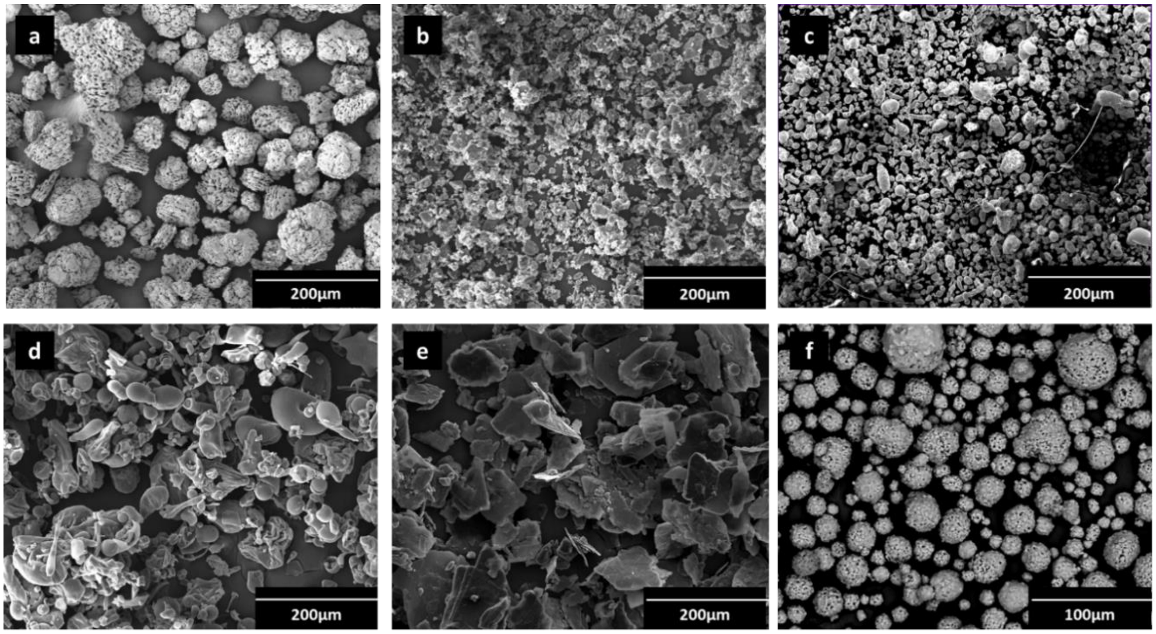

Figure 7.1.1.1 SEM image of raw powders: a) Alumina, b) Sugar, c) Stainless Steel 316L, d) Maltodextrin, e) Graphite, f) Hydroxyapatite

7.1.2 Experimental Procedure

A general overview of the experimental procedure is shown in Figure 7.1.2.1. First, the graphite mold was printed in the custom-made solvent jetting printer described in chapter 3 using the mixed graphite-sugar-maltodextrin powder. Prior to sintering, the mold was subject to partial debinding, in vacuum for one hour at 850 °C. Then, the mold was filled with an article powder, samples were set up appropriately and subjected to Spark Plasma Sintering. All the experiments were carried out using an SPS device (SPSS DR.SINTER Fuji Electronics model 515, Japan). After sintering, the graphite mold is easily scrapped off due to its higher sintering temperature compared to the article powders. The part is initially cleaned by using compressed air, tweezers (for internal channels) and surface polishing if necessary. The sample set-up and cleaning process for metallic and ceramic powders differed slightly and will be described separately below.

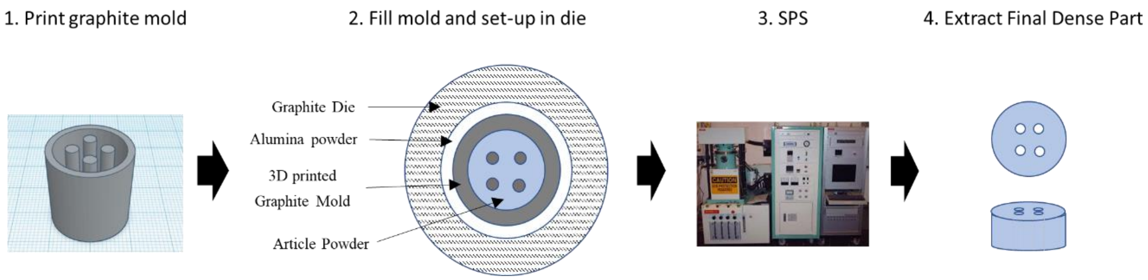

Figure 7.1.2.1: General experimental procedure for graphite sacrificial mold via SPS approach.

Hydroxyapatite (HAP) was chosen as a proof of concept for using this method with ceramic materials due to its biocompatibility and potential use in biomedical applications. HAP is a delicate material that must remain under 1300 °C to avoid a phase transformation which diminishes its biocompatibility, therefore, extra precaution was taken using the SPS device by electrically insulating it with Alumina powder. A 35mm diameter graphite die was used for the tooling to surround the HAP powder and mold with alumina powder. For other materials, the alumina powder might be not necessary. The HAP samples were sintered at 1200 °C with a dwell time of 60 minutes. A pressure of 25 MPa was applied gradually once the sample reached maximum temperature. The SPS was allowed to cool before starting the cleaning process. The part is then placed in a furnace (without vacuum) up to 900 °C and held for 60 minutes to allow the remaining graphite to decompose. If there is any residual powder or a different surface roughness is desired, various sand blasting media are available to finish the part. Glass beads (80-100 grit, Interactivia) were used to finish the ceramic sample and to accentuate the surface features for bone implant applications.

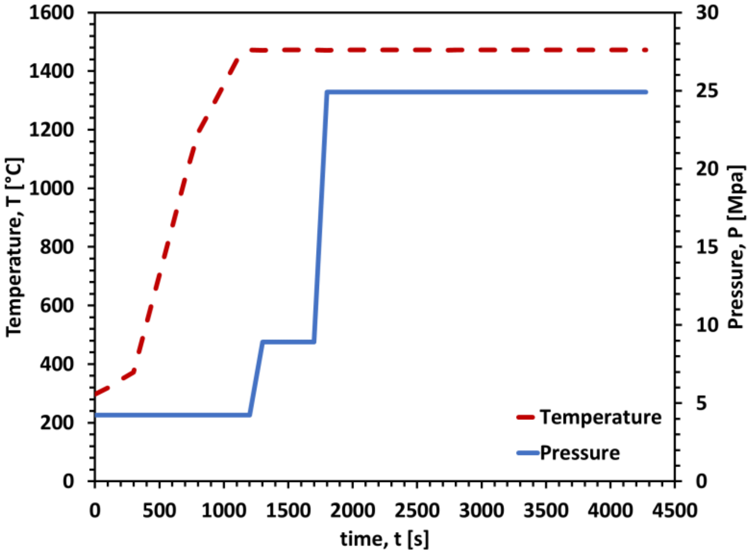

Figure 7.1.2.2: Process parameters used for the SPS process of the 4-channels HAP component.

Stainless Steel 316L (SS316L) was chosen to show the applicability of this method to metallic materials due to its versatility and ubiquitous use in industry. In this case the graphite sacrificial part was designed in order to create an internal channel in the sintered specimen. For this aim a loop made by graphite was produced following the procedure described above, and after inserting it in the SPS die the remaining space was filled with the stainless-steel powder. The powder assembly was then sintered at 950 °C for 20 minutes applying 50 MPa pressure once the sintering temperature was reached Figure 7.1.2.3. Once the component was extracted from the die, the graphite powder was removed to reveal the channel inside the specimen.

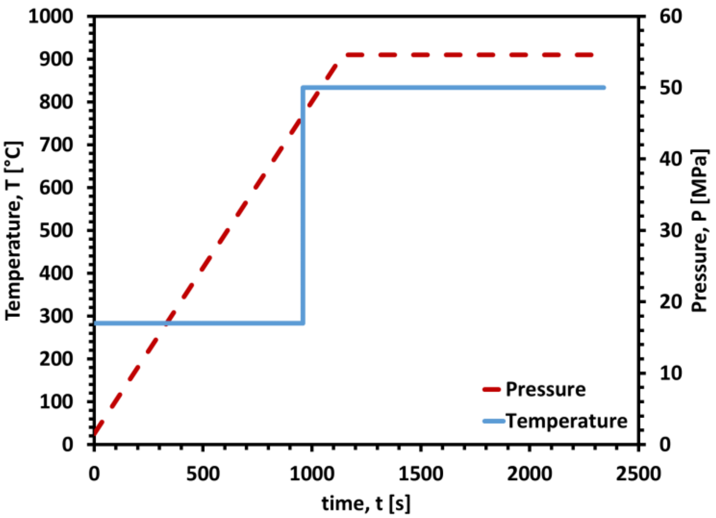

Figure 7.1.2.3: Process parameters used for the SPS process of the stainless-steel component.

7.1.3 Characterization

Density measurements of all components in the sintering cycle (Alumina powder, graphite mold, HAP powder, Stainless Steel powder) were necessary as input parameters for the finite element model. The theoretical density of the printing powder and mold was determined using a helium gas pycnometer (Ultrapyc 5000, Anton Paar, Austria). Relative densities of printed molds and tap densities of the powders were then determined via the geometrical measurement method. The bulk densities of the sintered parts were estimated using the Archimedes’ immersion method following ASTM standard C373-18.

Scanning Electron Microscopy (FEI Quanta 450, FEI, Hillsboro, OR, USA) was used on polished and etched surfaces to analyze the microstructure of the material; grain size and porosity were assessed. The ceramic sample was thermally etched at 950 °C for 30 minutes and the metallic surface was chemically etched. An additional step was required for the ceramic parts to confirm the phase composition of the HAP sample. X-Ray Diffraction (Bruker D-8 diffractometer, MA, USA) was used utilizing CuKα radiation at room temperature.

7.1.4 SPS Modeling

Spark Plasma Sintering is a process where three main physical phenomena are involved and interconnected: densification, thermal distribution and electrical behavior of the specimens. Powder densification can be modeled based on studies presented in literature [123], [207], [220]–[223]. SPS involves Joule heating [224]–[239], densification and field phenomena [123], [197], [207], [222], [223], [240], [241]. To simulate the thermal and electrical current distribution and the densification during SPS, Finite Element Method (FEM) is largely used [204], [205], [208], [242], [243]. The behavior of the powder assembly during the SPS process is predicted using a model based on the continuum theory of sintering, which has been embedded in a FEM (finite element model) software and validated through the comparison with the experimental results.

The sintering behavior of the powder assembly is influenced by the contribution of the different powders that compose it. Therefore, the components' geometry at the end of the sintering cannot be predicted using the mass conservation law. The sintering model embedded in the FEM software COMSOL Multiphysics® (COMSOL Inc., Los Angeles, CA) allows the prediction of the densification and displacement that occur during sintering resulting in a useful tool for the design of the initial geometry of the components.

The description of mechanic of the powder compact is conducted using the constitutive relationship of the continuum theory of sintering proposed by Olevsky [123], equation 2. The equivalent stress for the SPS of a powder material is based on a power-law creep:

$$\sigma(W) = AW^{m} \tag{12}$$

with m is the strain rate sensitivity exponent, and A (Pa s^m) is the power-law creep coefficient.

$$A = \frac{1}{A_0^m} T^m exp\left(\frac{mQ}{RT}\right) \tag{13}$$

where A_0 (K $Pa^{-1/m}$ s^{-1}) is the power creep factor, T (K) is the absolute temperature, R (J mol^{-1} K^{-1}) is the gas constant, Q (J mol^{-1}) is the power law creep activation energy.

Since the considered process conditions are not sufficient to sinter the graphite powder that compose the sacrificial part, for the graphite the equivalent stress is based on the conditions of cold compaction:

$$\sigma(W) = \sigma_y \tag{14}$$

where σ_y (Pa) is the yield strength.

Considering a porous material, the equivalent strain rate, normalize shear and bulk viscosity, and sintering stress are defined as functions of porosity θ:

$$W = \sqrt{\frac{\varphi\dot{\gamma}^2 + \psi\dot{e}^2}{1-\theta}} \tag{15}$$

$$\varphi = (1-\theta)^2 \tag{16}$$

$$\psi = \frac{2}{3}\frac{(1-\theta)^3}{\theta} \tag{17}$$

$$P_L = \frac{3\alpha}{r_0}(1-\theta)^2 \tag{18}$$

where α is the surface energy (J m^{-2}), r_0 is the particles radius (μm) and $\dot{\gamma}$ is the shape change rate (s^{-1}) defined as:

$$\dot{\gamma} = \sqrt{2\left(\dot{\varepsilon}_{xy}^2 + \dot{\varepsilon}_{xz}^2 + \dot{\varepsilon}_{yz}^2\right) + \frac{2}{3}\left(\dot{\varepsilon}_x^2 + \dot{\varepsilon}_y^2 + \dot{\varepsilon}_z^2\right) - \frac{2}{3}\left(\dot{\varepsilon}_x\dot{\varepsilon}_y + \dot{\varepsilon}_x\dot{\varepsilon}_z + \dot{\varepsilon}_y\dot{\varepsilon}_z\right)} \tag{19}$$

To determine the sintering parameters (strain rate sensitivity and power law creep coefficient), the sintering materials (HAP, alumina, stainless steel) were sintered separately. Using the method described in Manière at al. work [190] that linearizes the constitutive equation for the SPS:

$$\frac{1}{m} ln\left(\frac{|\sigma_z|}{\left(\psi+\frac{2}{3}\varphi\right)^{1+\frac{m-1}{2}}(1-\theta)^{\frac{1-m}{2}}}\right) - ln(T) = -ln(A_0) + \frac{Q}{RT} \tag{20}$$

one can identify the A_0 and Q parameters through the regression of the experimental data for a fixed m value.

The graphite mold was considered to be subjected to cold compaction, and in this case the effective equivalent stress is described as:

$$\sigma(W) = \sigma_y \tag{21}$$

Where σ_y [MPa] is the yield strength and the creep parameter m ~ 0. To determine the value of σ_y, the graphite powder was subjected to the multi-step pressure dilatometry [244], [245].

7.2 Results

The discussion on the experimental outcomes is provided first as a demonstration of the applicability of the proposed method for both metallic and ceramic materials. The accuracy of the electro-thermal-mechanical simulation used to predict the material behavior of the materials during sintering is discussed later.

7.2.1 Experimental

Initial experiments were conducted with a simple one channel geometry (Figure 7.2.1.1). The successful production of a one channel component was difficult. In fact, over 40 experiments were conducted prior to achieving an acceptable result. Some of the parameters that were changed in order to make it work were binder concentration in the sacrificial mold, sintering heating rate, sintering holding time and pressure applied during SPS. The binder concentration was lowered prior to SPS by debinding for longer times in the oven, this helped reduce the cracks significantly. The heating rate was decreased to avoid cracking. When the heating rate is too fast, the diffusion process may not be able to keep up with the rate of temperature increase, resulting in incomplete bonding and poor material properties. This can further increase the likelihood of cracking and other defects in the final product. The holding time at the top temperature was increased to promote more densification which also improved the final component. The amount of pressure applied did not affect the final part, however, it was observed that applying the pressure after arriving at the top temperature yielded better results. This is most likely due to the binder completely decomposing halfway through the cycle.

Figure 7.2.1.1: Initial experimental results with one channel. The printed graphite scaffold with HAP powder inside (left) and the final sample after SPS (right).

Once the proper sintering cycle and parameters were confirmed using a one channel geometry, the geometry was made more complex by adding three more internal channels. A high-density 10 mm in diameter ceramic cylinder with 4 channels was successfully produced using a 3D printed graphite mold and Spark Plasma Sintering (Figure 7.1.2.1). The graphite removal process described above was easy and sufficient in removing the residual graphite. As predicted, the alumina powder and graphite mold did not sinter, leading to easy detachment. The relative density for HAP achieved was 96% and the final grain average grain size was 30 µm as seen in Figure 7.2.1.3. The microstructure in the middle of the sample is similar to the microstructure at the edge of the HAP sample. Initial powder particle size was ~30 micron, suggesting no noticeable grain growth occurring during the sintering cycle. This was an exciting find given that normally there is a heterogenous grain size in the center of the sample and the edge for components fabricated via SPS (See Figure 7.2.1.3). The final HAP sample was analyzed via X-Ray Diffraction (XRD) to confirm HAP was the only phase present as seen in Figure 7.2.1.4. This result is important in confirming the biocompatibility of HAP for biomedical applications. No carbon diffusion from the graphite mold is present in the HAP part due to the partial debinding step taken prior to sintering and the size of the component.

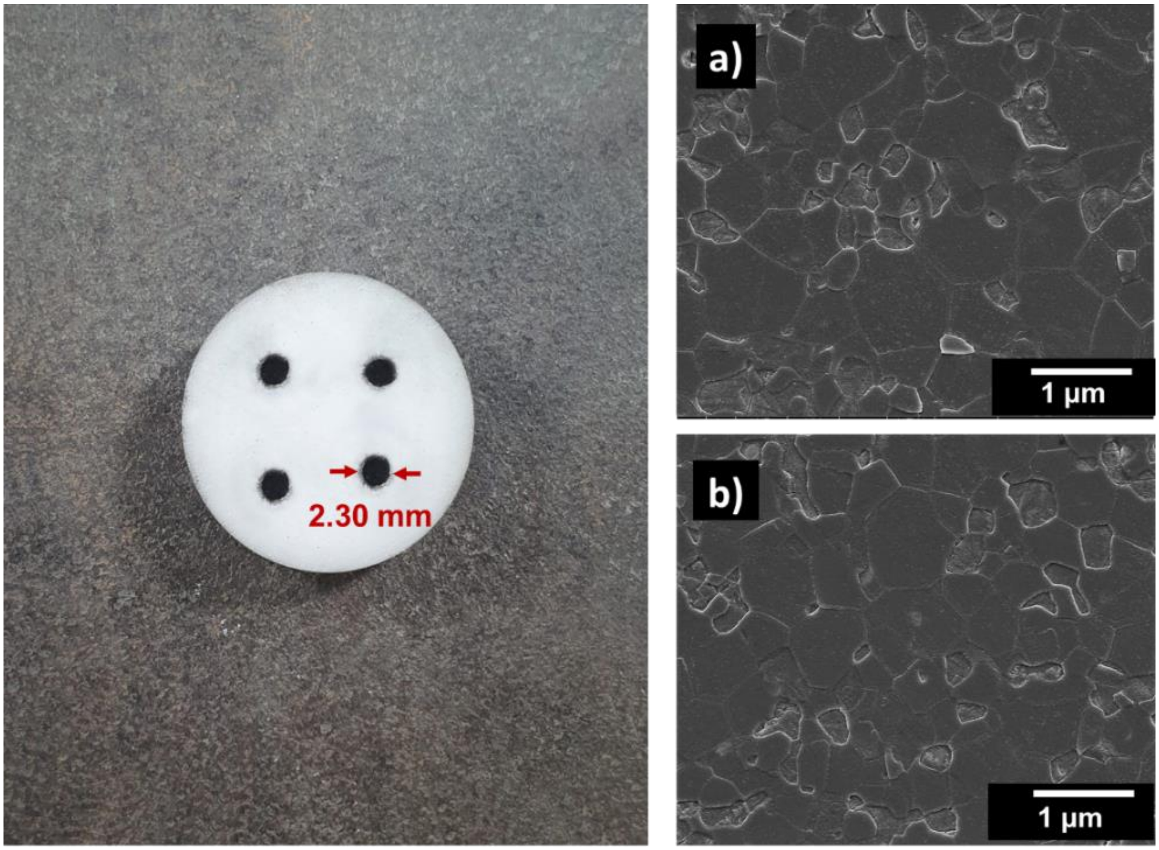

Figure 7.2.1.2: Final HAP cylindrical sample with four channels showing SEM of the heterogenous microstructure, a) center and b) edge.

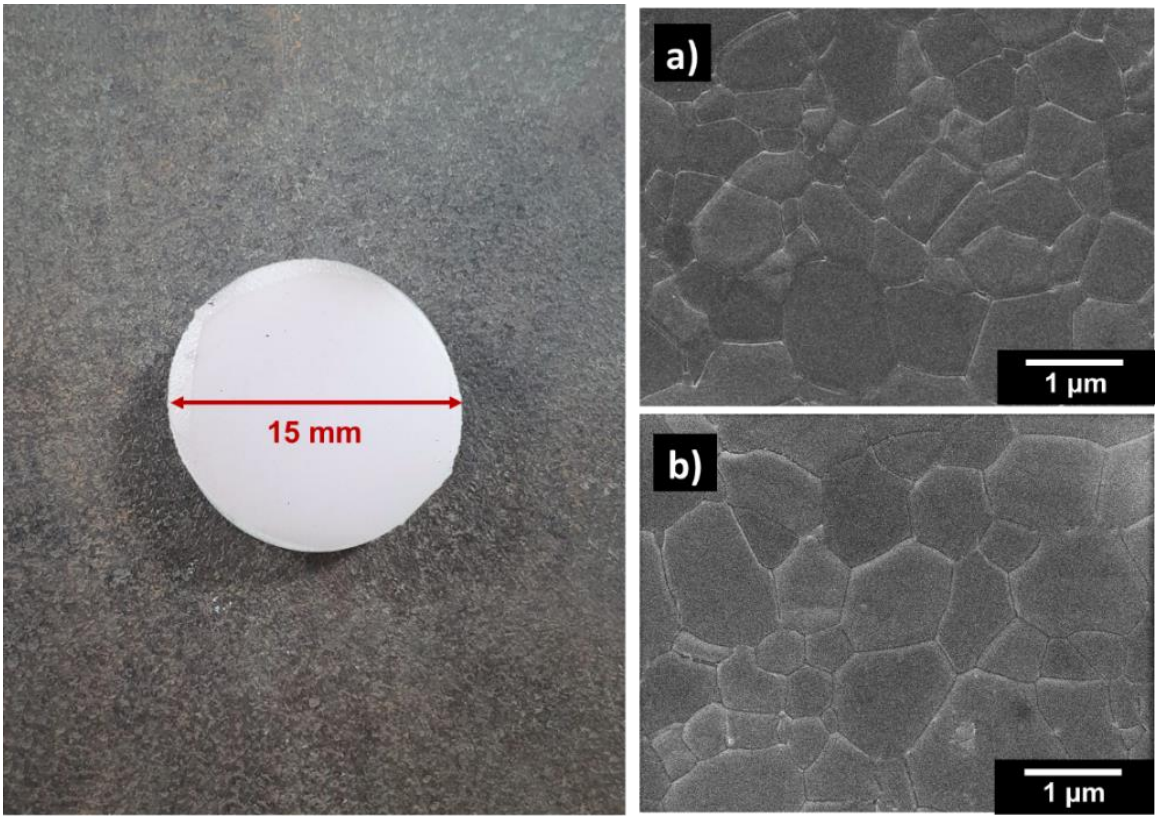

Figure 7.2.1.3: Final HAP cylindrical sample with no channels showing SEM of the homogeneous microstructure a) center and b) edge.

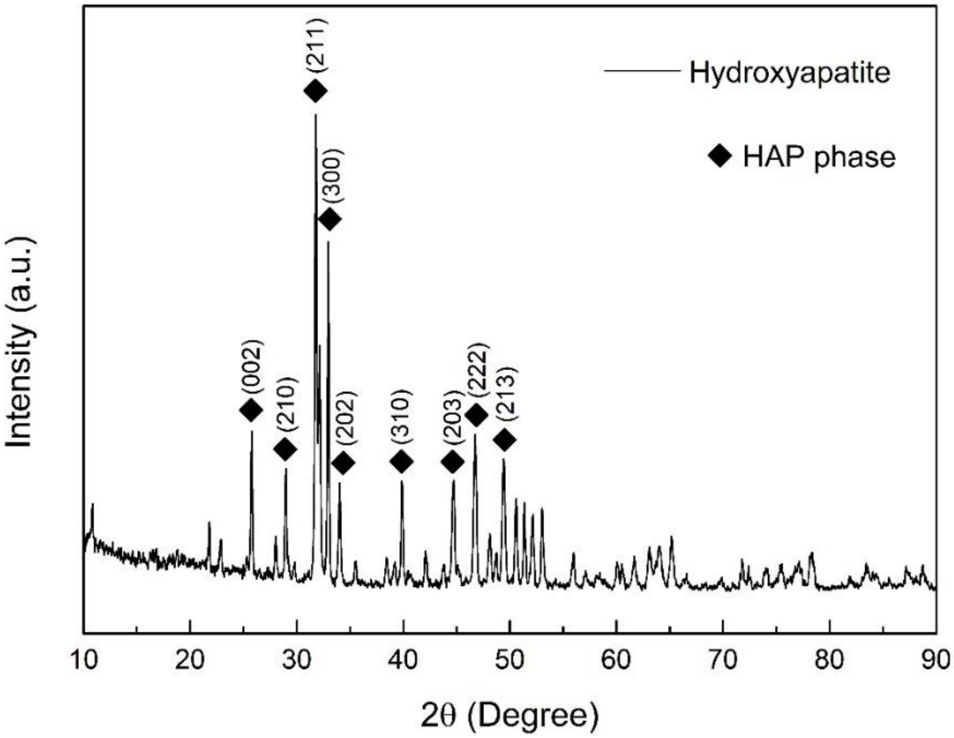

Figure 7.2.1.4: XRD showing pure HAP phase in final sintered part.

Although the outer geometry shown the HAP sample is a disk, changing the outer geometry is possible via the printed graphite mold. As can be seen in Figure 7.1.2.1, the graphite mold was designed to have straight walls, however, these walls can be designed to be any geometry. The geometry of the sacrificial mold dictates not only the internal architecture but the external architecture of the samples as well to attain a variety of final geometries.

To prove the ability to create a complex shape, a human tooth was printed. Using the same approach of a graphite sacrificial mold followed by SPS, the HAP sample in Figure 7.2.1.5 was fabricated. Due to the small size and the use of graphite, carbon diffusion into the sample was observed in the initial attempt to produce this tooth geometry (see Figure 7.2.1.5(b)). After sintering, the sample is covered with graphite as can be seen in part a of the figure below. Most of the graphite is removed with a brush but the final cleaning is done via temperature annealing as described in the methods section. For the initial attempt, the same sintering cycle as the 4-channel component was used. However, carbon diffusion occurred. To mitigate the carbon diffusion on the second attempt, the holding time at the highest temperature was limited to 10 minutes rather than 30 minutes.

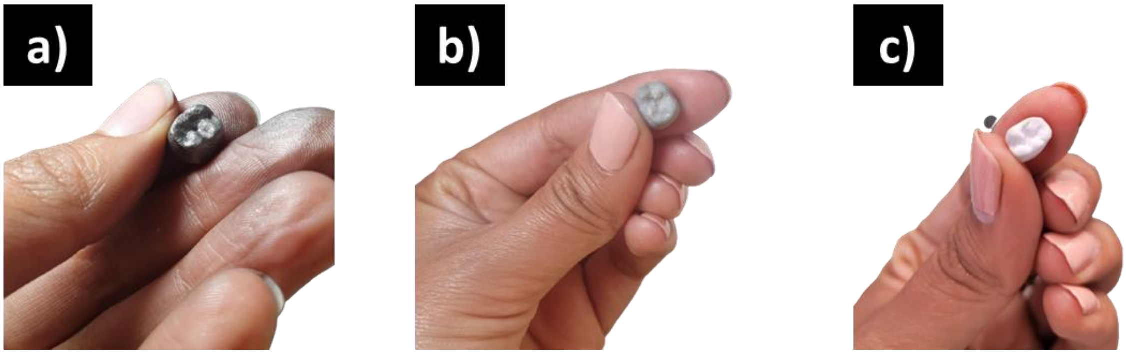

Figure 7.2.1.5: Tooth geometry produced by SPS of graphite sacrificial mold a) post SPS, b) 30 min hold sample (after annealing) and c) 10-minute hold (after annealing).

A fully dense stainless-steel cylinder (15 mm diameter and 10mm height) with an internal curved channel was also manufactured successfully using the proposed method. The design of the channel was chosen to represent a possible loop in a component that requires a cooling system; therefore, a curved cylindrical element with a support to easily insert and keep it centered in the die was printed. Once the printed element was inserted into the die, it was surrounded by stainless steel powder and then the cylindrical specimen with the presence of the curved graphite element was sintered. The stainless steel (SS) part and the cross-section is shown in Figure 7.2.1.6 after cleaning. The surface roughness on the internal channel is due to the resolution of the printed graphite part. In future work, this can be improved by optimizing the graphite powder and printing. A post-processing step for the polishing of the stainless-steel inner channel may be required depending on the application, not necessary for bone replacement.

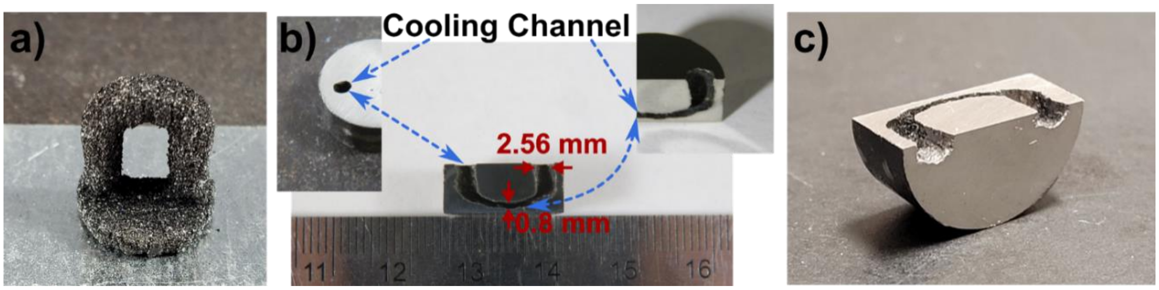

Figure 7.2.1.6: Stainless-Steel 316L specimen a) graphite loop b) top and bottom internal channel measurements after SPS c) full cross-section view.

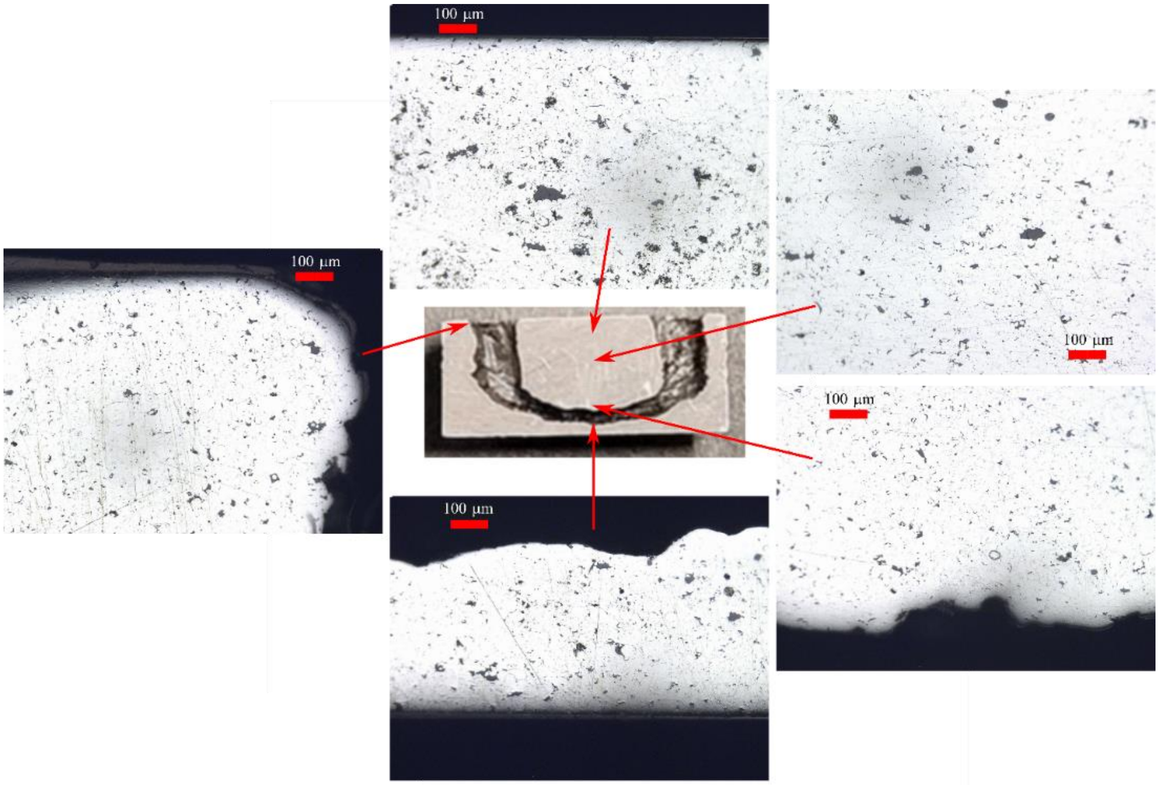

Figure 7.2.1.7: Micrographs of the Stainless-steel 316L components in the different areas.

Figure 7.2.1.7 presents the microstructure of the component after polishing in different areas of the sample. These images show how the density is homogeneous in the different areas of the component. Although the outer geometries shown for both the HAP and stainless-steel samples are discs, changing the outer geometry is possible via the printed graphite mold. As can be seen in Figure 7.2.1.5 of the tooth geometry, the graphite mold walls can be designed to be any geometry. The geometry of the sacrificial mold dictates not only the internal architecture but the external architecture of the samples as well to attain a variety of final geometries.

7.2.2 SPS Simulation

The densification curves for each material were obtained to determine the densification reached during cold compaction (graphite) and sintering (alumina, HAP and stainless steel) and are shown in Figure 7.2.2.1. Using the procedures described in section 6.1, the sintering and cold compaction parameters for the different materials were determined (Table 7.2.2.1)

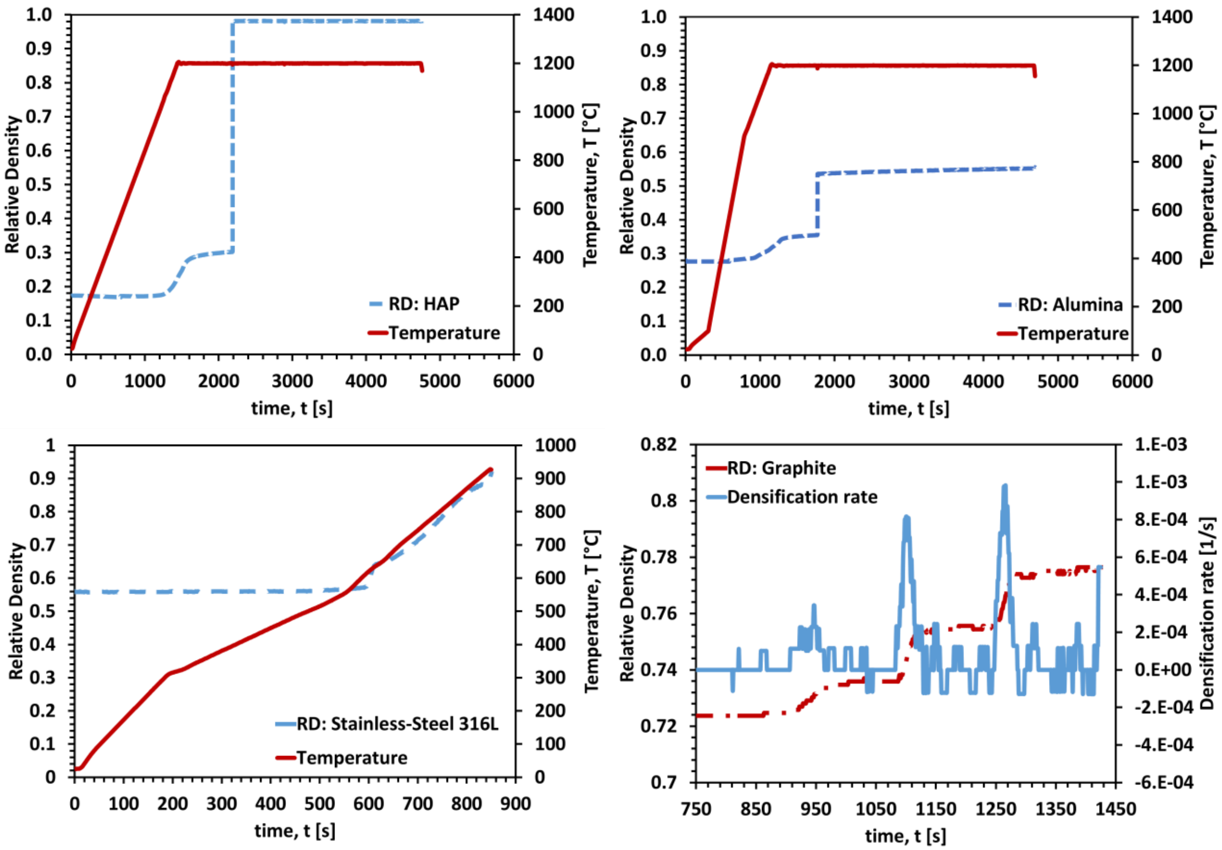

Figure 7.2.2.1: Densification curve for HAP, alumina and stainless-steel 316L powders and densification rate for graphite powder.

Table 7.2.2.1: Sintering and cold compaction parameters.

Material	**A [Pa s]**	**Q [kJ/K mol]**	**m**	**σ_y [MPa]**
Alumina	0.0011	172	1	--
HAP	$5.45 \cdot 10^{-4}$	114	1	--
Stainless-Steel 316L	$1.06 \cdot 10^{-4}$	65.3	1	--
Graphite	--	--	~0	60

The model's results for the HAP 4-channel component are presented in Figure 7.2.2.2. It is possible to observe the different densification levels reached by the three materials that compose the initial assembly (graphite, alumina and HAP). The external ring made from alumina reached a final relative density of around 70%, meanwhile the graphite mold was compacted up to 80-85%; therefore, these sacrificial parts were easily removed from the final component which reached full density.

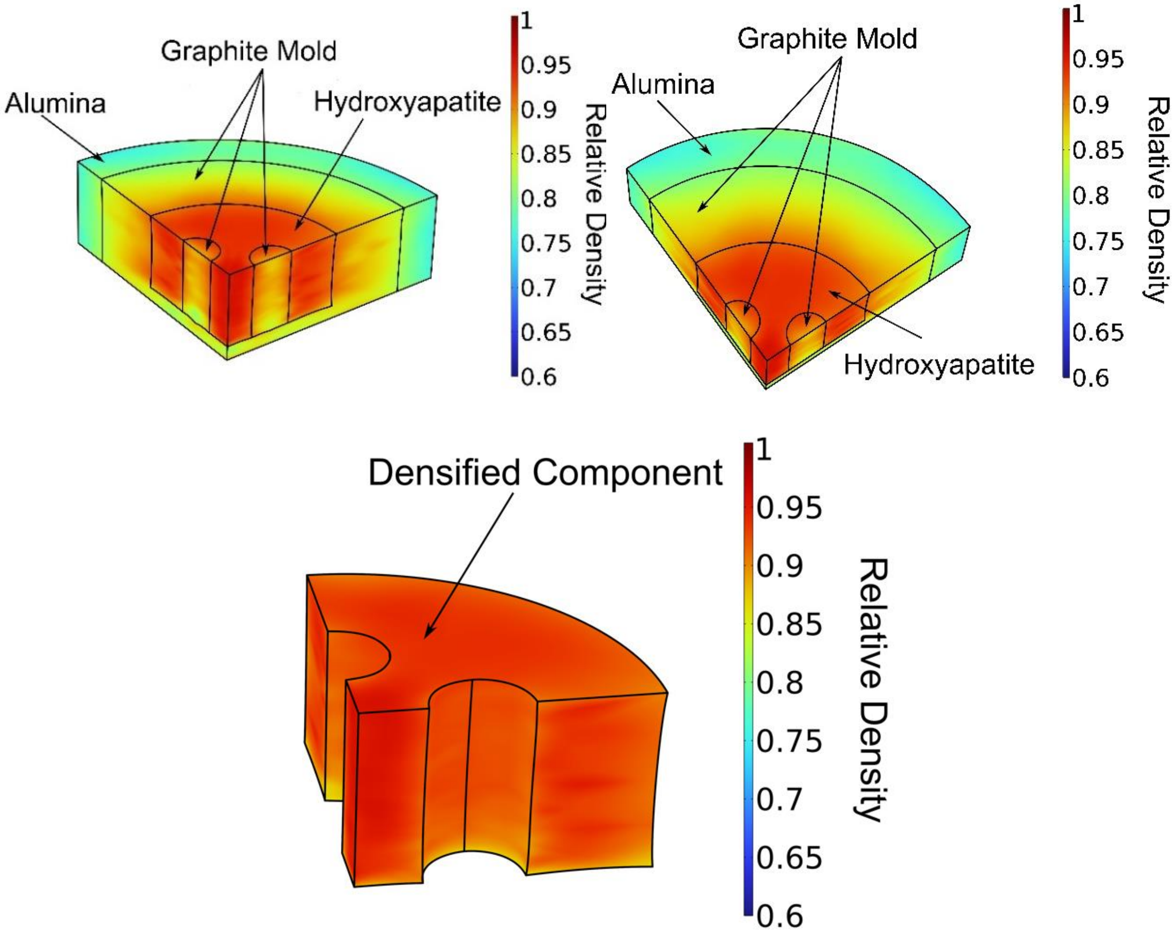

Figure 7.2.2.2: FEM model results of the 4 channel HAP component.

Table 7.2.2.2: Comparison between experimental and model HAP specimen's dimension.

	Height [mm]	Diameter [mm]	Channel diameter [mm]
Experimental	4.54	15.00	2.30
Model	4.74	14.98	2.63
Δ	0.20	0.02	0.33

The comparison of the sintered component and model dimensions are reported in Table 7.2.2.2. The comparison between the dimensions of the different geometrical features measured in the real and in the "virtual" component show good agreement with only small differences that can be derived from experimental uncertainty. Some of this uncertainty can be derived from the dimensional precision of the printed mold which was affected by the resolution of the solvent jetting process.

In addition to predicting the deformation of the final part using this method, this model and simulation can be used to predict the initial part geometry necessary to achieve the desired final part .As can be observed in Figure 7.2.2.2, there is wasting effect in the walls of the 4-channel component. This was not a desired geometrical result, in fact, a straight wall was preferred for the outside geometry. To determine what the initial geometry should be in order to achieve the straight walls, the model was used to run virtual experiments. Figure 7.2.2.3 shows how when starting with a straight inner wall, the final sample will experience some waisting after the SPS cycle as was also observed in experiments (left side). More importantly, the right side of the figure shows how when starting with a slightly curved inner wall, a final straight wall can be achieved. It is difficult to photograph the initial curve printed on the sacrificial mold because it is so small. The initial arc (barreled away from the central axis) was only displaced 0.3 mm from the initial straight wall coordinate.

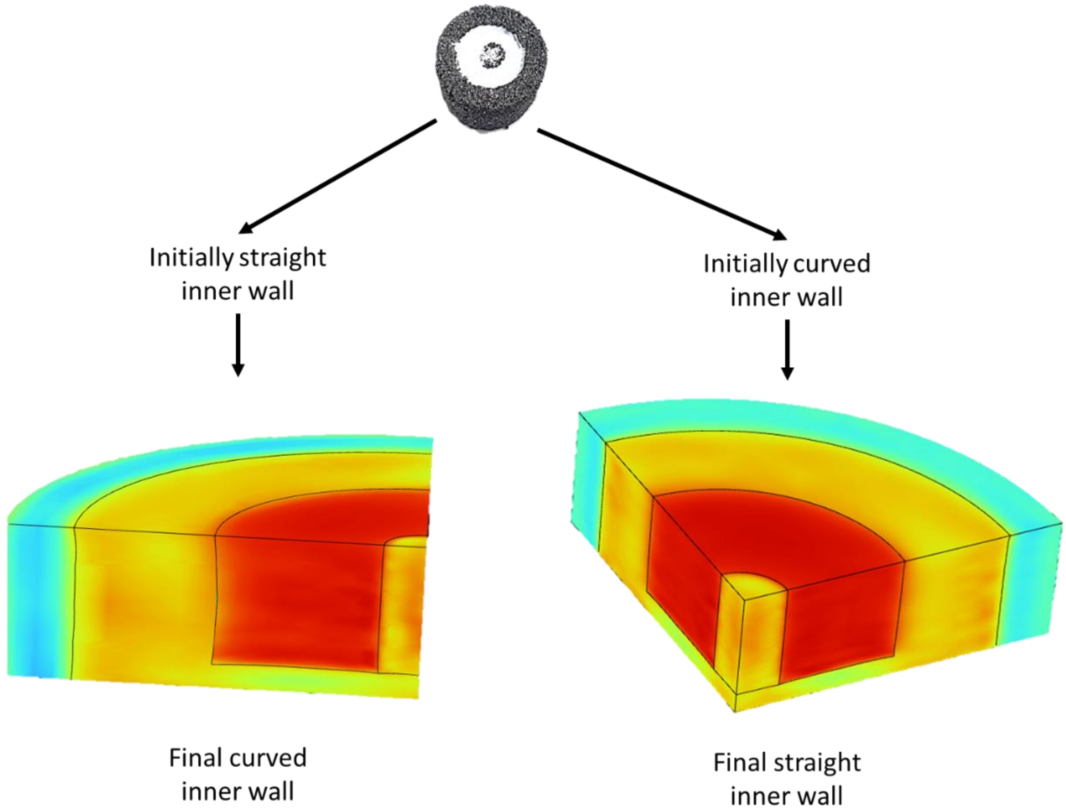

Figure 7.2.2.3: Utilization of model to predict initial curve necssary for the inner wall of printed mold to achieve a straight inner wall after SPS.

Similarly, the model was run for the stainless-steel component with the internal loop channel feature. The model results are showed in Figure 7.2.2.4. Also, for this case, it is possible to appreciate the ability of the model to predict the varying levels of densification of the different materials used in this process.

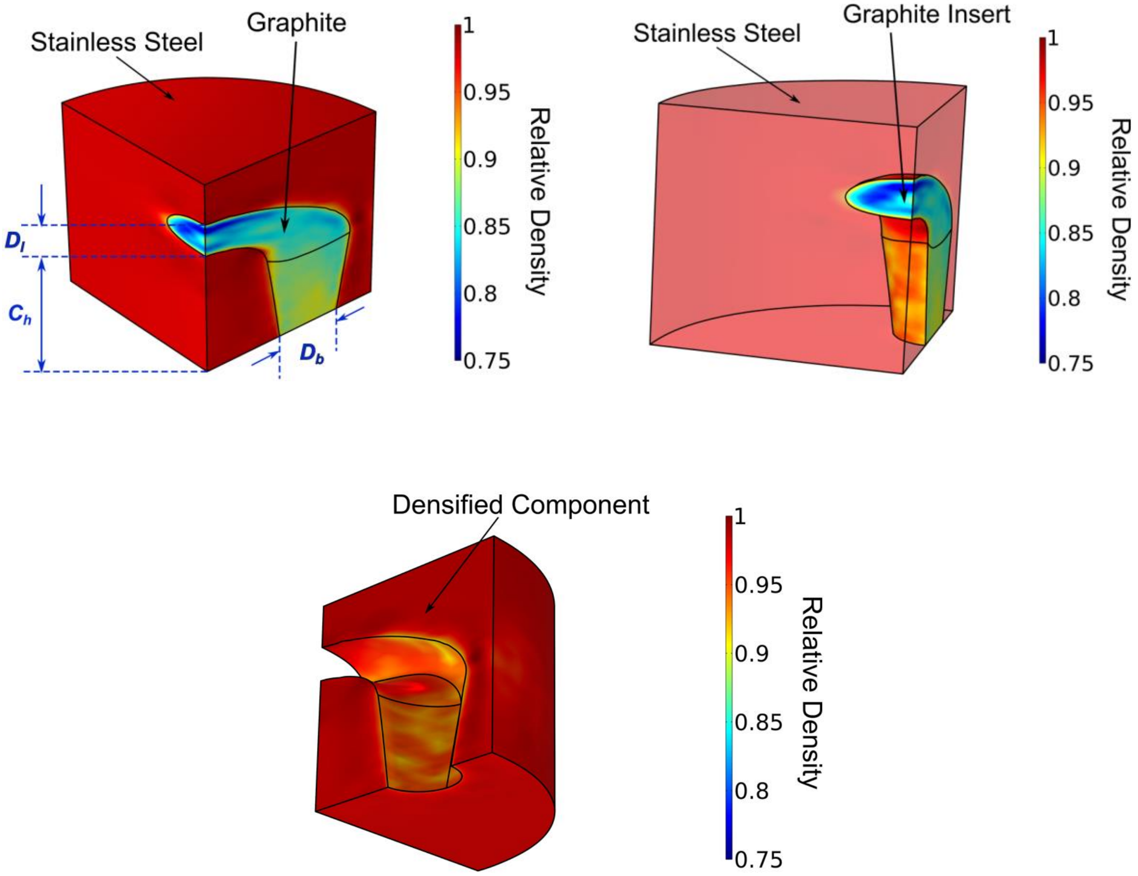

Figure 7.2.2.4: FEM model results of the stainless-steel 316L component.

For the stainless-steel part, the model predicted a final relative density of 98% which was in agreement with the experimental results. Moreover, in Table 7.2.2.3, the comparison between the experimental and the model results for the stainless-steel component are reported. For both the HAP and the stainless-steel components, the model was capable of predicting the final dimension of the internal channel. A similar study as was illustrated in Figure 7.2.2.3 can be performed for the stainless-steel components to achieve a desired geometry for the channel. For example, if the desired geometry includes a fully circular channel, then the initial inner channel geometry would be slightly elliptical in the z direction.

Table 7.2.2.3: Comparison between experimental and model SS316L specimen's dimensions.

	Bottom Diameter (D_b) [mm]	Loop Diameter (D_l) [mm]	Channel height (C_h) [mm]
Experimental	2.56	0.8	5.18
Model	2.64	1.17	4.45
Δ	0.08	0.37	0.73

7.3 Discussion

The proposed approach opens the potential of producing near net shape ceramic and metallic parts in a streamlined process which takes advantage of the ability to design and produce custom complex shapes using the SJ printing method in conjunction with the ability to use SPS to consolidate materials efficiently. The method to SPS a 3D printed graphite mold was validated by producing both a 4-channel HAP ceramic disc and a U-shaped channel stainless steel metallic part. A finite element model was created to simulate the densification behavior of the sample in the graphite mold during sintering. The density and shape of the final sintered samples were accurately predicted by the simulation and can be used in the design of the mold for various materials and components.

This work demonstrates the significant potential that advanced Spark Plasma Sintering methods have in creating complex shapes with a custom internal architecture. Traditionally, SPS was limited by the die geometry where one tooling set was dedicated to the production of one sample shape. Theoretically, any internal and external shape can be printed using the presented method; however, additional experiments need to be conducted to assess the realistic geometric limits. The U-shaped metallic part illustrates the freedom of having features perpendicular to the direction of the load - a common concern in pressure assisted sintering. Furthermore, the 4-channel ceramic part produced in this work addresses the multiple feature ability of this method by having more than one channel. This process can be extended to most materials given that the powder of interest does not need to go through any preparation prior to sintering. Using the developed modeling code, a proper sintering cycle can be determined for each material and geometry, dramatically improving the productivity of the SPS technology.

Additionally, using the developed model, the initial geometry necessary for the printing of the sacrificial mold can be determined. This is particularly important to avoid time consuming experimental runs. From an industrial perspective, this is highly important in actually implementing this technique in industrial applications.

7.4 Chapter Summary

A novel method of producing complex ceramic and metallic parts with designed internal channels was developed. The method utilizes a combination of the additive manufacturing technique of solvent jetting and spark plasma sintering (SPS.) The developed manufacturing approach brings benefits in producing complex shape with internal channels. Along with geometric customization of the 3D printed mold, a major advantage of this method is the removal of the need for a long debinding process, usually necessary with other 3D printing methods, by using the SPS. Furthermore, because the graphite does not sinter, it is easily removed from the internal channels and cavities via sand blasting. Any remaining graphite can be decomposed in air via annealing. Additionally, sintering time is drastically reduced using SPS which leads to high density with limited grain growth. High density ceramic and metallic complex parts with internal channels were successfully produced with close to theoretical densities. The conducted studies include the development of a model that can predict the evolution and/or distortions of the complex-shaped powder assembly during the sintering process. The model is based on the continuum theory of sintering formulations embedded in a finite element code.

Chapter Acknowledgements

Chapter 7, in part, is a reprint of the material as it appears in Journal of European Ceramic Society, 2023. Torresani, Elisa; Carrillo, Maricruz. Elsevier. The dissertation author was the primary investigator and co-author of this paper.

8 CUSTOMER DISCOVERY AND MARKET FIT RESEARCH ON 3D PRINTED LOAD BEARING CERAMIC SCAFFOLDS

During my third and fourth year of this doctoral program, I applied and received the U.S. National Science Foundation's Innovation Corps (I-Corps™) grant to conduct customer and market discovery research. The I-Corps curriculum is a comprehensive, hands-on entrepreneurial education course that helps turn idea into impact. The NSF-funded projects that are prepared to transition toward commercialization will reap faster economic and societal advantages thanks to the intense training provided by this program for scientists and engineers. This was a new experience for me (Entrepreneurial Lead), Elisa Torresani (Technical Lead) and Eugene Olevsky (Principal Investigator) of having a PhD student prepare a proposal, submit a proposal and be granted an NSF I-Corps grant.

The major goal of this project was to evaluate the marketability and ease of integration of a technology developed at San Diego State's Powder Technology Lab (PTL). The technology is a method of producing ceramic samples via 3D printing to be used as bone grafts and implants which are custom made for the injury site and patient characteristics. This method is described in detail in Chapter 5. The mechanical and physical properties achieved in the bone scaffolds produced had not been previously achieved or presented in industry. The team believes this is a technology that could be integrated into the current standard of care in operating rooms across the country and eventually the world. However, even if the technology is there, it does not mean it can be easily implemented in the field which is why I applied to this grant.

8.1 Research Methodology

Over 200 customer discovery interviews were conducted by the team along with successful completion of all didactic portions of the program at Kick-off and Lessons learned events. The program was divided into two parts: I-Corps Summer Sprint and I-Corps National Program. The sprint program took place at San Diego State University and was focused on the introduction to a Business Model Canvas (BMC). An example of our BMC is shown in Figure 8.1.1. The national program was designed to fully confirm whether the research idea was needed, wanted and fitting to the current state of our target industry. Basically, completing and understanding this BMC for our potential start-up through the interviews and lessons was the ultimate goal for this NSF project.

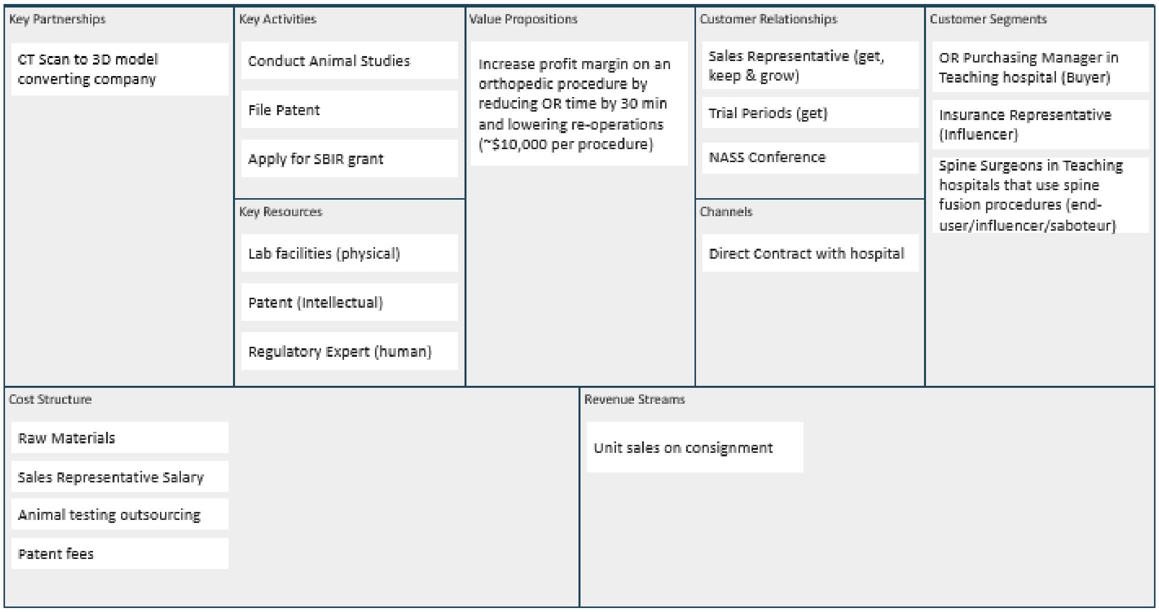

Key Partnerships
- CT Scan to 3D model converting company

Key Activities
- Conduct Animal Studies
- File Patent
- Apply for SBIR grant

Key Resources
- Lab facilities (physical)
- Patent (Intellectual)
- Regulatory Expert (human)

Value Propositions
- Increase profit margin on an orthopedic procedure by reducing OR time by 30 min and lowering re-operations (~$10,000 per procedure)

Customer Relationships
- Sales Representative (get, keep & grow)
- Trial Periods (get)
- NASS Conference

Channels
- Direct Contract with hospital

Customer Segments
- OR Purchasing Manager in Teaching hospital (Buyer)
- Insurance Representative (Influencer)
- Spine Surgeons in Teaching hospitals that use spine fusion procedures (end-user/influencer/saboteur)

Cost Structure
- Raw Materials
- Sales Representative Salary
- Animal testing outsourcing
- Patent fees

Revenue Streams
- Unit sales on consignment

Figure 8.1.1: Business Model Canvas (BMC) used for NSF I-Corps grant.

The specific objectives for the NSF I-Corps sprint summer program (4 weeks):

1. Attend 40 hours of lectures with the teaching team.
2. Provide a written report of progress weekly.
3. Conduct 30 interviews with industry experts.
4. Identify your target customer.
5. Determine at least 3 value propositions for that customer.
6. Create a Lessons Learned video and presentation to conclude the program.

This part of the program was done solely in person in San Diego, California. Lessons and customer discovery interviews were done in person and over the phone. The team was connected with a mentor for this program, our industry mentor was Dominic Tong, M.D. who had experience in the medical industry both as a physician and as an investor. Dr. Tong was integral in attaining enough interviews during the short 4-week period. The team also was required to attend several entrepreneurship events around the San Diego County where we built the network for more interview opportunities.

Specific objectives for the national NSF I-Corps program (18 months):

1) Complete all lectures with the teaching team.
2) Conduct at least 100 customer discovery interviews.
3) Determine if there is demand for the technology in current market.
4) Determine if the technology is financially viable in current market.
5) Determine if there is product market fit.
6) Submit final report to NSF.

The kickoff event, didactic lectures and lessons learned event for this portion of the program was virtual due to the COVID-19 pandemic. All initial 100 interviews were also virtual, mostly through Zoom and over the phone. However, some of the interviews were done in person. Additionally, a no-cost extension was submitted for this project. The budget of $50,000 was not spent within the time period, again, due to the pandemic. The most common expenditures are commonly travel, food, hotel and conference fee expenses and given that everyone was on lock down, the team refrained from all those activities. The budget was successfully spent the following year.

8.2 Results

Due to the extension, the number of customer discovery interviews was higher than the requirement. At the end of the program, the team conducted a total of 231 interviews with industry experts. People interviewed included: orthopedic surgeons, FDA consultants, hospital managers, nurses, insurance companies, CEOs, medical device sales representatives and patients. The initial customer list grew from orthopedic surgeon to over 8 different stake holders to include medical device sales representatives, which we had no idea was such an integral part of the bone repair and implant workflow.

The team learned a lot about how to conduct a market research study. The fundamentals were learned on how to identify key stakeholders, important value propositions and critical questions to lead us into a definite conclusion on our technology’s potential. More than 200 customer discovery interviews allowed us to gauge the current status of the market and how our product fits into it. Through the knowledge gained in the didactic portion of the program and the insight we gained from all interviewees, the team determined there is a high demand and need for this technology in the market.

The current gold standard is autologous or allographic bone which is limited in size, shape, and availability. This was confirmed by most surgeons the team spoke to and the bone scaffold companies that have heard of the demand for better solutions from their customers. Additionally, there is potential for implementation in “niche” surgery types. For example, pediatric surgery. One pediatric surgeon from Rady’s Children’s Hospital stated that at times, he must cut the standard implants in the operating room to fit his small patients.

Although there are many metallic implants being used in surgery today, there are no ceramic components being printed and used. When asked, most stakeholders mentioned ceramic materials would be ideal however, manufacturing of ceramics has been too difficult and so there has been no success. Importantly, this confirmation allowed me to narrow down my research on what matters to people performing these operations every day. Surgeons mentioned several reasons why metallic implants need to be improved to include:

- Corrosion and Wear: Metallic implants are susceptible to corrosion and wear over time, which can lead to implant failure and the release of metal ions into the surrounding tissues. This can cause inflammation, tissue damage, and other complications.
- Allergic Reactions: Some patients may develop allergic reactions to the metal in the implants, which can cause pain, swelling, and other symptoms. This is more common in patients with metal allergies or a history of metal sensitivity.
- Infection: Metallic implants can also be prone to infection, which can lead to implant failure and the need for revision surgery. The risk of infection is higher in patients with compromised immune systems or other risk factors.

- Stress Shielding: Metallic implants can cause stress shielding, which is the transfer of stress away from the bone to the implant. This can lead to bone loss and weakening of the bone around the implant.
- Limited Lifespan: Metallic implants have a limited lifespan and may need to be replaced over time. Revision surgery can be more complicated and riskier than the initial surgery and can also be expensive.

It was also evident that orthopedic surgeons are constantly working to develop new materials and techniques to address these issues and improve the outcomes for patients with joint replacements and other orthopedic implants. The team determined that the technology is financially viable by using Centers for Medicare & Medicaid Services (CMS) Reimbursement codes to our advantage. Insurance plays a bigger role in the medical industry than was expected but it can be used as a positive tool. Furthermore, the implementation of our technology would not require significant infrastructure changes or workflow disruption. This is important for the hospital managers who are usually concerned with increasing the cost of running the hospital and operating room. Through the interviews with Purchasing Managers of hospitals, the team was able to conclude that our technology would be added as an available option for implants. Therefore, our product would simply need a spot on the shelf that is already existing.

When speaking to our “competitors” in the industry, the team discovered the existence of an NTAP classification for customizable implants which gives the technology an edge because the reimbursement is much higher than products being used today. Hospitals usually favor higher-paid reimbursement codes because they get paid per surgery, regardless of the implant that is used. Therefore, if the implant gives more money to the hospital, the hospital receives more money at the end. Based on the details provided above, the team proved there is product market fit.

8.3 Discussion

It is important to include the work conducted under this grant given that it guided my research work in a way a theoretical approach could not. I have read countless articles and books on bioceramics, 3D printing of ceramics, sintering and sintering models, however, in literature, one cannot know and understand how the technologies being developed will help the end patient without talking to those patients. Furthermore, it is often the case where a technology is developed, the science is phenomenal, but it does not fit in the market and renders useless. A great example given during one of the lessons was that of the Segway. The two-wheeled, self-balancing battery electric vehicle invented by Dean Kamen. It was launched in 2001 and was thought to become the next big thing in transportation, completely revolutionizing the way we move around. Yet it failed to gain significant market acceptance and is now something of a curiosity. The product is very clever and the engineering work that went into it to make it work is impressive. However, they were making a product instead of a solution. They did not speak to their future customers and did not listen to the market. Many researchers fall into this trap of developing groundbreaking research that cannot be transformed into a solution.

One major finding happened during a conference in Boston. While walking around the exhibition hall, the EL met people from a company called Carlsmed. This company has a very similar technology and disclosed that they were able to get a CMS code called NTAP which completely changed our strategy. NTAP stands for "New Technology Add-on Payment," which is a program implemented by the Centers for Medicare and Medicaid Services (CMS) in the United States. The program provides additional reimbursement to hospitals for the use of certain new medical technologies that are deemed to be clinically effective and have demonstrated substantial clinical improvement over existing treatments. Under the NTAP program, CMS assigns a unique HCPCS (Healthcare Common Procedure Coding System) code to each qualifying new technology. This code is used by hospitals to report the use of the technology on their claims for reimbursement. The additional payment amount for a given NTAP-eligible technology is calculated based on the estimated costs associated with the technology and the number of Medicare beneficiaries who receive the technology. The additional payment is made in addition to the standard Medicare payment for the associated procedure. The NTAP program is intended to encourage the adoption of new, clinically effective technologies by hospitals, and to ensure that Medicare beneficiaries have access to these technologies. It is important to note that not all new technologies are eligible for NTAP, and that eligibility criteria can vary from year to year. Introduced in 2001, the CMS NTAP program was created by Congress to help close this gap and support timely access to innovative therapies for the Medicare population. This additional payment makes a technology like ours very marketable to hospitals and surgeons.

Additionally, the team now has the knowledge to use the same method that was learned during the program for all future customer discovery. Over 250 network connections were made, and all have agreed to another interview if the team needs more information or clarification. We did not just figure out the plan for this technology, we have the tools to evaluate all future technologies that are developed in our laboratory in a professional and efficient manner.

9 OVERALL CONCLUSIONS

9.1 Achieved Goals

The research conducted resulted in various methods combining additive manufacturing and sintering techniques to produce porous scaffolds with complex shapes and load bearing capabilities. We demonstrated that it is possible to use powder-based 3D printing techniques to fabricate near net shape components with properties resembling those of natural bone. We were able to fabricate a high-strength yet porous ceramic component using solvent jetting and free sintering by granulating the printing powder, enabling the use of nano-sized powder particles. We developed a technique where we use solvent jetting indirectly to produce a sacrificial mold that self-destructs during sintering. We designed a way to produce complex shaped components with internal architecture via solvent jetting and spark plasma sintering which is usually not possible due to the application of pressure. And finally, predictive tools and models were developed to fully utilize the advantages of additive manufacturing and design our initial geometries based on the desired final properties and shapes.

Prior to our work, the 3D printing of nano-sized powder using binder or solvent jetting was impossible. It can be seen in literature that the recommended size for printing using powder-based methods, the ideal particle size is in the range of 40-120 micron. This is due to the flowability required for printing. However, this usually results in low densities, especially in ceramics. By using our innovative granulated powder approach, we were able to print nano-powders resulting in a more sinterable component.

The use of binder in printed components is often seen as an impediment to the successful fabrication of fully dense parts. We decided to use this flaw to our advantage when developing the Additive Manufacturing via Subtractive Sintering method. Due to the presence of binder, and the application of pressure, this mold essentially removes itself from the final sintered part during sintering. This significantly reduces the processing time because it removes the awfully time-consuming debinding step. Furthermore, since the AMSS method uses free sintering versus other more advanced sintering techniques, it opens new opportunities for mass production.

Applying pressure is a great tactic used in technologies like SPS and hot pressing to decrease porosity in components and, therefore, help in sintering. However, because of this application of load, components produced using pressure are traditionally limited to simple shapes with no internal cavities. In this work, we developed a method where an object with internal channels and can be fabricated. Because we are printing the sacrificial mold, any shape can be printed for the outside of the mold when the axial deformation due to the pressure is taken into account in the design of that mold. Additionally, a predictive model was developed using the continuum theory of sintering to plan for the deformation that occurs during the pressing and sintering process.

9.2 Engineering & Science Novelty of the Obtained Research Results

(i) The powder preparation method developed enabled the use of nano-sized particles via powder-based printing methods. Using smaller powder sizes increases sinterability and results in smaller grain sizes which in turn leads to a higher mechanical strength.

(ii) The Additive Manufacturing via Subtractive Sintering method developed in this work resulted fully dense ceramic components with complex shapes. This had never been possible with the printing of powders using powder-based methods. Additionally, using the binder to our advantage in the self-destruction of the mold, eliminated the need for long debinding times.

(iii) For the first time, a complex shaped component with curved or multiple internal channels was fabricated using Spark Plasma Sintering (SPS). This is especially impressive given that pressure assisted sintering is traditionally limited to simple cylindrical shapes.

  a. Additionally, it was found that using SPS increases the biocompatibility of the HAP component when compared to parts produced via hot pressing, this is particularly important for orthopedic applications.

(iv) Remarkably, product market fit was found for the technology developed in chapter 4. Using an NSF grant, customer discovery confirmed that the technologies being developed were in demand in industry.

  a. Orthopedic surgeons are looking for innovative solutions using bioceramics.
  b. Hospitals would be able to add our technology to their implant selection.
  c. Surgeons and biomedical engineers agree that custom made load-bearing implants would be beneficial for patient recovery.

9.3 Summary of Research Progress

A flowchart that lists the work completed in relation to the identified study goals and tasks in Figure 2.3.1 is given in Figure 9.3.1. Although the initial flow chart did not include an FEM model for all three techniques developed, the final chart indicates the completion of the predictive model for all. Additionally, the initial tasks and objectives did not include the NSF I-

Corps program that resulted in being a confirmation of the need for the research conducted in this work.

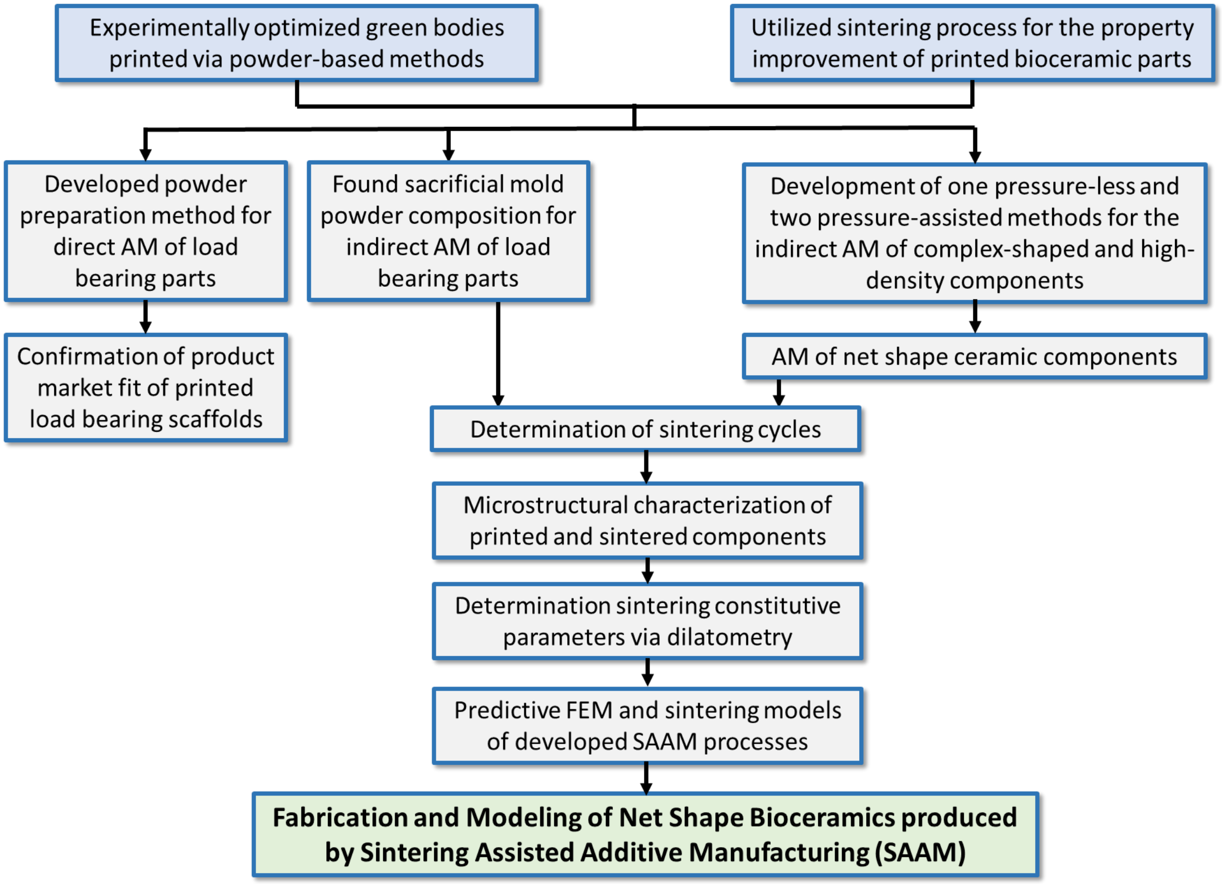

Figure 9.3.1: Summary of conducted work.

In the future, more research needs to be done on the cell viability and host integration for scaffolds fabricated using the developed SAAM methods. The biological response of the produced scaffolds was outside of the scope of this work. However, only biocompatible materials were used and produced with properties proven to enhance osseointegration, vascularization and healing modalities. Further research needs to also be done on the geometrical limits of each method. For the nano-powder printing (chapter 4) for example, geometries with over hangs or bigger dimensions were not printed and might pose problems. For the AMSS process (chapter 5), the limitation on internal channels possible with this technique is not fully understood. And lastly, the sacrificial mold method used in conjunction with Spark Plasma Sintering (SPS) needs to be expanded to include multiple parts and or more complex outer geometries with multiple channels.

Overall, the advancements made in the science of 3D printing bioceramics during this doctoral research were significant. The proper implementation of this fundamental research on industrial technologies has the potential to revolutionize the orthopedic implant industry. The demand from surgeons and patients for innovative solutions exists. And most importantly, if the use of bioceramics (particularly the mineral that makes up your bones- hydroxyapatite) becomes the gold standard of care for bone repair, the industry will be moving towards using materials that naturally were intended to be used for skeletal repair and reconstruction.

REFERENCES

[1] R. R. Pelker and G. E. Friedlaender, “Biomechanical aspects of bone autografts and allografts,” *Orthop. Clin. North Am.*, vol. 18, no. 2, pp. 235–239, 1987.

[2] A. Paré, *The workes of that famous chirurgion Ambrose Parey*. Richard Cotes, and Willi: Du-gard, and are to be sold by John Clarke, 1972.

[3] H. T. Aro and A. J. Aho, “Clinical use of bone allografts,” *Ann. Med.*, vol. 25, no. 4, pp. 403–412, 1993.

[4] J. Hunter, *The Natural History of the Human Teeth: Explaining Their Structure, Use, Formation, Growth, and Diseases. Illustrated with Copper-plates*, vol. 2. J. johnson, 1778.

[5] D. N. Bracey *et al.*, “A decellularized porcine xenograft-derived bone scaffold for clinical use as a bone graft substitute: a critical evaluation of processing and structure,” *J. Funct. Biomater.*, vol. 9, no. 3, p. 45, 2018.

[6] R. Li *et al.*, “Notes from the Field: Tuberculosis Outbreak Linked to a Contaminated Bone Graft Product Used in Spinal Surgery - Delaware, March-June 2021,” *MMWR. Morb. Mortal. Wkly. Rep.*, vol. 70, pp. 1261–1263, Sep. 2021, doi: 10.15585/mmwr.mm7036a4.

[7] L. Lu, B. L. Currier, and M. J. Yaszemski, “Synthetic bone substitutes,” *Curr. Opin. Orthop.*, vol. 11, no. 5, pp. 383–390, 2000.

[8] M.-P. Ginebra, T. Traykova, and J. A. Planell, “Calcium phosphate cements as bone drug delivery systems: a review,” *J. Control. release*, vol. 113, no. 2, pp. 102–110, 2006.

[9] W. Jin and P. K. Chu, “Orthopedic implants,” *Encycl. Biomed. Eng.*, vol. 1, p. 3, 2019.

[10] J. Fischer, “Mechanical, thermal, and chemical analyses of the binary system Au-Ti in the development of a dental alloy,” *J. Biomed. Mater. Res.*, vol. 52, no. 4, pp. 678–686, Dec. 2000, doi: https://doi.org/10.1002/1097-4636(20001215)52:4<678::AID-JBM12>3.0.CO;2-P.

[11] D. C. Rodrigues, R. M. Urban, J. J. Jacobs, and J. L. Gilbert, “In vivo severe corrosion and hydrogen embrittlement of retrieved modular body titanium alloy hip-implants,” *J. Biomed. Mater. Res. Part B Appl. Biomater.*, vol. 88B, no. 1, pp. 206–219, Jan. 2009, doi: https://doi.org/10.1002/jbm.b.31171.

[12] S. Franz, S. Rammelt, D. Scharnweber, and J. C. Simon, “Immune responses to implants – A review of the implications for the design of immunomodulatory biomaterials,” *Biomaterials*, vol. 32, no. 28, pp. 6692–6709, 2011, doi: https://doi.org/10.1016/j.biomaterials.2011.05.078.

[13] G. Wang, Y. Wan, T. Wang, and Z. Liu, “Corrosion Behavior of Titanium Implant with different Surface Morphologies,” *Procedia Manuf.*, vol. 10, pp. 363–370, 2017, doi: https://doi.org/10.1016/j.promfg.2017.07.006.

[14] A. Asserghine, D. Filotás, L. Nagy, R. M. Souto, and G. Nagy, “Do titanium biomaterials get immediately and entirely repassivated? A perspective,” *npj Mater. Degrad.*, vol. 6, no. 1, p. 57, 2022, doi: 10.1038/s41529-022-00270-0.

[15] A. H. Glassman, J. D. Bobyn, and M. Tanzer, “New Femoral Designs: Do They Influence Stress Shielding?,” *Clin. Orthop. Relat. Res.*, vol. 453, 2006, [Online]. Available: https://journals.lww.com/clinorthop/Fulltext/2006/12000/New_Femoral_Designs__Do_They_Influence_Stress.12.aspx.

[16] A. A. Al-Tamimi, P. R. A. Fernandes, C. Peach, G. Cooper, C. Diver, and P. J. Bartolo, “Metallic bone fixation implants: a novel design approach for reducing the stress shielding phenomenon,” *Virtual Phys. Prototyp.*, vol. 12, no. 2, pp. 141–151, Apr. 2017, doi: 10.1080/17452759.2017.1307769.

[17] M. Niinomi and M. Nakai, “Titanium-Based Biomaterials for Preventing Stress Shielding between Implant Devices and Bone,” *Int. J. Biomater.*, vol. 2011, p. 836587, 2011, doi: 10.1155/2011/836587.

[18] J. J. Klawitter and S. F. Hulbert, “Application of porous ceramics for the attachment of load bearing internal orthopedic applications,” *J. Biomed. Mater. Res.*, vol. 5, no. 6, pp. 161–229, Nov. 1971, doi: https://doi.org/10.1002/jbm.820050613.

[19] C. Rey, C. Combes, C. Drouet, and M. J. Glimcher, “Bone mineral: update on chemical composition and structure,” *Osteoporos. Int.*, vol. 20, pp. 1013–1021, 2009.

[20] R. Z. LeGeros and J. P. LeGeros, “Calcium phosphate bioceramics: past, present and future,” in *Key Engineering Materials*, 2003, vol. 240, pp. 3–10.

[21] R. Z. LeGeros, “Biodegradation and bioresorption of calcium phosphate ceramics,” *Clin. Mater.*, vol. 14, no. 1, pp. 65–88, 1993.

[22] R. Z. LeGeros, “Properties of osteoconductive biomaterials: calcium phosphates.,” *Clin. Orthop. Relat. Res.*, vol. 395, pp. 81–98, 2002.

[23] M. Vallet-Regí, “Revisiting ceramics for medical applications,” *Dalt. Trans.*, no. 44, pp. 5211–5220, 2006.

[24] S. V Dorozhkin, “Bioceramics of calcium orthophosphates,” *Biomaterials*, vol. 31, no. 7, pp. 1465–1485, 2010, doi: https://doi.org/10.1016/j.biomaterials.2009.11.050.

[25] S. Hoover, S. Tarafder, A. Bandyopadhyay, and S. Bose, “Silver doped resorbable tricalcium phosphate scaffolds for bone graft applications,” *Mater. Sci. Eng. C*, vol. 79, pp. 763–769, 2017, doi: https://doi.org/10.1016/j.msec.2017.04.132.

[26] R. Horowitz, M. Leventis, M. Rohrer, and H. Prasad, “Bone grafting: History, rationale, and selection of materials and techniques,” *Compend. Contin. Educ. Dent.*, vol. 35, pp. 1-6;quiz7, Nov. 2014.

[27] M. A. Fernandez-Yague, S. A. Abbah, L. McNamara, D. I. Zeugolis, A. Pandit, and M. J. Biggs, “Biomimetic approaches in bone tissue engineering: Integrating biological and physicomechanical strategies,” *Adv. Drug Deliv. Rev.*, vol. 84, pp. 1–29, 2015.

[28] X. Wang *et al.*, “Engineering biological tissues from the bottom-up: Recent advances and future prospects,” *Micromachines*, vol. 13, no. 1, p. 75, 2022.

[29] E. Helgeland, S. Shanbhag, T. O. Pedersen, K. Mustafa, and A. Rosen, “Scaffold-based temporomandibular joint tissue regeneration in experimental animal models: a systematic review,” *Tissue Eng. Part B Rev.*, vol. 24, no. 4, pp. 300–316, 2018.

[30] H. Jodati, B. Yılmaz, and Z. Evis, “A review of bioceramic porous scaffolds for hard tissue applications: Effects of structural features,” *Ceram. Int.*, vol. 46, no. 10, Part B, pp. 15725–15739, 2020, doi: https://doi.org/10.1016/j.ceramint.2020.03.192.

[31] H. Cao and N. Kuboyama, “A biodegradable porous composite scaffold of PGA/β-TCP for bone tissue engineering,” *Bone*, vol. 46, no. 2, pp. 386–395, 2010, doi: https://doi.org/10.1016/j.bone.2009.09.031.

[32] S. I. Roohani-Esfahani *et al.*, “Unique microstructural design of ceramic scaffolds for bone regeneration under load,” *Acta Biomater.*, vol. 9, no. 6, pp. 7014–7024, 2013, doi: https://doi.org/10.1016/j.actbio.2013.02.039.

[33] I. J. Gibson and M. F. Ashby, “The mechanics of three-dimensional cellular materials,” *Proc. R. Soc. London. A. Math. Phys. Sci.*, vol. 382, no. 1782, pp. 43–59, 1982.

[34] Q. Chen and G. A. Thouas, “Metallic implant biomaterials,” *Mater. Sci. Eng. R Reports*, vol. 87, pp. 1–57, 2015.

[35] A. Entezari, S.-I. Roohani-Esfahani, Z. Zhang, H. Zreiqat, C. R. Dunstan, and Q. Li, “Fracture behaviors of ceramic tissue scaffolds for load bearing applications,” *Sci. Rep.*, vol. 6, no. 1, pp. 1–10, 2016.

[36] Q. Fu, “Bioactive glass scaffolds for bone tissue engineering,” in *Biomedical, therapeutic and clinical applications of bioactive glasses*, Elsevier, 2019, pp. 417–442.

[37] S. C. Marks and P. R. Odgren, “Chapter 1 - Structure and Development of the Skeleton,” J. P. Bilezikian, L. G. Raisz, and G. A. B. T.-P. of B. B. (Second E. Rodan, Eds. San Diego: Academic Press, 2002, pp. 3–15.

[38] M. Pilia, T. Guda, and M. Appleford, “Development of composite scaffolds for load-bearing segmental bone defects,” *Biomed Res. Int.*, vol. 2013, p. 458253, 2013, doi: 10.1155/2013/458253.

[39] J. Zhang, W. Liu, V. Schnitzler, F. Tancret, and J.-M. Bouler, “Calcium phosphate cements for bone substitution: chemistry, handling and mechanical properties,” *Acta Biomater.*, vol. 10, no. 3, pp. 1035–1049, 2014.

[40] M. Mirkhalaf, A. Dao, A. Schindeler, D. G. Little, C. R. Dunstan, and H. Zreiqat, “Personalized Baghdadite scaffolds: stereolithography, mechanics and in vivo testing,” *Acta Biomater.*, vol. 132, pp. 217–226, 2021.

[41] R. G. Wells, “The role of matrix stiffness in regulating cell behavior,” *Hepatology*, vol. 47, no. 4, pp. 1394–1400, 2008.

[42] A. J. Engler, S. Sen, H. L. Sweeney, and D. E. Discher, “Matrix elasticity directs stem cell lineage specification,” *Cell*, vol. 126, no. 4, pp. 677–689, 2006.

[43] L. L. Hench and J. M. Polak, “Third-generation biomedical materials,” *Science (80-.).*, vol. 295, no. 5557, pp. 1014–1017, 2002.

[44] C. Wu *et al.*, “The effect of mesoporous bioactive glass on the physiochemical, biological and drug-release properties of poly (DL-lactide-co-glycolide) films,” *Biomaterials*, vol. 30, no. 12, pp. 2199–2208, 2009.

[45] D. D. Deligianni, N. D. Katsala, P. G. Koutsoukos, and Y. F. Missirlis, “Effect of surface roughness of hydroxyapatite on human bone marrow cell adhesion, proliferation, differentiation and detachment strength,” *Biomaterials*, vol. 22, no. 1, pp. 87–96, 2000, doi: https://doi.org/10.1016/S0142-9612(00)00174-5.

[46] E. Nasatzky, J. Gultchin, and Z. Schwartz, “[The role of surface roughness in promoting osteointegration],” *Refuat. Hapeh. Vehashinayim.*, vol. 20, no. 3, pp. 8-19,98, 2003, [Online]. Available: http://europepmc.org/abstract/MED/14515625.

[47] A. Wennerberg, “The importance of surface roughness for implant incorporation,” *Int. J. Mach. Tools Manuf.*, vol. 38, no. 5, pp. 657–662, 1998, doi: https://doi.org/10.1016/S0890-6955(97)00114-4.

[48] O. Chan *et al.*, “The effects of microporosity on osteoinduction of calcium phosphate bone graft substitute biomaterials,” *Acta Biomater.*, vol. 8, no. 7, pp. 2788–2794, 2012.

[49] P. Viswanathan *et al.*, “3D surface topology guides stem cell adhesion and differentiation,” *Biomaterials*, vol. 52, pp. 140–147, 2015.

[50] G. Khalil, S. Lorthois, M. Marcoux, P. Mansat, and P. Swider, “Wave front migration of endothelial cells in a bone-implant interface,” *J. Biomech.*, vol. 44, no. 10, pp. 1980–1986, 2011.

[51] J. R. Jones and L. L. Hench, “Regeneration of trabecular bone using porous ceramics,” *Curr. Opin. Solid State Mater. Sci.*, vol. 7, no. 4, pp. 301–307, 2003, doi: https://doi.org/10.1016/j.cossms.2003.09.012.

[52] S. J. Hollister, “Porous scaffold design for tissue engineering,” *Nat. Mater.*, vol. 4, no. 7, pp. 518–524, 2005.

[53] M. Mirkhalaf, X. Wang, A. Entezari, C. R. Dunstan, X. Jiang, and H. Zreiqat, “Redefining architectural effects in 3D printed scaffolds through rational design for optimal bone tissue regeneration,” *Appl. Mater. Today*, vol. 25, p. 101168, 2021.

[54] V. Karageorgiou and D. Kaplan, “Porosity of 3D biomaterial scaffolds and osteogenesis,” *Biomaterials*, vol. 26, no. 27, pp. 5474–5491, 2005, doi: https://doi.org/10.1016/j.biomaterials.2005.02.002.

[55] I. Denry and L. T. Kuhn, “Design and characterization of calcium phosphate ceramic scaffolds for bone tissue engineering,” *Dent. Mater.*, vol. 32, no. 1, pp. 43–53, 2016.

[56] M. Scheffler and P. Colombo, *Cellular ceramics: structure, manufacturing, properties and applications*. John Wiley & Sons, 2006.

[57] E. Liverani, G. Rogati, S. Pagani, S. Brogini, A. Fortunato, and P. Caravaggi, “Mechanical interaction between additive-manufactured metal lattice structures and bone in compression: implications for stress shielding of orthopaedic implants,” *J. Mech. Behav. Biomed. Mater.*, vol. 121, p. 104608, 2021.

[58] S. Bose and N. Sarkar, “Natural medicinal compounds in bone tissue engineering,” *Trends Biotechnol.*, vol. 38, no. 4, pp. 404–417, 2020.

[59] G. L. Koons, M. Diba, and A. G. Mikos, “Materials design for bone-tissue engineering,” *Nat. Rev. Mater.*, vol. 5, no. 8, pp. 584–603, 2020.

[60] V. Campana *et al.*, “Bone substitutes in orthopaedic surgery: from basic science to clinical practice,” *J. Mater. Sci. Mater. Med.*, vol. 25, no. 10, pp. 2445–2461, 2014, doi: 10.1007/s10856-014-5240-2.

[61] A. Heuijerjans, W. Wilson, K. Ito, and C. C. van Donkelaar, “The critical size of focal articular cartilage defects is associated with strains in the collagen fibers,” *Clin. Biomech.*, vol. 50, pp. 40–46, 2017, doi: https://doi.org/10.1016/j.clinbiomech.2017.09.015.

[62] T.-M. G. Chu, D. G. Orton, S. J. Hollister, S. E. Feinberg, and J. W. Halloran, “Mechanical and in vivo performance of hydroxyapatite implants with controlled architectures,” *Biomaterials*, vol. 23, no. 5, pp. 1283–1293, 2002, doi: https://doi.org/10.1016/S0142-9612(01)00243-5.

[63] X. Du, S. Fu, and Y. Zhu, “3D Printing of Ceramic-Based Scaffolds for Bone Tissue Engineering: An Overview,” *J. Mater. Chem. B*, vol. 6, Jun. 2018, doi: 10.1039/C8TB00677F.

[64] V. A. Dubok, “Bioceramics — Yesterday, Today, Tomorrow,” *Powder Metall. Met. Ceram.*, vol. 39, no. 7, pp. 381–394, 2000, doi: 10.1023/A:1026617607548.

[65] C. Piconi, G. Maccauro, F. Muratori, and E. Prever, “Alumina and Zirconia Ceramics in Joint Replacements,” *J. Appl. Biomater. Biomech.*, vol. 1, pp. 19–32, Jan. 2003.

[66] H. Lu *et al.*, “Current Application of Beta-Tricalcium Phosphate in Bone Repair and Its Mechanism to Regulate Osteogenesis ,” *Frontiers in Materials* , vol. 8. 2021, [Online]. Available: https://www.frontiersin.org/articles/10.3389/fmats.2021.698915.

[67] W. Suchanek and M. Yoshimura, “Processing and properties of hydroxyapatite-based biomaterials for use as hard tissue replacement implants,” *J. Mater. Res.*, vol. 13, no. 1, pp. 94–117, 1998, doi: DOI: 10.1557/JMR.1998.0015.

[68] I. Ielo, G. Calabrese, G. Luca, and S. Conoci, “Recent Advances in Hydroxyapatite-Based Biocomposites for Bone Tissue Regeneration in Orthopedics,” *Int. J. Mol. Sci.*, vol. 23, p. 9721, Aug. 2022, doi: 10.3390/ijms23179721.

[69] M. J. Webber, O. F. Khan, S. A. Sydlik, B. C. Tang, and R. Langer, “A Perspective on the Clinical Translation of Scaffolds for Tissue Engineering,” *Ann. Biomed. Eng.*, vol. 43, no. 3, pp. 641–656, 2015, doi: 10.1007/s10439-014-1104-7.

[70] J.-P. Kruth, M.-C. Leu, and T. Nakagawa, “Progress in additive manufacturing and rapid prototyping,” *Cirp Ann.*, vol. 47, no. 2, pp. 525–540, 1998.

[71] E. Sachs, M. Cima, and J. Cornie, “Three-Dimensional Printing: Rapid Tooling and Prototypes Directly from a CAD Model,” *CIRP Ann.*, vol. 39, no. 1, pp. 201–204, 1990, doi: https://doi.org/10.1016/S0007-8506(07)61035-X.

[72] A. C. F. on A. M. Technologies, A. S. T. Materials, and A. C. F. on A. M. T. S. F. 9. on Terminology, *Standard Terminology for Additive Manufacturing Technologies: ASTM F2792-12A*. ASTM International, 2012.

[73] O. Diegel, “10.02 - Additive Manufacturing: An Overview,” S. Hashmi, G. F. Batalha, C. J. Van Tyne, and B. B. T.-C. M. P. Yilbas, Eds. Oxford: Elsevier, 2014, pp. 3–18.

[74] C. W. Hull, “Apparatus for production of three-dimensional objects by stereolithography,” *United States Patent, Appl., No. 638905, Filed*, 1984.

[75] I. Campbell, O. Diegel, J. Kowen, and T. Wohlers, “Wohlers Report 2017 3D Printing and Additive Manufacturing State of the Industry: Annual Worldwide Progress Report.” Wohlers Associates, 2017.

[76] M. Shah, D. R. Patel, and S. Pande, “Additive manufacturing integrated Casting-A review,” *Mater. Today Proc.*, 2022.

[77] C. M. Cheah, C. K. Chua, C. W. Lee, C. Feng, and K. Totong, “Rapid prototyping and tooling techniques: a review of applications for rapid investment casting,” *Int. J. Adv. Manuf. Technol.*, vol. 25, pp. 308–320, 2005.

[78] K. J. Hodder and R. J. Chalaturnyk, “Bridging additive manufacturing and sand casting:

Utilizing foundry sand," *Addit. Manuf.*, vol. 28, pp. 649–660, 2019.

[79] A. Basso *et al.*, "3d printed mold for powder injection molding process," in *Proceedings of the Joint Special Interest Group meeting between euspen and ASPE Advancing Precision in Additive Manufacturing (2019) The European Society for Precision Engineering and Nanotechnology*, 2019, pp. 71–74.

[80] D. Almonti and N. Ucciardello, "Design and thermal comparison of random structures realized by indirect additive manufacturing," *Materials (Basel).*, vol. 12, no. 14, p. 2261, 2019.

[81] K. Naplocha, A. Dmitruk, P. Mayer, and J. W. Kaczmar, "Design of honeycomb structures produced by investment casting," *Arch. Foundry Eng.*, 2019.

[82] P. Sepulveda and J. G. P. Binner, "Processing of cellular ceramics by foaming and in situ polymerisation of organic monomers," *J. Eur. Ceram. Soc.*, vol. 19, no. 12, pp. 2059–2066, 1999, doi: https://doi.org/10.1016/S0955-2219(99)00024-2.

[83] I.-H. Jo, K.-H. Shin, Y.-M. Soon, Y.-H. Koh, J.-H. Lee, and H.-E. Kim, "Highly porous hydroxyapatite scaffolds with elongated pores using stretched polymeric sponges as novel template," *Mater. Lett.*, vol. 63, no. 20, pp. 1702–1704, 2009, doi: https://doi.org/10.1016/j.matlet.2009.05.017.

[84] J. C. Le Huec, T. Schaeverbeke, D. Clement, J. Faber, and A. Le Rebeller, "Influence of porosity on the mechanical resistance of hydroxyapatite ceramics under compressive stress," *Biomaterials*, vol. 16, no. 2, pp. 113–118, 1995, doi: https://doi.org/10.1016/0142-9612(95)98272-G.

[85] G. Brunello *et al.*, "Powder-based 3D printing for bone tissue engineering," *Biotechnol. Adv.*, vol. 34, no. 5, pp. 740–753, 2016, doi: https://doi.org/10.1016/j.biotechadv.2016.03.009.

[86] S. Deville, E. Saiz, and A. P. Tomsia, "Freeze casting of hydroxyapatite scaffolds for bone tissue engineering," *Biomaterials*, vol. 27, no. 32, pp. 5480–5489, 2006, doi: https://doi.org/10.1016/j.biomaterials.2006.06.028.

[87] N. Sultana and M. Wang, "PHBV/PLLA-based composite scaffolds fabricated using an emulsion freezing/freeze-drying technique for bone tissue engineering: surface modification and in vitro biological evaluation," *Biofabrication*, vol. 4, no. 1, p. 15003, 2012, doi: 10.1088/1758-5082/4/1/015003.

[88] D. W. Hutmacher, J. T. Schantz, C. X. F. Lam, K. C. Tan, and T. C. Lim, "State of the art and future directions of scaffold-based bone engineering from a biomaterials perspective," *J. Tissue Eng. Regen. Med.*, vol. 1, no. 4, pp. 245–260, 2007.

[89] C. Wang *et al.*, "3D printing of bone tissue engineering scaffolds," *Bioact. Mater.*, vol. 5, no. 1, pp. 82–91, 2020, doi: https://doi.org/10.1016/j.bioactmat.2020.01.004.

[90] C. R. M. Black, V. Goriainov, D. Gibbs, J. Kanczler, R. S. Tare, and R. O. C. Oreffo, “Bone Tissue Engineering,” *Curr. Mol. Biol. Reports*, vol. 1, no. 3, pp. 132–140, 2015, doi: 10.1007/s40610-015-0022-2.

[91] M. N. Collins, G. Ren, K. Young, S. Pina, R. L. Reis, and J. M. Oliveira, “Scaffold Fabrication Technologies and Structure/Function Properties in Bone Tissue Engineering,” *Adv. Funct. Mater.*, vol. 31, no. 21, p. 2010609, May 2021, doi: https://doi.org/10.1002/adfm.202010609.

[92] A. A. Zadpoor, “Bone tissue regeneration: the role of scaffold geometry,” *Biomater. Sci.*, vol. 3, no. 2, pp. 231–245, 2015, doi: 10.1039/C4BM00291A.

[93] M. Dang, L. Saunders, X. Niu, Y. Fan, and P. X. Ma, “Biomimetic delivery of signals for bone tissue engineering,” *Bone Res.*, vol. 6, no. 1, p. 25, 2018.

[94] R. Dimitriou, E. Jones, D. McGonagle, and P. V Giannoudis, “Bone regeneration: current concepts and future directions,” *BMC Med.*, vol. 9, no. 1, pp. 1–10, 2011.

[95] M. Laubach *et al.*, “Clinical translation of a patient-specific scaffold-guided bone regeneration concept in four cases with large long bone defects,” *J. Orthop. Transl.*, vol. 34, pp. 73–84, 2022, doi: https://doi.org/10.1016/j.jot.2022.04.004.

[96] Y. Yang *et al.*, “Additive manufacturing of bone scaffolds,” *Int. J. Bioprinting*, vol. 5, Dec. 2018, doi: 10.18063/ijb.v5i1.148.

[97] J. W. Stansbury and M. J. Idacavage, “3D printing with polymers: Challenges among expanding options and opportunities,” *Dent. Mater.*, vol. 32, no. 1, pp. 54–64, 2016, doi: https://doi.org/10.1016/j.dental.2015.09.018.

[98] S. Bose, S. Vahabzadeh, and A. Bandyopadhyay, “Bone tissue engineering using 3D printing,” *Mater. Today*, vol. 16, no. 12, pp. 496–504, 2013, doi: https://doi.org/10.1016/j.mattod.2013.11.017.

[99] W. Yu *et al.*, “3D-printed Porous Ceramic Scaffolds for Bone Tissue Engineering: A Review,” *Biomater. Sci.*, vol. 5, Jun. 2017, doi: 10.1039/C7BM00315C.

[100] A. L. Maximenko and E. A. Olevsky, “Pore filling during selective laser melting - assisted additive manufacturing of composites,” *Scr. Mater.*, vol. 149, pp. 75–78, 2018, doi: https://doi.org/10.1016/j.scriptamat.2018.02.015.

[101] H. Yves-Christian, W. Jan, M. Wilhelm, W. Konrad, and P. Reinhart, “Net shaped high performance oxide ceramic parts by selective laser melting,” *Phys. Procedia*, vol. 5, pp. 587–594, 2010, doi: https://doi.org/10.1016/j.phpro.2010.08.086.

[102] J. Zhang *et al.*, “Three-dimensional printing of strontium-containing mesoporous bioactive glass scaffolds for bone regeneration,” *Acta Biomater.*, vol. 10, no. 5, pp. 2269–2281, 2014, doi: https://doi.org/10.1016/j.actbio.2014.01.001.

[103] Z. Min, Z. Shichang, X. Chen, Z. Yufang, and Z. Changqing, “3D-printed dimethyloxallyl glycine delivery scaffolds to improve angiogenesis and osteogenesis,” *Biomater. Sci.*, vol. 3, no. 8, pp. 1236–1244, 2015, doi: 10.1039/C5BM00132C.

[104] G. Lee, M. Carrillo, J. McKittrick, D. G. Martin, and E. A. Olevsky, “Fabrication of ceramic bone scaffolds by solvent jetting 3D printing and sintering: Towards load-bearing applications,” *Addit. Manuf.*, vol. 33, 2020, doi: 10.1016/j.addma.2020.101107.

[105] H. Seitz, U. Deisinger, B. Leukers, R. Detsch, and G. Ziegler, “Different Calcium Phosphate Granules for 3-D Printing of Bone Tissue Engineering Scaffolds,” *Adv. Eng. Mater.*, vol. 11, no. 5, pp. B41–B46, May 2009, doi: https://doi.org/10.1002/adem.200800334.

[106] A. Butscher *et al.*, “Printability of calcium phosphate powders for three-dimensional printing of tissue engineering scaffolds,” *Acta Biomater.*, vol. 8, no. 1, pp. 373–385, 2012, doi: https://doi.org/10.1016/j.actbio.2011.08.027.

[107] E. Vorndran *et al.*, “3D Powder Printing of β-Tricalcium Phosphate Ceramics Using Different Strategies,” *Adv. Eng. Mater.*, vol. 10, pp. B67–B71, Jan. 2009, doi: 10.1002/adem.200800179.

[108] B. Duan and M. Wang, “Customized Ca–P/PHBV nanocomposite scaffolds for bone tissue engineering: design, fabrication, surface modification and sustained release of growth factor,” *J. R. Soc. Interface*, vol. 7, no. suppl_5, 2010, doi: 10.1098/rsif.2010.0127.focus.

[109] Y. Du *et al.*, “Selective laser sintering scaffold with hierarchical architecture and gradient composition for osteochondral repair in rabbits,” *Biomaterials*, vol. 137, pp. 37–48, 2017, doi: https://doi.org/10.1016/j.biomaterials.2017.05.021.

[110] B. Duan, M. Wang, W. Y. Zhou, W. L. Cheung, Z. Y. Li, and W. W. Lu, “Three-dimensional nanocomposite scaffolds fabricated via selective laser sintering for bone tissue engineering,” *Acta Biomater.*, vol. 6, no. 12, pp. 4495–4505, 2010, doi: https://doi.org/10.1016/j.actbio.2010.06.024.

[111] Y. Zhang *et al.*, “Mesoporous bioactive glass nanolayer-functionalized 3D-printed scaffolds for accelerating osteogenesis and angiogenesis,” *Nanoscale*, vol. 7, no. 45, pp. 19207–19221, 2015, doi: 10.1039/C5NR05421D.

[112] J.-P. Carrel, A. Wiskott, M. Moussa, P. Rieder, S. Scherrer, and S. Durual, “A 3D printed TCP/HA structure as a new osteoconductive scaffold for vertical bone augmentation,” *Clin. Oral Implants Res.*, vol. 27, no. 1, pp. 55–62, Jan. 2016, doi: https://doi.org/10.1111/clr.12503.

[113] A. Lode *et al.*, “Fabrication of porous scaffolds by three-dimensional plotting of a pasty calcium phosphate bone cement under mild conditions,” *J. Tissue Eng. Regen. Med.*, vol. 8, no. 9, pp. 682–693, Sep. 2014, doi: https://doi.org/10.1002/term.1563.

[114] J. Zhao, X. Lu, K. Duan, L. Y. Guo, S. B. Zhou, and J. Weng, “Improving mechanical and biological properties of macroporous HA scaffolds through composite coatings,” *Colloids Surfaces B Biointerfaces*, vol. 74, no. 1, pp. 159–166, 2009, doi: https://doi.org/10.1016/j.colsurfb.2009.07.012.

[115] J. M. Oliveira *et al.*, “Macroporous hydroxyapatite scaffolds for bone tissue engineering applications: Physicochemical characterization and assessment of rat bone marrow stromal cell viability,” *J. Biomed. Mater. Res. Part A*, vol. 91A, no. 1, pp. 175–186, Oct. 2009, doi: https://doi.org/10.1002/jbm.a.32213.

[116] P. Miranda, A. Pajares, E. Saiz, A. P. Tomsia, and F. Guiberteau, “Mechanical properties of calcium phosphate scaffolds fabricated by robocasting,” *J. Biomed. Mater. Res. A*, vol. 85, no. 1, pp. 218–227, 2008, doi: 10.1002/jbm.a.31587.

[117] M. Mirkhalaf, Y. Men, R. Wang, Y. No, and H. Zreiqat, “Personalized 3D printed bone scaffolds: A review,” *Acta Biomater.*, vol. 156, pp. 110–124, 2023, doi: https://doi.org/10.1016/j.actbio.2022.04.014.

[118] R. M. German, *Sintering Theory and Practice*. New York: John Wiley & Sons, Ltd, 1996.

[119] A. O. Araoyinbo, F. A. Ishola, E. Y. Salawu, M. B. Biodun, and A. U. Samuel, “Overview of powder metallurgy process and its advantages,” *AIP Conf. Proc.*, vol. 2437, no. 1, p. 20153, Aug. 2022, doi: 10.1063/5.0092502.

[120] K. I. Rybakov, E. A. Olevsky, and E. V Krikun, “Microwave Sintering: Fundamentals and Modeling,” *J. Am. Ceram. Soc.*, vol. 96, no. 4, pp. 1003–1020, Apr. 2013, doi: https://doi.org/10.1111/jace.12278.

[121] Z. Xu, “Study on microwave sintering process and surface texture characteristics of ceramic materials,” in *IOP Conference Series: Materials Science and Engineering*, 2019, vol. 677, no. 2, p. 22078.

[122] M. Tokita, “Progress of Spark Plasma Sintering (SPS) Method, Systems, Ceramics Applications and Industrialization,” *Ceramics*, vol. 4, no. 2. pp. 160–198, 2021, doi: 10.3390/ceramics4020014.

[123] E. A. Olevsky, “Theory of sintering: from discrete to continuum,” *Mater. Sci. Eng. R Reports*, vol. 23, no. 2, pp. 41–100, 1998, doi: https://doi.org/10.1016/S0927-796X(98)00009-6.

[124] C. Herring, “Effect of Change of Scale on Sintering Phenomena,” *J. Appl. Phys.*, vol. 21, no. 4, pp. 301–303, Apr. 1950, doi: 10.1063/1.1699658.

[125] T. Kokubo, *Bioceramics and their clinical applications*. Elsevier, 2008.

[126] R. M. German, “History of sintering: empirical phase,” *Powder Metall.*, vol. 56, no. 2, pp. 117–123, Apr. 2013, doi: 10.1179/1743290112Y.0000000025.

[127] J. H. Shepherd, R. J. Friederichs, and S. M. Best, “11 - Synthetic hydroxyapatite for tissue engineering applications,” in *Woodhead Publishing Series in Biomaterials*, M. B. T.-H. (Hap) for B. A. Mucalo, Ed. Woodhead Publishing, 2015, pp. 235–267.

[128] P. Greil, T. Fey, and C. Zollfrank, “Chapter 7.1 - Biomorphous Ceramics from Lignocellulosic Preforms,” S. B. T.-H. of A. C. (Second E. Somiya, Ed. Oxford: Academic Press, 2013, pp. 527–555.

[129] S. Gopi, A. Pius, and S. Thomas, “11 - Synthesis, microstructure, and properties of high-strength porous ceramics,” in *Woodhead Publishing Series in Biomaterials*, S. Thomas, P. Balakrishnan, and M. S. B. T.-F. B. C. Sreekala, Eds. Woodhead Publishing, 2018, pp. 265–271.

[130] E. Champion, “Sintering of calcium phosphate bioceramics,” *Acta Biomater.*, vol. 9, no. 4, pp. 5855–5875, 2013, doi: https://doi.org/10.1016/j.actbio.2012.11.029.

[131] E. A. Monroe, W. Votava, D. B. Bass, and J. M. Mullen, “New Calcium Phosphate Ceramic Material for Bone and Tooth Implants,” *J. Dent. Res.*, vol. 50, no. 4, pp. 860–861, Jul. 1971, doi: 10.1177/00220345710500041201.

[132] H.-J. Kleebe, E. F. Brs, D. Bernache-Assolant, and G. Ziegler, “High-Resolution Electron Microscopy and Convergent-Beam Electron Diffraction of Sintered Undoped Hydroxyapatite,” *J. Am. Ceram. Soc.*, vol. 80, no. 1, pp. 37–44, Jan. 1997, doi: https://doi.org/10.1111/j.1151-2916.1997.tb02788.x.

[133] X. Guo, P. Xiao, J. Liu, and Z. Shen, “Fabrication of Nanostructured Hydroxyapatite via Hydrothermal Synthesis and Spark Plasma Sintering,” *J. Am. Ceram. Soc.*, vol. 88, no. 4, pp. 1026–1029, Apr. 2005, doi: https://doi.org/10.1111/j.1551-2916.2005.00198.x.

[134] A. J. Wagoner Johnson and B. A. Herschler, “A review of the mechanical behavior of CaP and CaP/polymer composites for applications in bone replacement and repair,” *Acta Biomater.*, vol. 7, no. 1, pp. 16–30, 2011, doi: https://doi.org/10.1016/j.actbio.2010.07.012.

[135] A. Nakahira, M. Tamai, H. Aritani, S. Nakamura, and K. Yamashita, “Biocompatibility of dense hydroxyapatite prepared using an SPS process,” *J. Biomed. Mater. Res.*, vol. 62, no. 4, pp. 550–557, Dec. 2002, doi: https://doi.org/10.1002/jbm.10344.

[136] G.-J. Oh, K.-D. Yun, K.-M. Lee, H.-P. Lim, and S.-W. Park, “Sintering behavior and mechanical properties of zirconia compacts fabricated by uniaxial press forming,” *J. Adv. Prosthodont.*, vol. 2, no. 3, pp. 81–87, 2010, doi: 10.4047/jap.2010.2.3.81.

[137] M. Seidenstuecker *et al.*, “3D Powder Printed Bioglass and β-Tricalcium Phosphate Bone Scaffolds,” *Materials* , vol. 11, no. 1. 2018, doi: 10.3390/ma11010013.

[138] X. Song *et al.*, “Biomimetic 3D Printing of Hierarchical and Interconnected Porous Hydroxyapatite Structures with High Mechanical Strength for Bone Cell Culture,” *Adv.*

Eng. Mater., vol. 21, no. 1, p. 1800678, Jan. 2019, doi: https://doi.org/10.1002/adem.201800678.

[139] S. Landgraeber, M. Jäger, J. J. Jacobs, and N. J. Hallab, "The Pathology of Orthopedic Implant Failure Is Mediated by Innate Immune System Cytokines," *Mediators Inflamm.*, vol. 2014, p. 185150, 2014, doi: 10.1155/2014/185150.

[140] N. J. Hallab, "A review of the biologic effects of spine implant debris: Fact from fiction," *SAS J.*, vol. 3, no. 4, pp. 143–160, 2009, doi: https://doi.org/10.1016/j.esas.2009.11.005.

[141] Y. Li, C. Wong, J. Xiong, P. Hodgson, and C. Wen, "Cytotoxicity of Titanium and Titanium Alloying Elements," *J. Dent. Res.*, vol. 89, no. 5, pp. 493–497, Mar. 2010, doi: 10.1177/0022034510363675.

[142] M. Ziaee and N. B. Crane, "Binder jetting: A review of process, materials, and methods," *Addit. Manuf.*, vol. 28, pp. 781–801, 2019, doi: https://doi.org/10.1016/j.addma.2019.05.031.

[143] L. C. Hwa, S. Rajoo, A. M. Noor, N. Ahmad, and M. B. Uday, "Recent advances in 3D printing of porous ceramics: A review," *Curr. Opin. Solid State Mater. Sci.*, vol. 21, no. 6, pp. 323–347, 2017, doi: https://doi.org/10.1016/j.cossms.2017.08.002.

[144] A. Cabo Rios, E. Hryha, E. Olevsky, and P. Harlin, "Sintering anisotropy of binder jetted 316L stainless steel: part I – sintering anisotropy," *Powder Metall.*, vol. 65, no. 4, pp. 273–282, Aug. 2022, doi: 10.1080/00325899.2021.2020485.

[145] A. Cabo Rios, E. Hryha, E. Olevsky, and P. Harlin, "Sintering anisotropy of binder jetted 316L stainless steel: part II – microstructure evolution during sintering," *Powder Metall.*, pp. 1–13, Jan. 2022, doi: 10.1080/00325899.2021.2020486.

[146] C. Zheng, A. Mostafaei, P. R. de Vecchis, I. Nettleship, and M. Chmielus, "Microstructure evolution for isothermal sintering of binder jet 3D printed alloy 625 above and below the solidus temperature," *Addit. Manuf.*, vol. 47, p. 102276, 2021, doi: https://doi.org/10.1016/j.addma.2021.102276.

[147] M. Salehi, M. Gupta, S. Maleksaeedi, and N. M. L. Sharon, "Inkjet based 3D additive manufacturing of metals," 2018.

[148] S. C. Cox, J. A. Thornby, G. J. Gibbons, M. A. Williams, and K. K. Mallick, "3D printing of porous hydroxyapatite scaffolds intended for use in bone tissue engineering applications," *Mater. Sci. Eng. C*, vol. 47, pp. 237–247, 2015.

[149] Y. Shanjani, J. N. A. De Croos, R. M. Pilliar, R. A. Kandel, and E. Toyserkani, "Solid freeform fabrication and characterization of porous calcium polyphosphate structures for tissue engineering purposes," *J. Biomed. Mater. Res. Part B Appl. Biomater.*, vol. 93B, no. 2, pp. 510–519, May 2010, doi: https://doi.org/10.1002/jbm.b.31610.

[150] R. Chumnanklang, T. Panyathanmaporn, K. Sitthiseripratip, and J. Suwanprateeb, “3D printing of hydroxyapatite: Effect of binder concentration in pre-coated particle on part strength,” *Mater. Sci. Eng. C*, vol. 27, no. 4, pp. 914–921, 2007, doi: https://doi.org/10.1016/j.msec.2006.11.004.

[151] H. Kakisawa, K. Minagawa, K. Ida, K. Maekawa, and K. Halada, “Dense P/M Component Produced by Solid Freeform Fabrication (SFF),” *Mater. Trans. - MATER TRANS*, vol. 46, pp. 2574–2581, Dec. 2005, doi: 10.2320/matertrans.46.2574.

[152] H. Miyanaji, K. M. Rahman, M. Da, and C. B. Williams, “Effect of fine powder particles on quality of binder jetting parts,” *Addit. Manuf.*, vol. 36, p. 101587, 2020, doi: https://doi.org/10.1016/j.addma.2020.101587.

[153] D. Veljović *et al.*, “The effect of the shape and size of the pores on the mechanical properties of porous HAP-based bioceramics,” *Ceram. Int.*, vol. 37, no. 2, pp. 471–479, 2011, doi: https://doi.org/10.1016/j.ceramint.2010.09.014.

[154] H. Miyanaji, N. Momenzadeh, and L. Yang, “Effect of printing speed on quality of printed parts in Binder Jetting Process,” *Addit. Manuf.*, vol. 20, pp. 1–10, 2018.

[155] A. Mostafaei *et al.*, “Binder jet 3D printing—Process parameters, materials, properties, modeling, and challenges,” *Prog. Mater. Sci.*, vol. 119, p. 100707, 2021.

[156] S. Shrestha and G. Manogharan, “Optimization of binder jetting using Taguchi method,” *Jom*, vol. 69, pp. 491–497, 2017.

[157] Y. Bai and C. B. Williams, “An exploration of binder jetting of copper,” *Rapid Prototyp. J.*, 2015.

[158] T. Colton, C. Inkley, A. Berry, and N. B. Crane, “Impact of inkjet printing parameters and environmental conditions on formation of 2D and 3D binder jetting geometries,” *J. Manuf. Process.*, vol. 71, pp. 187–196, 2021.

[159] X. Lv, F. Ye, L. Cheng, S. Fan, and Y. Liu, “Binder jetting of ceramics: Powders, binders, printing parameters, equipment, and post-treatment,” *Ceram. Int.*, vol. 45, no. 10, pp. 12609–12624, 2019.

[160] B. R. Utela, D. Storti, R. L. Anderson, and M. Ganter, “Development process for custom three-dimensional printing (3DP) material systems,” *J. Manuf. Sci. Eng.*, vol. 132, no. 1, 2010.

[161] E. M. Sachs *et al.*, “Jetting layers of powder and the formation of fine powder beds thereby.” Google Patents, Jul. 22, 2003.

[162] A. Butscher, M. Bohner, N. Doebelin, L. Galea, O. Loeffel, and R. Müller, “Moisture based three-dimensional printing of calcium phosphate structures for scaffold engineering,” *Acta Biomater.*, vol. 9, no. 2, pp. 5369–5378, 2013, doi: https://doi.org/10.1016/j.actbio.2012.10.009.

[163] K. Lu and W. T. Reynolds, “3DP process for fine mesh structure printing,” *Powder Technol.*, vol. 187, no. 1, pp. 11–18, 2008.

[164] P. Nandwana, A. M. Elliott, D. Siddel, A. Merriman, W. H. Peter, and S. S. Babu, “Powder bed binder jet 3D printing of Inconel 718: Densification, microstructural evolution and challenges☆,” *Curr. Opin. Solid State Mater. Sci.*, vol. 21, no. 4, pp. 207–218, 2017.

[165] Z. Zhou, C. A. Mitchell, F. J. Buchanan, and N. J. Dunne, “Effects of heat treatment on the mechanical and degradation properties of 3D-printed calcium-sulphate-based scaffolds,” *Int. Sch. Res. Not.*, vol. 2013, 2013.

[166] J. F. Bredt, S. Clark, and G. Gilchrist, “Three dimensional printing material system and method.” Google Patents, Aug. 08, 2006.

[167] A. C. Hoffmann and H. J. Finkers, “A relation for the void fraction of randomly packed particle beds,” *Powder Technol.*, vol. 82, no. 2, pp. 197–203, 1995.

[168] M. Zago, N. F. M. Lecis, M. Vedani, and I. Cristofolini, “Dimensional and geometrical precision of parts produced by binder jetting process as affected by the anisotropic shrinkage on sintering,” *Addit. Manuf.*, vol. 43, p. 102007, 2021, doi: https://doi.org/10.1016/j.addma.2021.102007.

[169] S. Sadeghi Borujeni, A. Shad, K. Abburi Venkata, N. Günther, and V. Ploshikhin, “Numerical simulation of shrinkage and deformation during sintering in metal binder jetting with experimental validation,” *Mater. Des.*, vol. 216, p. 110490, 2022, doi: https://doi.org/10.1016/j.matdes.2022.110490.

[170] J. oh, S. Nahm, B. Kim, and H. Choi, “Anisotropy in Green Body Bending Strength due to Additive Direction in the Binder-Jetting Additive Manufacturing Process,” *Korean J. Met. Mater.*, vol. 57, pp. 227–235, Apr. 2019, doi: 10.3365/KJMM.2019.57.4.227.

[171] R. Hamano, Y. Nakagawa, V. Irawan, and T. Ikoma, “Mechanical anisotropy and fracture mode of binder jetting 3D printed calcium sulfate moldings,” *Appl. Mater. Today*, vol. 25, p. 101160, 2021, doi: https://doi.org/10.1016/j.apmt.2021.101160.

[172] Y. Lee, P. Nandwana, and S. Simunovic, “Powder spreading, densification, and part deformation in binder jetting additive manufacturing,” *Prog. Addit. Manuf.*, vol. 7, no. 1, pp. 111–125, 2022, doi: 10.1007/s40964-021-00214-1.

[173] H. Palmour, M. Geho, R. L. Russell, and T. M. Hare, “Study of DO-Effects on Subsequent Densification Behavior in Spinel and Alumina Ceramics ,” *Solid State Phenom.*, vol. 25–26, pp. 37–44, 1992, doi: 10.4028/www.scientific.net/SSP.25-26.37.

[174] J. E. Barralet, S. M. Best, and W. Bonfield, “Effect of sintering parameters on the density and microstructure of carbonate hydroxyapatite,” *J. Mater. Sci. Mater. Med.*, vol. 11, no. 11, pp. 719–724, 2000, doi: 10.1023/A:1008975812793.

[175] Y. Aman, V. Garnier, and E. Djurado, “Influence of green state processes on the sintering behaviour and the subsequent optical properties of spark plasma sintered alumina,” *J. Eur. Ceram. Soc.*, vol. 29, no. 16, pp. 3363–3370, 2009, doi: https://doi.org/10.1016/j.jeurceramsoc.2009.07.014.

[176] D. Ravi and D. J. Green, “Sintering stresses and distortion produced by density differences in bi-layer structures,” *J. Eur. Ceram. Soc.*, vol. 26, no. 1, pp. 17–25, 2006, doi: https://doi.org/10.1016/j.jeurceramsoc.2004.10.032.

[177] H. Riedel and T. Kraft, “Distortions and Cracking of Graded Components during Sintering,” *Mater. Sci. Forum*, vol. 308–311, pp. 1035–1040, 1999, doi: 10.4028/www.scientific.net/MSF.308-311.1035.

[178] Z.-Z. Du and A. C. F. Cocks, “Constitutive models for the sintering of ceramic components—I. Material models,” *Acta Metall. Mater.*, vol. 40, no. 8, pp. 1969–1979, 1992, doi: https://doi.org/10.1016/0956-7151(92)90183-F.

[179] D. J. Green, O. Guillon, and J. Rödel, “Constrained sintering: A delicate balance of scales,” *J. Eur. Ceram. Soc.*, vol. 28, no. 7, pp. 1451–1466, 2008, doi: https://doi.org/10.1016/j.jeurceramsoc.2007.12.012.

[180] H. Kim, O. Gillia, and D. Bouvard, “A phenomenological constitutive model for the sintering of alumina powder,” *J. Eur. Ceram. Soc.*, vol. 23, no. 10, pp. 1675–1685, 2003, doi: https://doi.org/10.1016/S0955-2219(02)00411-9.

[181] E. A. Olevsky, V. Tikare, and T. Garino, “Multi-Scale Study of Sintering: A Review,” *J. Am. Ceram. Soc.*, vol. 89, no. 6, pp. 1914–1922, Jun. 2006, doi: https://doi.org/10.1111/j.1551-2916.2006.01054.x.

[182] R. Raj, “Analysis of the Sintering Pressure,” *J. Am. Ceram. Soc.*, vol. 70, no. 9, p. C-210-C-211, Sep. 1987, doi: https://doi.org/10.1111/j.1151-2916.1987.tb05743.x.

[183] R. K. Bordia and G. W. Scherer, “On constrained sintering—I. Constitutive model for a sintering body,” *Acta Metall.*, vol. 36, no. 9, pp. 2393–2397, 1988, doi: https://doi.org/10.1016/0001-6160(88)90189-7.

[184] R. K. Bordia and G. W. Scherer, “On constrained sintering—II. Comparison of constitutive models,” *Acta Metall.*, vol. 36, no. 9, pp. 2399–2409, 1988, doi: https://doi.org/10.1016/0001-6160(88)90190-3.

[185] R. K. Bordia and G. W. Scherer, “On constrained sintering—III. Rigid inclusions,” *Acta Metall.*, vol. 36, no. 9, pp. 2411–2416, 1988, doi: https://doi.org/10.1016/0001-6160(88)90191-5.

[186] H. E. Exner, *Principles of Single Phase Sintering*. Freund Publishing House, 1979.

[187] R. M. German and Z. A. Munir, “The geometry of sintering wires,” *J. Mater. Sci.*, vol. 10, no. 10, pp. 1719–1724, 1975, doi: 10.1007/BF00554933.

[188] D. Uskoković and H. E. Exner, "The Kinetics of Contact Formation During Sintering by Diffusion Mechanisms BT - Sintering Key Papers," S. Sōmiya and Y. Moriyoshi, Eds. Dordrecht: Springer Netherlands, 1990, pp. 111–146.

[189] W. F. Smith and J. Hashemi, *Foundations of Materials Science and Engineering*. McGraw-Hill, 2003.

[190] C. Manière, G. Lee, J. McKittrick, S. Chan, and E. A. Olevsky, "Modeling zirconia sintering trajectory for obtaining translucent submicronic ceramics for dental implant applications," *Acta Mater.*, vol. 188, pp. 101–107, 2020, doi: https://doi.org/10.1016/j.actamat.2020.01.061.

[191] R. Singh, S. Singh, and G. Singh, "Dimensional Accuracy Comparison of Investment Castings Prepared with Wax and ABS Patterns for Bio-medical Application," *Procedia Mater. Sci.*, vol. 6, pp. 851–858, 2014, doi: https://doi.org/10.1016/j.mspro.2014.07.102.

[192] J. Mun, B.-G. Yun, J. Ju, and B.-M. Chang, "Indirect additive manufacturing based casting of a periodic 3D cellular metal – Flow simulation of molten aluminum alloy," *J. Manuf. Process.*, vol. 17, pp. 28–40, 2015, doi: https://doi.org/10.1016/j.jmapro.2014.11.001.

[193] J. Mun and J. Thurman, "Indirect Additive Manufacturing Based Casting (I·AM Casting) of a Lattice Structure," *ASME Int. Mech. Eng. Congr. Expo. Proc.*, vol. 2, Nov. 2014, doi: 10.1115/IMECE2014-38055.

[194] P. Torabi, M. Petros, and B. Khoshnevis, "Selective Inhibition Sintering: The Process for Consumer Metal Additive Manufacturing," *3D Print. Addit. Manuf.*, vol. 1, no. 3, pp. 152–155, Sep. 2014, doi: 10.1089/3dp.2014.0017.

[195] B. Khoshnevis, J. Zhang, M. Fateri, and Z. Xiao, *CERAMICS 3D PRINTING BY SELECTIVE INHIBITION SINTERING*. 2014.

[196] M. Carrabba *et al.*, "Translucent zirconia in the ceramic scenario for monolithic restorations: A flexural strength and translucency comparison test," *J. Dent.*, vol. 60, pp. 70–76, 2017, doi: https://doi.org/10.1016/j.jdent.2017.03.002.

[197] E. A. Olevsky and D. V. Dudina, *Field-assisted sintering: Science and applications*. 2018.

[198] R. Orrù, R. Licheri, A. M. Locci, A. Cincotti, and G. Cao, "Consolidation/synthesis of materials by electric current activated/assisted sintering," *Mater. Sci. Eng. R Reports*, vol. 63, no. 4, pp. 127–287, 2009, doi: https://doi.org/10.1016/j.mser.2008.09.003.

[199] Z. A. Munir, U. Anselmi-Tamburini, and M. Ohyanagi, "The effect of electric field and pressure on the synthesis and consolidation of materials: A review of the spark plasma sintering method," *J. Mater. Sci.*, vol. 41, no. 3, pp. 763–777, 2006, doi: 10.1007/s10853-006-6555-2.

[200] T. Nishimura, M. Mitomo, H. Hirotsuru, and M. Kawahara, “Fabrication of silicon nitride nano-ceramics by spark plasma sintering,” *J. Mater. Sci. Lett.*, vol. 14, no. 15, pp. 1046–1047, 1995, doi: 10.1007/BF00258160.

[201] S. Grasso, Y. Sakka, and G. Maizza, “Electric Current Activated/Assisted Sintering (ECAS): a Review of Patents 1906–2008,” *Sci. Technol. Adv. Mater. - SCI TECHNOL ADV MATER*, vol. 10, Oct. 2009, doi: 10.1088/1468-6996/10/5/053001.

[202] O. Guillon *et al.*, “Field-Assisted Sintering Technology/Spark Plasma Sintering: Mechanisms, Materials, and Technology Developments,” *Adv. Eng. Mater.*, vol. 16, Jul. 2014, doi: 10.1002/adem.201300409.

[203] B.-N. Kim, K. Hiraga, K. Morita, and H. Yoshida, “Effects of heating rate on microstructure and transparency of spark-plasma-sintered alumina,” *J. Eur. Ceram. Soc.*, vol. 29, no. 2, pp. 323–327, 2009, doi: https://doi.org/10.1016/j.jeurceramsoc.2008.03.015.

[204] T. Voisin, J. Monchoux, L. Durand, N. Karnatak, M. Thomas, and A. Couret, “An Innovative Way to Produce γ-TiAl Blades: Spark Plasma Sintering,” *Adv. Eng. Mater.*, vol. 17, Apr. 2015, doi: 10.1002/adem.201500019.

[205] C. Manière, L. Durand, A. Weibel, G. Chevallier, and C. Estournès, “A sacrificial material approach for spark plasma sintering of complex shapes,” *Scr. Mater.*, vol. 124, pp. 126–128, 2016, doi: https://doi.org/10.1016/j.scriptamat.2016.07.006.

[206] P. Mondalek, L. Silva, and M. Bellet, “A Numerical Model for Powder Densification by SPS Technique,” *Adv. Eng. Mater.*, vol. 13, pp. 587–593, Jul. 2011, doi: 10.1002/adem.201000340.

[207] C. Manière, L. Durand, A. Weibel, and C. Estournès, “Spark-plasma-sintering and finite element method: From the identification of the sintering parameters of a submicronic α-alumina powder to the development of complex shapes,” *Acta Mater.*, vol. 102, pp. 169–175, 2016, doi: 10.1016/j.actamat.2015.09.003.

[208] H. Kim, O. Gillia, P. Dorémus, and D. Bouvard, “Near net shape processing of a sintered alumina component: adjustment of pressing parameters through finite element simulation,” *Int. J. Mech. Sci.*, vol. 44, no. 12, pp. 2523–2539, 2002, doi: https://doi.org/10.1016/S0020-7403(02)00189-3.

[209] C. Manière, E. Nigito, L. Durand, A. Weibel, Y. Beynet, and C. Estournès, “Spark plasma sintering and complex shapes: The deformed interfaces approach,” *Powder Technol.*, vol. 320, pp. 340–345, 2017, doi: https://doi.org/10.1016/j.powtec.2017.07.048.

[210] C. Manière, E. Torresani, and E. A. Olevsky, “Simultaneous Spark Plasma Sintering of Multiple Complex Shapes,” *Materials* , vol. 12, no. 4. 2019, doi: 10.3390/ma12040557.

[211] H. Yoshikawa, N. Tamai, T. Murase, and A. Myoui, “Interconnected Porous Hydroxyapatite Ceramics for Bone Tissue Engineering,” *J. R. Soc. Interface*, vol. 6 Suppl 3, pp. S341-8, Jun. 2009, doi: 10.1098/rsif.2008.0425.focus.

[212] C. Feng *et al.*, “Three-Dimensional Printing of Scaffolds with Synergistic Effects of Micro–Nano Surfaces and Hollow Channels for Bone Regeneration,” *ACS Biomater. Sci. Eng.*, vol. 7, no. 3, pp. 872–880, Mar. 2021, doi: 10.1021/acsbiomaterials.9b01824.

[213] M. H. Carrillo, G. Lee, C. Maniere, and E. A. Olevsky, “Additive manufacturing of powder components based on subtractive sintering approach,” *Rapid Prototyp. J.*, vol. ahead-of-p, no. ahead-of-print, Jan. 2021, doi: 10.1108/RPJ-01-2021-0006.

[214] Y. Yao, W. Qin, B. Xing, N. Sha, T. Jiao, and Z. Zhao, “High performance hydroxyapatite ceramics and a triply periodic minimum surface structure fabricated by digital light processing 3D printing,” *J. Adv. Ceram.*, vol. 10, no. 1, pp. 39–48, 2021, doi: 10.1007/s40145-020-0415-4.

[215] W. Sixel, M. Liu, G. Nellis, and B. Sarlioglu, “Ceramic 3D Printed Direct Winding Heat Exchangers for Improving Electric Machine Thermal Management,” in *2019 IEEE Energy Conversion Congress and Exposition (ECCE)*, 2019, pp. 769–776, doi: 10.1109/ECCE.2019.8913234.

[216] D. Singh *et al.*, “One piece ceramic heat exchanger for concentrating solar power electric plants,” *Renew. Energy*, vol. 160, pp. 1308–1315, 2020, doi: https://doi.org/10.1016/j.renene.2020.07.070.

[217] T. Do, C. Shin, P. Kwon, and J. Yeom, “Fully-Enclosed Ceramic Micro-burners Using Fugitive Phase and Powder-based Processing,” *Sci. Rep.*, vol. 6, no. 1, p. 31336, 2016, doi: 10.1038/srep31336.

[218] M. Bachman and G. P. Li, “Integrated MEMS in package,” *Circuit World*, vol. 38, no. 4, pp. 184–192, Jan. 2012, doi: 10.1108/03056121211280404.

[219] W. Nawrot and K. Malecha, “Additive manufacturing revolution in ceramic microsystems,” *Microelectron. Int.*, vol. 37, no. 2, pp. 79–85, Jan. 2020, doi: 10.1108/MI-11-2019-0073.

[220] R. K. Bordia, S.-J. L. Kang, and E. A. Olevsky, “Current understanding and future research directions at the onset of the next century of sintering science and technology,” *J. Am. Ceram. Soc.*, vol. 100, no. 6, pp. 2314–2352, Jun. 2017, doi: https://doi.org/10.1111/jace.14919.

[221] A. G. K. Jinka and R. W. Lewis, “Finite element simulation of hot isostatic pressing of metal powders,” *Comput. Methods Appl. Mech. Eng.*, vol. 114, no. 3, pp. 191–212, 1994, doi: https://doi.org/10.1016/0045-7825(94)90174-0.

[222] M. Abouaf, J. L. Chenot, G. Raisson, and P. Bauduin, “Finite element simulation of hot

isostatic pressing of metal powders," *Int. J. Numer. Methods Eng.*, vol. 25, no. 1, pp. 191–212, Jan. 1988, doi: https://doi.org/10.1002/nme.1620250116.

[223] E. A. Olevsky, C. Garcia-Cardona, W. L. Bradbury, C. D. Haines, D. G. Martin, and D. Kapoor, "Fundamental Aspects of Spark Plasma Sintering: II. Finite Element Analysis of Scalability," *J. Am. Ceram. Soc.*, vol. 95, no. 8, pp. 2414–2422, Aug. 2012, doi: https://doi.org/10.1111/j.1551-2916.2012.05096.x.

[224] D. Giuntini *et al.*, "Localized Overheating Phenomena and Optimization of Spark-Plasma Sintering Tooling Design," *Materials (Basel).*, vol. 6, pp. 2612–2632, Jul. 2013, doi: 10.3390/ma6072612.

[225] D. Giuntini, J. RAETHEL, M. Herrmann, A. MICHAELIS, C. Haines, and E. OLEVSKY, "Spark plasma sintering novel tooling design: Temperature uniformization during consolidation of silicon nitride powder," *J. Ceram. Soc. Japan*, vol. 124, pp. 403–414, Apr. 2016, doi: 10.2109/jcersj2.15213.

[226] C. Arnaud *et al.*, "Dog-bone copper specimens prepared by one-step spark plasma sintering," *J. Mater. Sci.*, vol. 50, no. 22, pp. 7364–7373, 2015, doi: 10.1007/s10853-015-9293-5.

[227] X. Wang, S. R. Casolco, G. Xu, and J. E. Garay, "Finite element modeling of electric current-activated sintering: The effect of coupled electrical potential, temperature and stress," *Acta Mater.*, vol. 55, no. 10, pp. 3611–3622, 2007, doi: https://doi.org/10.1016/j.actamat.2007.02.022.

[228] C. Wang, L. Cheng, and Z. Zhao, "FEM analysis of the temperature and stress distribution in spark plasma sintering: Modelling and experimental validation," *Comput. Mater. Sci.*, vol. 49, no. 2, pp. 351–362, 2010, doi: https://doi.org/10.1016/j.commatsci.2010.05.021.

[229] S. Grasso, Y. Sakka, and G. Maizza, "Pressure Effects on Temperature Distribution During Spark Plasma Sintering with Graphite Sample," *Mater. Trans. - MATER TRANS*, vol. 50, pp. 2111–2114, Aug. 2009, doi: 10.2320/matertrans.M2009148.

[230] S. Muñoz and U. Anselmi-Tamburini, "Temperature and stress fields evolution during spark plasma sintering processes," *J. Mater. Sci.*, vol. 45, no. 23, pp. 6528–6539, 2010, doi: 10.1007/s10853-010-4742-7.

[231] X. Wei, D. Giuntini, A. L. Maximenko, C. D. Haines, and E. A. Olevsky, "Experimental Investigation of Electric Contact Resistance in Spark Plasma Sintering Tooling Setup," *J. Am. Ceram. Soc.*, vol. 98, no. 11, pp. 3553–3560, Nov. 2015, doi: https://doi.org/10.1111/jace.13621.

[232] K. Matsugi, H. Kuramoto, T. Hatayama, and O. Yanagisawa, "Temperature distribution at steady state under constant current discharge in spark sintering process of Ti and Al2O3 powders," *J. Mater. Process. Technol.*, vol. 134, no. 2, pp. 225–232, 2003, doi:

https://doi.org/10.1016/S0924-0136(02)01039-7.

[233] A. Zavaliangos, J. Zhang, M. Krammer, and J. R. Groza, “Temperature evolution during field activated sintering,” *Mater. Sci. Eng. A*, vol. 379, no. 1, pp. 218–228, 2004, doi: https://doi.org/10.1016/j.msea.2004.01.052.

[234] K. Vanmeensel, A. Laptev, J. Hennicke, J. Vleugels, and O. Van der Biest, “Modelling of the temperature distribution during field assisted sintering,” *Acta Mater.*, vol. 53, no. 16, pp. 4379–4388, 2005, doi: https://doi.org/10.1016/j.actamat.2005.05.042.

[235] U. Anselmi-Tamburini, J. E. Garay, and Z. A. Munir, “Fundamental investigations on the spark plasma sintering/synthesis process: III. Current effect on reactivity,” *Mater. Sci. Eng. A*, vol. 407, no. 1, pp. 24–30, 2005, doi: https://doi.org/10.1016/j.msea.2005.06.066.

[236] G. Molénat, L. Durand, J. Galy, and A. Couret, “Temperature Control in Spark Plasma Sintering: An FEM Approach,” *J. Metall.*, vol. 2010, Jan. 2010, doi: 10.1155/2010/145431.

[237] A. Pavia *et al.*, “Electro-thermal measurements and finite element method simulations of a spark plasma sintering device,” *J. Mater. Process. Technol.*, vol. 213, no. 8, pp. 1327–1336, 2013, doi: https://doi.org/10.1016/j.jmatprotec.2013.02.003.

[238] A. J.B and C. Walter, “Numerical Simulation of the Temperature and Stress Field Evolution Applied to the Field Assisted Sintering Technique,” *ISRN Mater. Sci.*, vol. 2012, May 2012, doi: 10.5402/2012/698158.

[239] C. Maniere *et al.*, “Pulse analysis and electric contact measurements in spark plasma sintering,” *Electr. Power Syst. Res.*, vol. 127, pp. 307–313, 2015, doi: https://doi.org/10.1016/j.epsr.2015.06.009.

[240] G. Maizza, S. Grasso, and Y. Sakka, “Moving finite-element mesh model for aiding spark plasma sintering in current control mode of pure ultrafine WC powder,” *J. Mater. Sci.*, vol. 44, no. 5, pp. 1219–1236, 2009, doi: 10.1007/s10853-008-3179-8.

[241] C. Geindreau, D. Bouvard, and P. Doremus, “Constitutive behaviour of metal powder during hot forming. Part I: Experimental investigation with lead powder as a simulation material,” *Eur. J. Mech. - A/Solids*, vol. 18, no. 4, pp. 581–596, 1999, doi: https://doi.org/10.1016/S0997-7538(99)00102-3.

[242] M. Suárez, A. Fernandez, J. L. Menendez, R. Torrecillas, and H. U. Kessel, “Challenges and Opportunities for Spark Plasma Sintering: A Key Technology for a New Generation of Materials,” *Sinter. Appl.*, pp. 320–338, Feb. 2013, doi: 10.5772/53706.

[243] D. Giuntini, J. Raethel, M. Herrmann, A. Michaelis, and E. A. Olevsky, “Advancement of Tooling for Spark Plasma Sintering,” *J. Am. Ceram. Soc.*, vol. 98, no. 11, pp. 3529–3537, Nov. 2015, doi: https://doi.org/10.1111/jace.13528.

[244] W. Li, E. A. Olevsky, J. McKittrick, A. L. Maximenko, and R. M. German, "Densification mechanisms of spark plasma sintering: multi-step pressure dilatometry," *J. Mater. Sci.*, vol. 47, no. 20, pp. 7036–7046, 2012, doi: 10.1007/s10853-012-6515-y.

[245] G. Lee *et al.*, "Densification of zirconium nitride by spark plasma sintering and high voltage electric discharge consolidation: A comparative analysis," *Ceram. Int.*, vol. 41, Aug. 2015, doi: 10.1016/j.ceramint.2015.08.042.